UNIVERSITA' DEGLI STUDI DI PARMA

Dottorato di ricerca in Scienza e Tecnologia dei Materiali Innovativi

Ciclo XXVIII (2013-2015)

Electrical investigation of p-type 4H-SiC heavily doped by ion implantation

Coordinatore:
Chiar.mo Prof. Dalcanale Enrico

Tutor:
Chiar.ma Prof. Parisini Antonella

Dottorando: Gorni Marco

2016

Table of contents

1. Introduction

The energy efficiency is one of the main goal in modern society because of the increasing of power consumption and a contemporary decreasing of natural resources. The worldwide industrialization and globalization have consistently accelerated the power demand, leading to double the energy demand more or less every 40 years. More than 80% of energy is currently provided by fossil fuels and non-renewable resources in general, causing massive release of pollutants in the atmosphere other than a rapid reduction of their availability.

A global effort has been started towards the implementation of energy-efficient electronics. The research activity on microelectronic and power electronic has grown with a nearly exponential rate during the last decades, leading to a progressive reduction of devices and integrated circuits and, over all, a reduction of energy consumption through its efficient use. The increasing dependence on power electronics in modern society has motivated great advances in power electronics technology. These advances are significantly dependent on performance enhancements of power devices that have been widely used in power generation and power distribution. In the last decades, Silicon (Si) technology has dominated the power electronic field, permitting the fabrication of semiconductor devices able to operate in a wide spectrum of power levels and frequencies. Due to the inherent limitations of silicon material properties, such as narrow bandgap, low thermal conductivity and low critical electric field, Silicon power devices are approaching their limits in terms of higher power and higher temperature operations, offering no significant improvement in device performances with further investment. Hence, this

material is no longer suitable for modern power electronics application. The demand for improved energy efficiency in power electronics, which can be satisfied by reducing the switching and conduction losses of devices, as well as for devices capable of high temperature operation, is pushing the power electronics technology development toward wide band gap (WBG) semiconductors. In this context, Silicon Carbide (SiC) and gallium nitride (GaN) exhibit interesting electrical and physical properties that can satisfy the continuous demands of improved energy efficiency (see ref. [1]). SiC, in particular, has been recognized, among all the WBG materials, as a good candidate for replacing silicon in several power device applications. SiC-based electronic devices can work at higher temperature, higher power and in environments harsher than the current traditional semiconductor technology may do. The potential application fields of SiC-based electronic devices nowadays include aerospace (high temperature engines and radiation hard devices), transportation (power supply and power modules), industry, communications and renewable energies (power conversion). The main advantages offered by SiC in comparison with silicon are an higher breakdown field (ten times higher), an higher thermal conductivity (more than three times higher at room temperature), and an higher operating temperature (up to 600°C for SiC devices, where silicon one stops at only 150°C), but also low switching losses in high frequencies applications and lower on-resistances in unipolar devices (see ref. [2]). Among all the large number of polytypes (i.e., of different crystal structures), the more mature and better studied is the hexagonal polytype 4H-SiC, mainly due to its wider band (3.26 eV). These aspects are discussed in chapter 2 of this thesis.

There are, however, several issues concerning the processing technology of this material, as the planar and selective area doping for planar device fabrication: as discussed in chapter 3, ion implantation is the preferable practical method that can be

adopted for these purposes, especially for heavy doping. This doping technique requires a subsequent electrical activation of implanted dopants and a recovery of crystal lattice, damaged by the implantation process: both these requirements can be satisfied by the application of thermal treatments on implanted materials.

The increasing of both the volume density of implanted dopants and the temperature of these post implantation thermal treatments was the approach adopted over the last years to lower the resistivity of silicon carbide, as this reduction is highly desirable mainly for the fabrication of good ohmic contacts, in particular for p-type doping, where all the acceptor species show high ionization energy (see chapter 2). For these reasons, an original approach was explored in this work: 4H-SiC material, heavily doped by the implantation of Aluminum (Al), the preferred acceptor elements as shown in chapter 2, was subjected to thermal treatments performed at very high temperatures, up to 1950-2000°C. The realization of these samples is discussed in chapter 4. To evaluate the effectiveness of this approach, and so to evaluate the doping level, the compensation and the resistivity, as well as to investigate the electrical properties of the samples obtained in this way, an electrical investigation was performed on such samples by Hall effect and resistivity measurements. The results of this investigation are showed and discussed in chapter 5.

Such high implantation doses and thermal treatments temperatures, however, could induce the formation of defects inside the material, and so to the presence of unwanted electrically active deep traps. Their presence can be investigated by Space Charge Spectroscopy techniques like Admittance Spectroscopy and Deep Level Transient Spectroscopy, as showed in chapter 4. For this reason, during this work it was developed an automated acquisition system, mainly for the Admittance Spectroscopy,

and a preliminary electrical investigation on 4H-SiC diodes, obtained by Al+ implantation, was performed and showed in the last part of chapter 5.

This work was made in collaboration with the research group of Dr. Roberta Nipoti of CNR-IMM Institute of Bologna (Italy), responsible of the processing of the samples and transport data above room temperature.

1.1 References of this chapter

[1] K. Takahashi et al., "Wide bandgap semiconductors: fundamental properties and modern photonic and electronic devices", Springer (2007), ISBN-13 978-3-540-47234-6

[2] T. Kimoto et al., "Fundamentals of silicon carbide technology", John Wiley & sons (2014)

2. Main aspects of Silicon Carbide

2.1 Introduction and brief history

Silicon carbide (SiC) is a stable compound in the binary phase diagram of the group IV elements of the periodic table. It is a wide, indirect band gap semiconductor, and it shows optimum physical and chemical stability, even in harsh environments. Inside the wide bandgap semiconductor panorama, silicon carbide is one of the most investigated materials by the scientific community due to its higher potentiality to reach market maturity in a wide field of device applications.

SiC itself is rare in nature, and synthesis of a compound material containing silicon–carbon bonds was first reported by a Swedish scientist, Jons Jakob Berzelius (see ref [1]) in 1824: as a curiosity in the same year he also discovered elemental silicon. The first important mechanical property pointed out in SiC was its great hardness, of about 9.5 points on the Mohs scale (where the maximum is reached by the diamond with 10 points). For this reason, in the years immediately following its discovery, SiC found a commercial market as abrasive under the name of Carborundum, contraction of the two words carbon and corundum (or alumina, another widely used abrasive material). In the recent past, but also nowadays, SiC was used as fireproof material for high-temperature ceramics and also as resistive heating element utilized in silicon device manufacturing. In the first years of the 20th century, the British scientist Joseph Henry Round discovered that pieces of silicon carbide emitted light when an electric current

Figure 2.1: Silicon carbide (SiC) monocrystal from the LMGP (Minatec) lab of Grenoble. Author: David Monniaux. Source: Wikipedia (en).

passed through them. In these years, its rectifying properties were also discovered and, notwithstanding the high turn-on voltage, crystal detectors made with this material were used in that period in the first applications on radio-telecommunication under the name of Carborundum.

After this promising period, however, SiC was progressively abandoned as semiconductor material, due to the focusing of the interest of the semiconductor community on the more attractive silicon and germanium materials, during the 1930s. Only around the 1970 silicon carbide was investigated again from the scientists, looking for semiconductor materials suitable for light emitting diodes (LED) in the

blue range of the visible spectrum, but also in this case it was rapidly abandoned and replaced by direct band gap semiconductors, like the III-nitride group ones (GaN, etc…). Nevertheless, the action for obtaining SiC bulk boules of better and better crystalline quality and SiC epitaxial layers approaching the electronic quality continued under the driving need of high power electronic applications for which SiC still was the most promising and robust semiconductor.

In the last decade, the intense research activity on SiC materials and devices, led to the commercial availability of high quality and high purity silicon carbide material

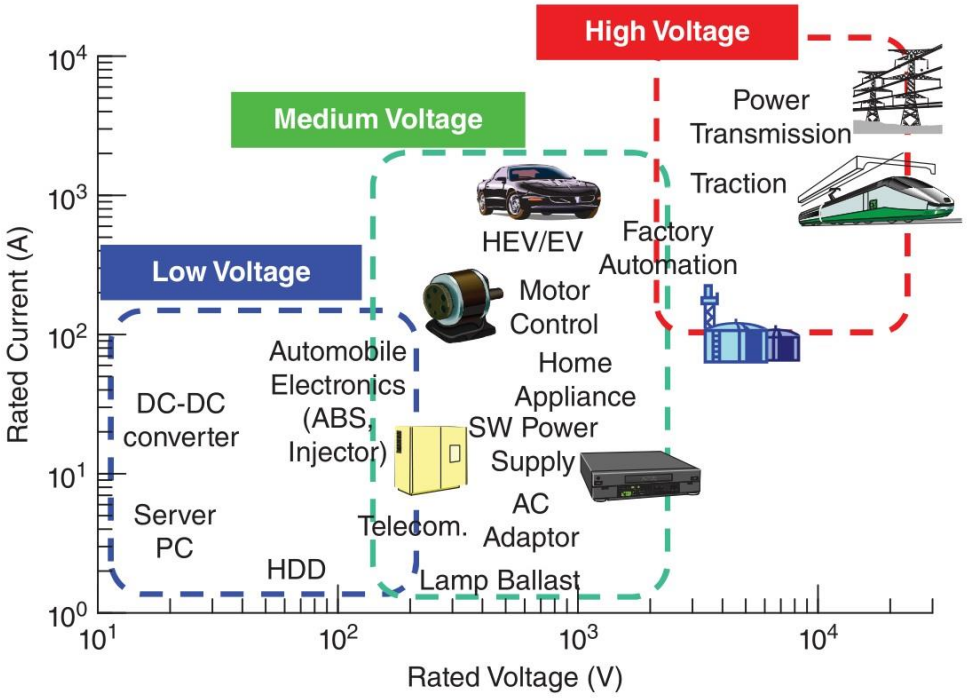

Figure 2.2: Major application fields of SiC power electronic devices as a function of the related voltage. Silicon carbide finds its application in medium and high voltage sectors, especially in power transmission and transport.

and to the commercialization of both silicon carbide components or systems including SiC components. In fact, the advantages given by the use of SiC components in power systems largely compensate the major cost of the these devices with respect to the equivalent devices in silicon.

Now days, Silicon Carbide is widely tested for power transmission applications (see figure 2.2), in particular in electronic power conversion. Other interesting application fields of this material concern telecommunications, motor control, electric and hybrid vehicles, robotics, heating, but also others. Furthermore, for high-voltage bipolar device applications, SiC shows a longer carrier lifetime, in comparison with other promising wide band gap materials like gallium nitride (GaN). This is mainly due to its indirect band structure. Another very recent application field for SiC is the biomedicine and biomedical engineering: in fact, silicon carbide is also biocompatible and it is investigated as a promising material for biosensors, bioMEMS, etc… (see for more information [2]).

2.2 Material properties

The crystallization of silicon carbide is in the form of silicon-carbon bilayers, with a bond length of about 1.9 Å, the average between the Si-Si bond in crystalline silicon and the C-C bond in diamond. In SiC, such bilayers are closely packed, but this

material shows the property of a large variation in crystal lattices, which are all built up by these stacked bilayers. This property is called polymorphism while the various crystalline phases are called polytypes. Polymorphism is observed also in some III-nitride and II-VI compounds.

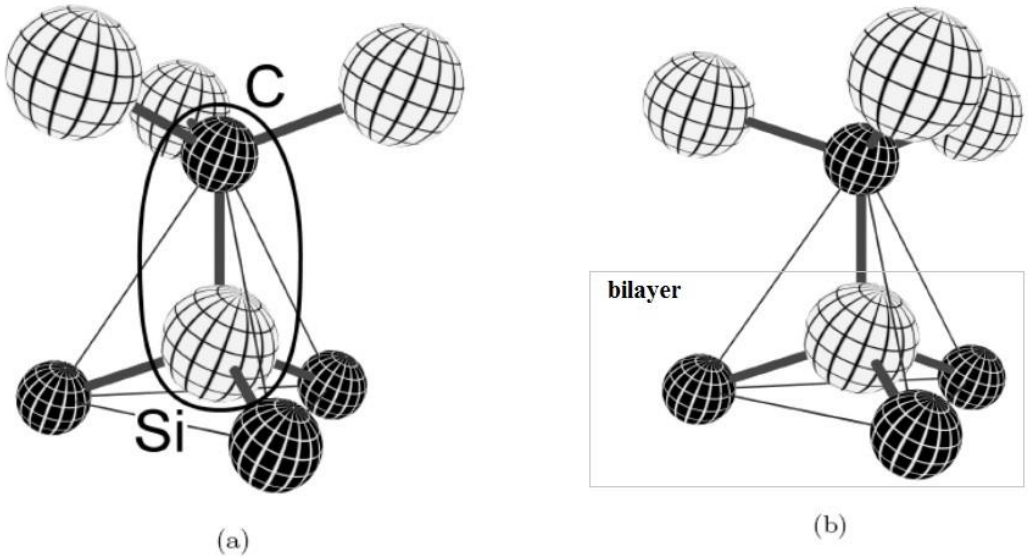

Figure 2.3: Cubic (a) and hexagonal (b) lattice site for silicon (light spheres) and carbon atoms (dark spheres) in the silicon carbide crystal lattice.

As it's possible to see in figure 2.3, a different stacking sequence results in inequivalent crystal lattice sites, of cubic and hexagonal symmetry, respectively.

The different crystal structures can be identified by their characteristic stacking sequences, and the lattice order can be written as a letter sequence (A for the base layer, B, C etc… for the following layers until a complete description of the structure). A common notation was introduced (and take his name) by Ramsdell (see ref. [3]): in this notation, the letters *C*, *H* and *R* are used to indicate, respectively, the cubic,

hexagonal and rhombohedral symmetry of the crystal lattice; the letters are then followed by the number of layers in the stacking sequence (for example: 4H silicon carbide, indicates a hexagonal crystal structure and four layers in the stacking sequence). The main polytypes are:

- **2H –** With the stacking sequence AB, this is the purely hexagonal structure (wurtzite): all lattice sites show hexagonal symmetry (figure 2.3b). This polytype, however, shows very little technological interest so far, mainly due to the difficulties in its growth

- **3C –** This is the cubic zincblende structure with the stacking sequence ABC. Like for gallium arsenide (GaAs), all lattice sites show the same cubic

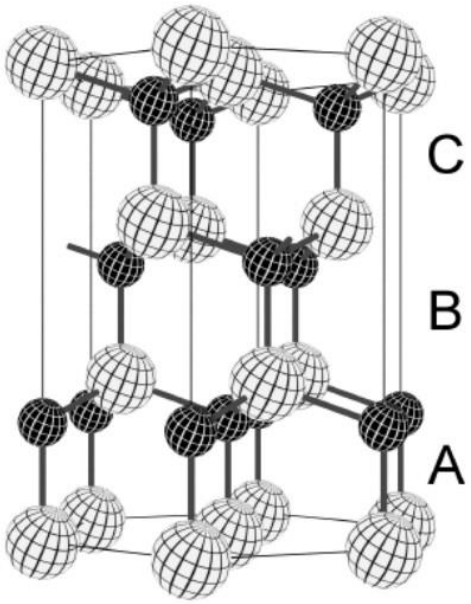

Figure 2.4: The 3C crystal lattice of silicon carbide. It consists of a repetition of Si-C bilayers stacked in a ABC sequence along the [111] axis. The cubic lattice constant is a=4.36 Å.

symmetry of figure 2.3a. In figure 2.4 a scheme of the crystal lattice of this polytype.

- **4H –** The stacking sequence of this polytype is ABAC, it is currently the most investigated polytype for power electronic devices, mainly due to its wider bandgap (about 3.26 eV at RT, see for example ref [4]) and isotropy of the electrons and hole mobility in the <0001> basal plane with respect to other

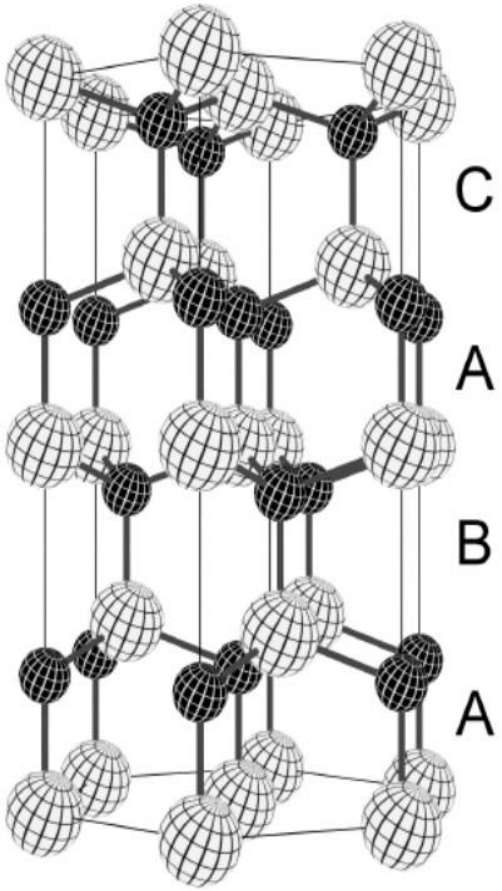

Figure 2.5: The 4H-SiC crystal structure. The lattice is formed by a repetition of Si-C bilayers in the stacked sequence ABAC with lattice constants a=3.08 and c=10.08.

polytypes. It show a proportion of cubic and hexagonal lattice sites of 50%-50%, a scheme of its crystal structure is reported on figure 2.5. The samples investigated in this thesis are made of the 4H-SiC polytype

- **6H –** The first polytype available as single-crystalline wafers, it shows a stacking sequence ABCACB. It presents a higher anisotropy of its parameters with respect to 4H-SiC, and also a slightly lower bandgap of about 3 eV. 2/3 of the sites of the crystal lattice are cubic, the other 1/3 are hexagonal.

This is only a selection of the different polytypes which silicon carbide can reproduce during growth, other longer stacking sequences has been identified, showing the tendency of this material to form highly anisotropic crystals. In table 2.1, the main physical properties of this material are reported and compared with other important semiconductor materials. Note that, in comparison with silicon, 4H-SiC shows a ten times higher breakdown field and a more than three times higher thermal conductivity at room temperature. These aspects are very important for high power applications, allowing a consistent reduction of the device dimensions with respect to Si-based devices and providing a more efficient dissipation of heat around room temperature.

	RT Energy gap (eV)	Breakdown field (MV/cm)	RT electron mobility (cm^2/Vs)	RT hole mobility (cm^2/Vs)	RT Thermal conductivity (W/cmK)
Si	1.12 ind.	0.3	1350	480	1.5
Ge	0.66 ind.	0.1	3900	1900	1.6
3C-SiC	2.4 ind.	2.0	1000	40	4.9
4H-SiC	3.26 ind.	3.0	1000	120	4.9
GaN	3.4 dir.	3.3	1000	30	1.6

Table 2.1: Main physical parameters of common semiconductor materials. For the room temperature (RT) energy gap is also reported the direct (dir.) or indirect (ind.) character. The 4H-SiC, shows a ten times higher breakdown field and a three times higher thermal conductivity with respect to Si.

Furthermore, silicon carbide is a polar material, and when it's cut perpendicularly to the c-axis (i.e. the direction of stacking sequences, the <0001> direction) it shows polar surfaces, in which the top layer is covered by silicon or carbon atoms (Si- and C-faces respectively).

2.3 Material Growth and structural defects

Silicon carbide, unlike other common semiconductor materials, does not show a liquid phase. For this reason, the only way to synthesize and grow silicon carbide materials for device processing is from gaseous phases. The commonly used techniques for electronic-grade SiC growth are: (i) the Physical Vapor Transport (PVT), where a solid SiC source is evaporated at high temperatures, and vapors crystallize in a colder part of the reactor, and (ii) the Chemical Vapor Deposition (CVD), where gas-phase precursors containing silicon and carbon react, and silicon carbide is solidified on the target. The commonly used technique for the epitaxial growth of this material is the vapor-liquid-solid (VLS) one (see ref [5] for example). This technique is based on a combination of liquid phase epitaxy (LPE) and CVD. Carbon is supplied in form of gas that contains it (propane for example, C_3H_8). Gas cracks upon heating, and carbon first dissolves in the melt and then migrates to the substrate, driven by the gradient of its concentration between the top and the bottom of the liquid. When carbon reaches the substrate, it reacts with Si atoms from the solvent forming a SiC layer.

The bulk growth of silicon carbide, instead, is mainly provided by the seeded sublimation method, also known as the modified Lely method (see for example ref. [6]). A simple scheme of this method is reported on figure 2.6: a graphite crucible is placed in a low pressure atmosphere of an inert gas and heated at very high temperatures (2300°C or higher). A single crystal seed is put at the top of the crucible, while a SiC source (usually SiC powder) is placed at the bottom. The sublimation into Si and C separated atoms of the source is provided by the high temperatures, and these

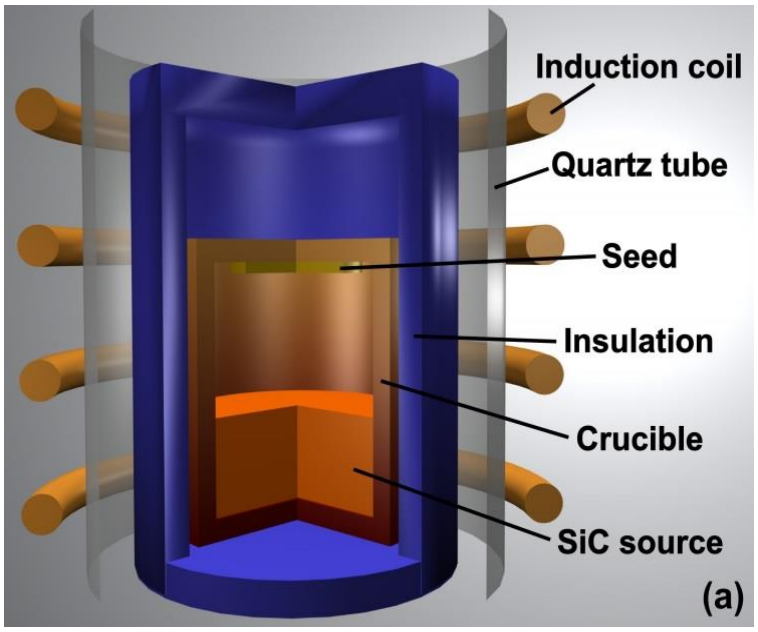

Figure 2.6: a simplified scheme of the modified Lely process.

species are transported to the seed, and so the growth begins. The driving force in this case is provided by a temperature gradient between the source and the seed. The main advantage of this technique is the high growth rate. Such a growth method allows to obtain high quality bulk silicon carbide crystals. Negative aspects, instead, are mainly

related to the impossibility to supplement source material during growth: for this reason, the thickness of the grown material is controlled by the initial quantity of the source material and longer growth finds difficulties in the control of the partial pressures, because the Si/C ratio changes during the process and causes instabilities.

These growth techniques are not the only possible ones for epitaxial and bulk growth, and the research for crystal growth improvements is active nowadays to provide higher growing rates, larger SiC wafers but also to reduce unwanted defects concentration: as usually said, perfect crystals do not exist. The main defects that can be found in high quality silicon carbide crystals are stacking faults, twin boundaries and polytypic inclusions.

Stacking faults (SFs) defects are a variation of the particular stacking sequence of a SiC polytype. For example, the stacking sequence of the 4H-SiC polytype (ABAC) can change during the growth along the c-axis (becoming for example ABABAC). This is a common defect in close-packed structures such as SiC due to their low formation energy, they can also appear in bunches and not only isolated and introduce other polytype stacking. For more details on stacking faults and their impact on device performances see for example ref. [7]. Other common defects in silicon carbide are the twin boundaries (TBs). The term *twin* refers to two crystal domains composed by the same crystal structure but with a different orientation, usually they look like a mirror reflection of the crystal structure (see figure 2.7).

The twin boundary between two domains is an extended defect with high formation energy, and it can also relax causing the formation of stacking faults; they are

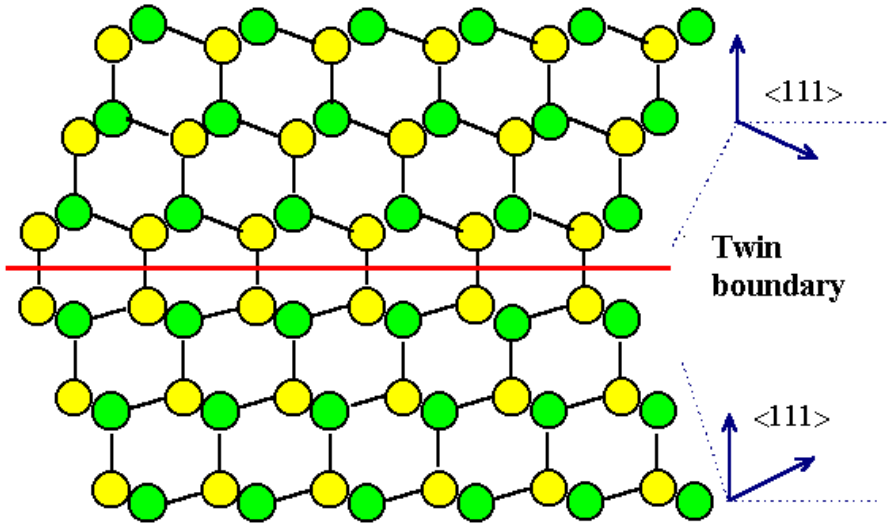

Figure 2.7: example of a twin boundary defect in a crystal structure.

detrimental for devices performances, and so they are highly not desired. The polytype inclusions, instead, typically appear in epitaxial growth as a defect. During the growth of a particular silicon carbide polytype, a different polytype growth can occur. Typical for 4H-SiC, 3C-SiC inclusions form, mainly due to a non-uniform substrate or to the growth condition used (see ref. [8]).

In an old past, the most important defect in bulk SiC was the micropipe (MP). It is commonly accepted that MP is a pure screw dislocation with giant Burgers vector along the c-axis direction (see for example ref. [9]). Two types of MP defects are reported in literature (see ref. [10]): one with a diameter >1 μm lying approximately long the [0001] axis, which can extend over long distance (up to several centimeters), and the other (generally < 1 μm) which can lie at highly oblique angles to the [0001] crystal growth axis, with short ranges and starting and terminating abruptly (see figure 2.8). Also this kind of defect is clearly very detrimental to electronic device

performances, causing premature breakdown point failure. Nowadays, however, the commercially available silicon carbide is completely free of these defects in off-axis substrates and with densities lower than 10 cm^{-2} in on-axis ones (see for example CREE® catalogue [11]).

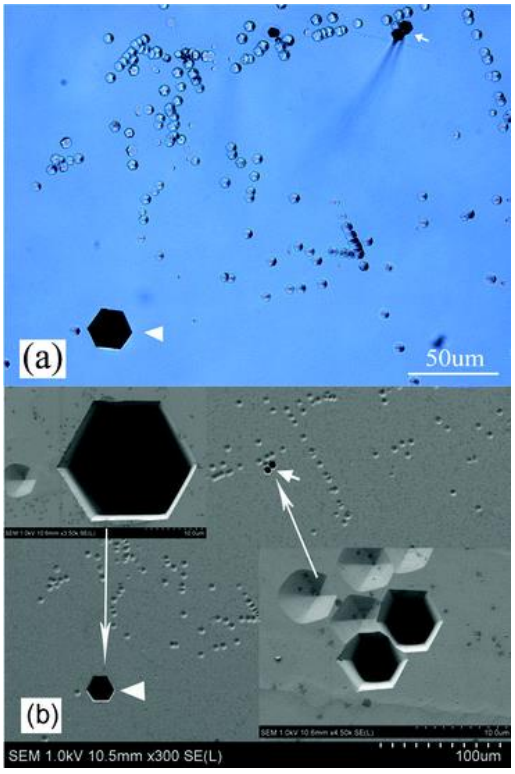

Figure 2.8: OM (a) and SEM (b) images of a 4H-SiC wafer showing micropipe defects.

Silicon carbide wafers became available in the recent years from an increasing number of manufacturers, and over the years they were available in larger diameters and with improved crystal quality.

2.4 Band structure of silicon carbide

The Brillouin zones (BZ) of cubic and hexagonal silicon carbide polytypes are shown in figure 2.9, as like as the electronic band structures of 3C-, 4H-, and 6H-SiC from left to right. The height of the Brillouin zones of the different hexagonal polytypes changes due to a different value of the lattice parameter *c*. All SiC polytypes show an indirect band structure: the top of the valence band is located at the Γ point of the BZ,

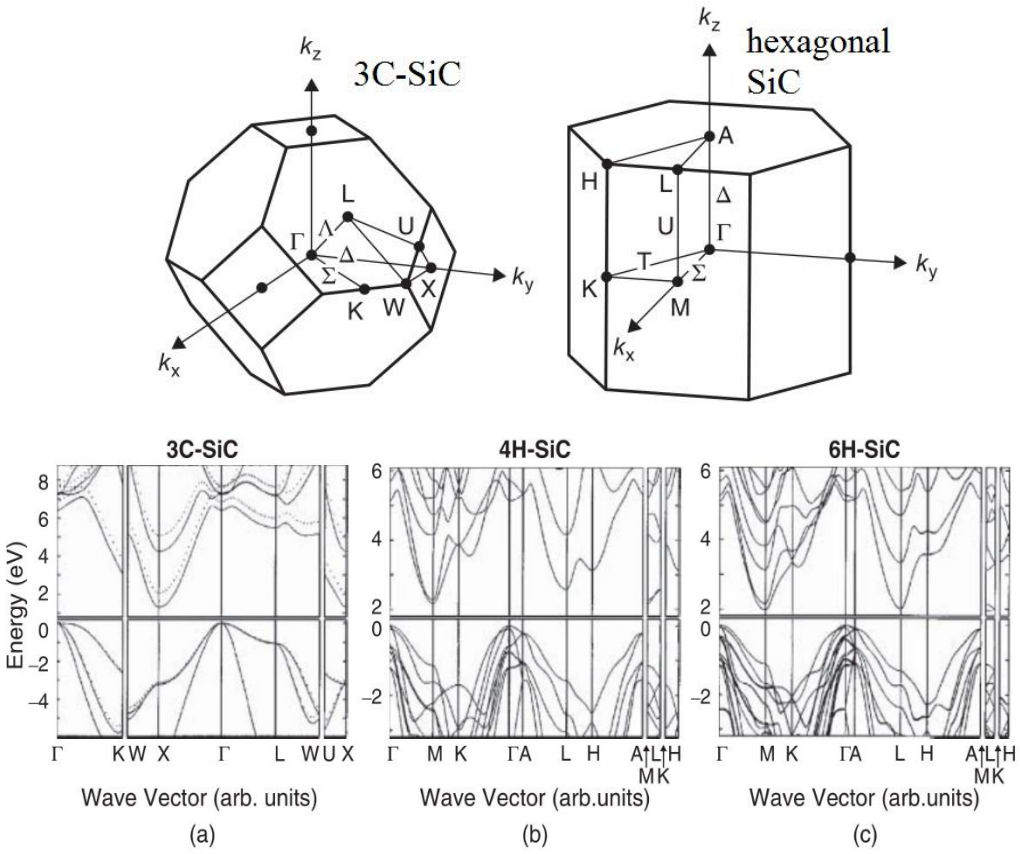

Figure 2.9: Brillouin zones (top) of cubic and hexagonal SiC polytypes and electronic band structures (bottom) of 3C-SiC (a), 4H-SiC (b) and 6H-SiC (c). Absolute values of bandgaps are slightly underestimated due to limitations of theoretical calculations.

while the minima appear at the boundary of it. They can be found at X point for 3C-SiC, at the M point for 4H-SiC and at U point (along the M-L line) for 6H polytype. The room temperature (RT) value of band gap of the 4H polytype is about $E_g=3.26$ *eV*. The number of conduction band minima in the first Brillouin zone is 3 for both 3C and 4H polytypes, while for 6H-SiC is 6. The valence band structure instead is similar for all polytypes because Si-C covalent bonds are common for all polytypes; however, variations can be found for the splitting. For example, for 3C-SiC the valence band is doubly degenerate, as a consequence of the cubic symmetry, and the next valence band is shifted 10 meV from the top by the spin-orbit interaction. The crystal field, present in hexagonal polytypes, splits the valence band degeneracy, and in 4H-SiC the magnitudes of the spin-orbit splitting and crystal-field splitting are respectively of 6.8 and 60 meV (see ref. [12]).

Table 2.2 summarizes the effective masses of electrons and holes for 3C, 4H and 6H-SiC: the electron effective mass depends on the polytype, leading to variations of the electron mobility. Figure 2.10 reports a simple scheme of the band edges of 4H-SiC, the polytype adopted in this work. For more details on the band structure of silicon carbide see for example refs. [13] and [15].

Polytype	Effective mass	Experiment (m_0)	Theory (m_0)
Electron effective mass			
3C-SiC	$m_{//}$	0.667	0.68
	$m_{\perp}$	0.247	0.23
4H-SiC	$m_{ML}(=m_{//})$	0.33	0.31
	$m_{M\Gamma}$	0.58	0.57
	m_{MK}	0.31	0.28
	$m_{\perp}(=(m_{M\Gamma}m_{MK})^{1/2})$	0.42	0.40
6H-SiC	$m_{ML}(=m_{//})$	2.0	1.83
	$m_{M\Gamma}$	–	0.75
	m_{MK}	–	0.24
	$m_{\perp}(=(m_{M\Gamma}m_{MK})^{1/2})$	0.48	0.42
Hole effective mass			
3C-SiC	$m_{\Gamma X}(=m_{[100]})$	–	0.59
	$m_{\Gamma K}(=m_{[110]})$	–	1.32
	$m_{\Gamma L}(=m_{[111]})$	–	1.64
4H-SiC	$m_{//}$	1.75	1.62
	$m_{\perp}$	0.66	0.61
6H-SiC	$m_{//}$	1.85	1.65
	$m_{\perp}$	0.66	0.60

Table 2.2: Effective masses of electrons and holes in 3C, 4H and 6H polytypes. Both experimental and theoretically calculated values are reported, in unit of electron mass m_0 (see ref [13]).

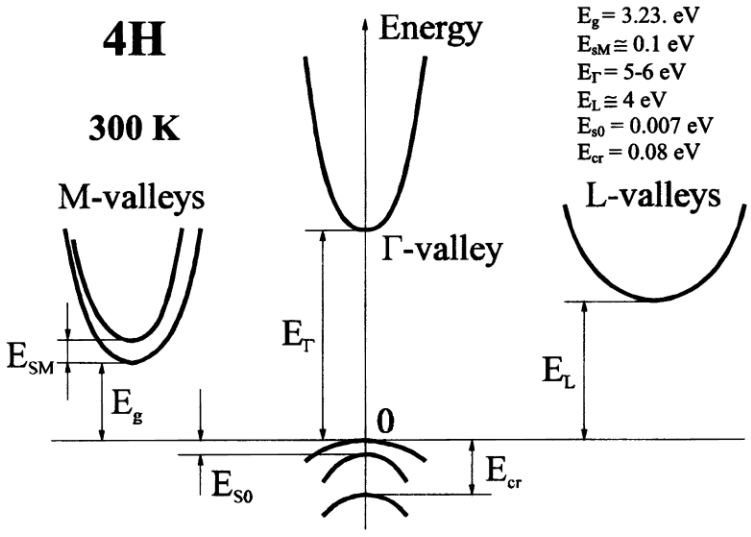

Figure 2.10: scheme of the band edges and related energy separations in 4H-SiC at RT (see ref. [14]).

2.5 Doping of silicon carbide

Silicon carbide can be efficiently doped with donor and acceptor impurities, inducing n- or p-type conductivity, respectively. However, due to the presence of inequivalent lattice sites for the same substitutional impurity and a biatomic base, a given species of incorporated impurity atoms is expected to give rise to two fundamental energy levels. Main p-type dopants for this material are boron and aluminum: from the reaction kinetics during crystal growth with dopant incorporation and from the results of other different investigation techniques it was discovered that these acceptor impurities are preferably incorporated on the silicon site of the crystal lattice (see ref. [16]). The main n-type impurities are, instead, nitrogen and phosphorus: nitrogen tends to occupy the carbon lattice site, while phosphorus preferably occupies the silicon one. Figure 2.11 reports a simple scheme of the thermal ionization energy of a selection of donors and acceptors in 4H-SiC. It is worth noting that two significantly different energy values are observed for the donor impurities, corresponding to the impurity incorporation into either cubic or hexagonal sites. Nitrogen for example shows ionization energies of about $E_C - E_N^{cub} = 102meV$ and $E_C - E_N^{hex} = 59meV$ in cubic and hexagonal sites respectively. A similar splitting, instead, is controversial for the acceptor impurities (see ref. [17], [18] and [19]), which are also characterized by higher values of the thermal ionization energy with respect to donors, owing to the higher effective masses of the valence band (VB) top in respect to the conduction band (CB) minimum. In particular, Boron shows an ionization energy of about $E_B - E_V \cong 290 - 390\ meV$, a value higher than the expected one for a hydrogenic acceptor. For this reason, during last years, aluminum became the favorite p-type dopant in silicon carbide device technology, with an ionization energy of about $E_{Al} -$

$E_V \cong 200\ meV$. For more details on the ionization energies in 4H-SiC, see for example ref. [17], [18] and [19]. The ionization energies of both donors and acceptors are expected to decrease with the increasing of their concentration and/or compensation (see ref. [20]), resulting in a spread of values reported by the literature.

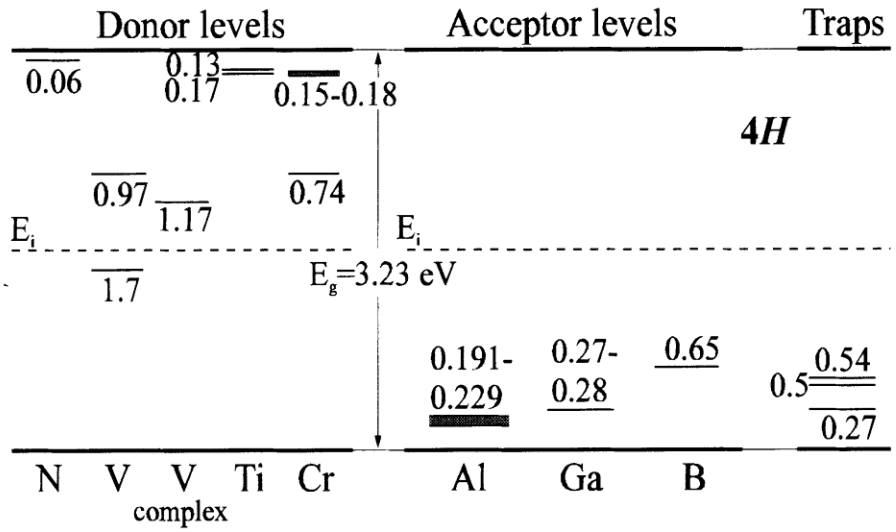

Figure 2.11: main donors and acceptors in 4H silicon carbide and their energy depth with respect to the related band edge. The Al acceptor, used for the samples of this investigation, is main adopted one during recent years. See ref [21] and related citations.

This phenomenon is attributed to a fluctuation of the local potential due to long range interaction amongst charged impurities: it affected extended states and impurity ground states, by spreading the latter into an impurity band and then reducing the energy separation between bounded to extended states.

The thermal ionization energies reported above show that even the shallow dopant ionization levels in silicon carbide are deep, if compared with those reported for other traditional semiconductors like germanium or silicon. This brings to an incomplete ionization of these impurities at RT, particularly for the acceptor dopants.

2.6 References of this chapter

[1] J.J Berzelius, Annalen der Physik 1, p.169 (1824)

[2] S. E. Saddow, "Silicon Carbide Biotechnology: A Biocompatible Semiconductor for Advanced Biomedical Devices and Applications", Elsevier (2002)

[3] L. S. Ramsdell, "Studies on Silicon Carbide", American Mineralogist 32, p. 64-82 (1947)

[4] C. Persson et al., "Relativistic band structure calculation of cubic and hexagonal SiC polytypes", Journal of Applied Physics 82, 11 (1997), 5496-5508

[5] D. Chaussende et al., "Vapour-liquid-solid mechanism for the growth of SiC homoepitaxial layers by VPE", Journal of Crystal Growth, vol. 234 (2002) p. 63-69

[6] V. D. Heydemann et al., "Growth of 6H and 4H silicon carbide single crystals by the modified Lely process utilizing a dual-seed crystal method", Applied Physics Letters 69, 3728 (1996)

[7] H. Fujiwara et al., "Characterization of in-grown stacking faults in 4H–SiC (0001) epitaxial layers and its impacts on high-voltage Schottky barrier diodes", Applied Physics Letters 87, 051912 (2005)

[8] J. A. Powell et al., "Controlled growth of 3C-SiC and 6H-SiC films on low-tilt-angle vicinal (0001) 6H-SiC wafers", Applied Physics Letters 59, 333 (1991)

[9] P. G. Neudeck et al., “Performance limiting micropipe defects in silicon carbide wafers”, Electronic Device Letters 15 (1994) p. 63-65

[10] C. J. Liu et al., “Formation mechanism of Type 2 micropipe defects in 4H–SiC crystals”, CrystEngComm 15 (2013), 1307

[11] http://www.cree.com/~/media/Files/Cree/Chips-and-Material/Data-Sheets-Material/MATCATALOG.pdf

[12] S. G. Sridhara et al., “Differential Absorption measurement of valence band splittings in 4H SiC”, Material Science Forum, vol. 338-342, p. 567-570

[13] W.R.L. Lambrecht et al., “Electronic band structure of SiC polytypes: A discussion of theory and experiment”, Phys. Status Solidi B, 202, 5 (1997)

[14] C. Persson et al., “Relativistic band structure calculation of cubic and hexagonal SiC polytypes”, Journal of Applied Physics 82, 11 5496-5508 (1997)

[15] P. Käckel et al., “Electronic properties of cubic and hexagonal SiC polytypes from ab initio calculations”, Physical Review B, 50, 10761 (1994)

[16] D. J. Larkin et al., “Site-competition epitaxy for controlled doping of CVD silicon carbide”, Institute of Physics Conf. Series 137: Silicon Carbide and Related Materials, pp. 51-54 (1994)

[17] I. G. Ivanov et al., “Ionization energies of phosphorus and nitrogen donors and aluminum acceptors in 4H silicon carbide from the donor-acceptor pair emission”, Physical Review B 71, 241201(R) (2005)

[18] S. R. Smith et al., “Shallow acceptor levels in 4H- and 6H-SiC”, Journal of Eletronic Materials 28, issue 3, p. 190-195

[19] G. Pensl et al., “Electrical and optical characterization of SiC”, Physica B: Condensed Matter 185, issue 1-4, p. 264-283 (1993)

[20] A. Schoner et al, “Dependence of the aluminum ionization energy on doping concentration and compensation in 6H-SiC”, Institute of Physics Conferences Series n° 142, p. 493-496 (1996)

[21] http://www.ioffe.ru/SVA/NSM/Semicond/SiC/impurities.html

For more details on the aspects showed in this chapter see for example:

- G. L. Harris, “Properties of Silicon Carbide”, Inspec (1995)
- T. Kimoto et al., “Fundamentals of Silicon Carbide Technology”, Wiley (2014)
- S. E. Saddow, “Silicon Carbide Biotechnology: A Biocompatible Semiconductor for Advanced Biomedical Devices and Applications”, Elsevier (2002)

3. Discussion on the work

3.1 State of the art and motivation of the work

As it was shown in the previous chapter, silicon carbide is a promising material amongst the wide bandgap semiconductors, and its properties make it an ideal material for many applications, especially for high power devices. However, there are several issues with the processing technology that need to be resolved to improve the device production with this material on industrial scale and to expand the market share of the devices. One of the most important processing step that need an optimization is the selected volume doping of SiC, for planar device fabrication. A good control of the doping process in both bulk crystals and epitaxial layers can be performed in-situ during the growth process, carried out, for example, by chemical vapor deposition. However, this implies the set-up of a reliable technology for the epitaxial growth inside etched trenches for the aim to obtain devices of planar geometry. Impurity diffusion and ion implantation are the alternative technologies to obtain laterally adjacent volumes of opposite conductive sign.

In silicon carbide, however, the thermal diffusion of impurities is not a suitable doping process, because it requires extremely high temperatures. This is mainly due to the low atomic mobilities in SiC: to obtain reasonable diffusivities (higher than 10^{-13} cm^2/s), temperatures of at least 1800°C are required for most elements (see ref. [1]). Amongst light elements, with small atomic radius (hydrogen, lithium etc…), only the

boron dopant shows significant diffusion under equilibrium conditions at temperature lower than 1800°C (see for example ref. [2]).

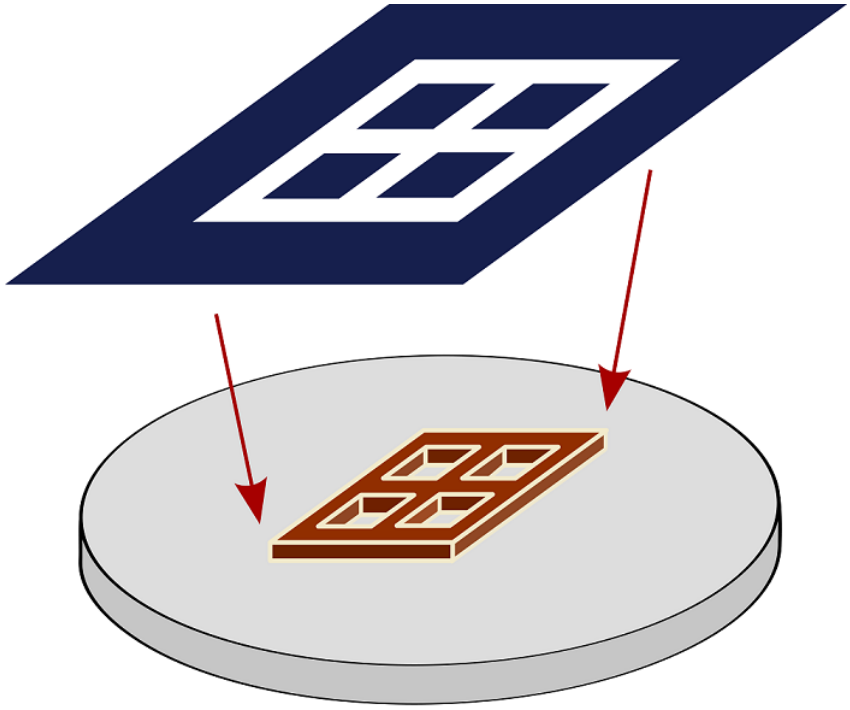

Figure 3.1: a simple scheme to clarify the meaning of selective area doping by the utilization of a mask.

For these reasons, ion implantation is the only practical method to perform a selective and planar area doping in silicon carbide. The ion implantation process will be described in the next paragraph of this chapter, however, in simple words, it consists in a process where high-speed ions of the element that needs to be implanted are injected inside the near-surface region of the target material. One of the main advantages of implantation technique is that the obtainable concentration of dopant can overcome the solubility limit of the species in the material, because this process is a non-equilibrium phenomenon; further, almost every element of the periodic table

can be implanted. Moreover, it gives a very good control over the depth profile distribution, allowing the realization of shallow junctions, buried doped regions, box profiles, etc. The doping of selected regions is obtained thanks to proper implant masks that block ions from penetrating into the semiconductor volume through the semiconductor surface exposed the ion beam (see figure 3.1).

However, there are two main issues concerning this doping technique: first of all, just after implantation, implanted ions lie not in substitutional position and so they are not electrically active, moreover, the ion bombardment seriously damage the crystal lattice, especially at high implanted doses, and damaged lattice needs to be recovered. Both these problems can be (at least partially) resolved by heating implanted material, i.e. by performing a post implantation thermal annealing of the implanted semiconductor wafer. Temperature, duration, heating and cooling transient of such an annealing process must be optimized with respect to the desired electrical activation of the implanted species. Depending of the desired annealing cycle different heating technologies have to be used. As examples it may be cited the facts that ultra-fast heating cannot be obtained by conventional resistive furnaces while cooling rate is determined by the thermal inertia of the sample holder.

High concentrations of dopant in selected areas of the sample can be required for specific applications, if locally very low material resistivity is desired. An example is given by the fabrication of ohmic contacts of low specific contact resistance, with values independent of the temperature. However, when this concept is applied to p-type contacts, the process must account for difficulties due to the material properties. In particular, the high ionization energies of p-type dopant species in 4H-SiC (about 200 meV for Al) hinders the lowering of resistivity, because this feature leads to a significant freezing out effects even at RT. On the other hand, the possibility to take

advantage of the transition to a metallic behavior is made difficult by the high value of the critical density for the insulator-to-metal transition. Such a transition has been reached, till now, only in epitaxial samples, and observed for a dopant concentration of about 6-8×10^{20} cm^{-3} (see ref [3]). Ion implantation remains the most powerful method to fabricate ohmic contacts of controlled area and very low specific resistivity.

The approach adopted over the years to obtain lower and lower resistivity in 4H-SiC has been the increasing of both the volume density of the implanted dopant and the temperature of post implantation thermal treatments, necessary for the electrical activation of the impurities. In the case of aluminum, the implanted concentration and post implantation annealing temperature have reached, respectively, the low 10^{21} cm^{-3} decade, and the 1800°C value (see ref. [4] and [5]). In this research, an original approach was explored by using very high annealing temperatures, up to 1950-2000°C (see next pages), on samples with Al^{+}-implant concentration of the order of 10^{20} cm^{-3}. The aim was the enhancement of the electrical activation of dopants by reducing, at the same time, the implanted impurity concentration, in order to limit the amount of disorder introduced in the lattice. To evaluate doping and compensation, and to investigate the electrical properties, such samples are generally studied by Hall effect and resistivity measurements in a wide temperature range. In implanted semiconductors, this technique permits to check the effectiveness of implantation and annealing processes, by evaluating the efficiency of the impurity electrical activation. In addition, the transport mechanisms controlling the electrical conduction of the layers can be investigated.

Such high implantation doses and annealing temperatures, however, could create traps in non-negligible concentration inside the material. For this reason, in the last part of the work it was developed an automated acquisition system for Admittance

Spectroscopy (AS) and Current-Voltage (C-V) measurements (see chapter 4) for a preliminary electrical investigation on simple 4H-SiC test devices as p^+/n junctions and Schottky barriers. In this case, a heavy Al^+ ion implantation was realized on n-type epilayers, according to the technological process applied for final devices. Thanks to this investigation and also Deep Level Transient Spectroscopy investigation (DLTS) the presence of electrically active defects was studied, with the aim to detect possible traps, induced in the active region of the devices by ion implantation and/or the high temperature thermal treatments.

3.2 Ion implantation

As it was said before, ion implantation is a process consisting in high velocity ion injected into the near surface region of a target material. It allows the implantation of almost all the elements of the periodic table with a precise control over their concentration and depth profiles, and a target can be selectively implanted thanks to the using of implant masks.

A ion implantation system is usually composed of a high-voltage particle accelerator that create a high velocity beam of ions which hits the surface of the target material that have to be implanted. In figure 3.2 is showed the basic scheme of a ion implanter where are showed its main components consisting in:

- **Ion source:** From a feed gas or a solid charge, which are the sources of the implant species, a plasma of the desired ion impurities is produced thanks to a high voltage. In the case of solid charges, material is heated and the produced vapor is used as ion source. This vapor, or the feed gas, are broken down into a variety of atomic and molecular species with the help of a plasma glow discharge, where they are ionized (see ref. [6]). Only the specie with the desired charge is selected: if the charge of the required ions is positive, for example, the exit is biased with a large negative potential with respect to the filament, and only the beam of positive ions leaves the system.

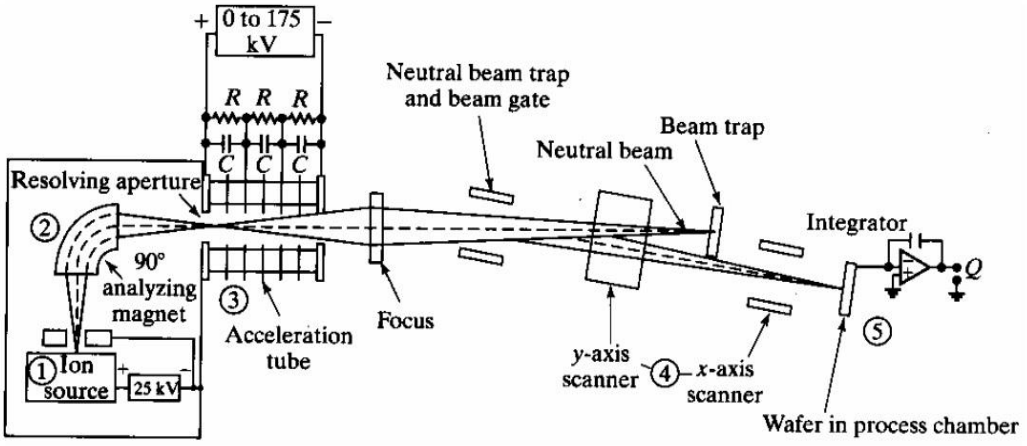

Figure 3.2: scheme of an ion implantation system. It mainly consists in a ion source (1), a mass spectrometer (2), a ion electrostatic accelerator (3), a beam scanning system (4) and the end station (5) where the target is positioned.

- **Mass spectrometer:** After reaching the exit of the ion source, the beam is composed by a variety of species, most of which are ionized. Thanks to an analyzer magnet, the desired impurity is separated from other species by their

different masses. The analyzer magnet bends the beam through a right angle (a magnetic field perpendicular to the beam velocity is present) and the selected specie is passed through an aperture slit to the main accelerator column.

- **Accelerator:** The accelerator provides to the beam the desired energy based on the required penetration depth, and accelerates the ions at the proper velocity. The required maximum voltage depends on the desired penetration depth of the ions into the target material. The accelerator column is typically several meters and it is kept in high vacuum to avoid ion collisions during the acceleration phase.

- **Scanning system:** the ion beam is rasterized with the help of x- and y- axis deflection plates. This guarantee uniform ion implantation across the target sample. In order to avoid the implantation of neutral particles, which may have been produced during the acceleration phase, the beam is slightly bent.

- **End station:** it is the space where the target sample is placed, inside a vacuum chamber, and its orientation and temperature are set (see ref. [7]). The possibility to set a proper (usually elevated) temperature of the implanted targets is important (i.e. to perform hot implantation), particularly when the implant dose is very high. Without this, the as-implanted lattice damage may result of near-amorphous level, and the lattice recovery results very difficult. Samples investigated in this work are implanted at a temperature in the range 300-500 °C. The precise control of the ion dose is provided, at the and station, by placing a Faraday cup. The cup captures all the entering charges and the

ion current is measured by connecting an amperometer between the cup and the electrical ground. The integration of the current over time, taking also into account the sample area, provides the dose. Since the Faraday cup absorbs all the energy, this measurement is usually made before real experiment.

In figure 3.3, a simple scheme of the implantation process on a crystal is reported. In this picture it is highlighted how the crystal lattice is partially damaged after implantation, and the implanted ions mainly occupy interstitial position and they are electrically inactive.

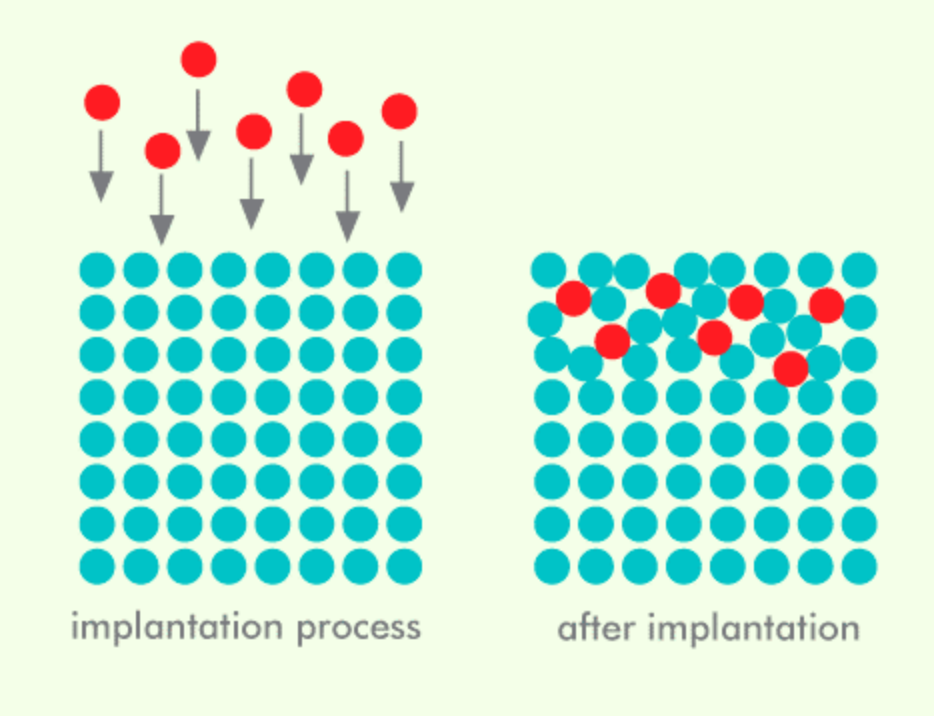

Figure 3.3: a simple scheme of the implantation process. Note that after implantation the crystal lattice is (at least partially) damaged, and the implanted ions are mainly in interstitial position.

The main problems related to ion implantation are the channeling effect and the amorphous layer formation:

- **Channeling effect:** inside a single crystal material, where the atoms are regularly arranged, a space may exists at particular orientations. As showed in figure 3.4, when the ion velocity is parallel to these crystal orientations, the ions can penetrate deeper into the target (see for example ref. [6]). This is called *ion channeling*, where atoms are not subjected to nuclear collisions and thus they can penetrate in depth. Channeling can be avoided by tilting the target sample so that ions enter in the crystal lattice with an angle less than a critical one. The critical angle is the largest angle whereby the steering action of the rows of atoms is lost, and it depends on the energy of the incident beam, the distance between atoms and the charge number of incident and target ions.

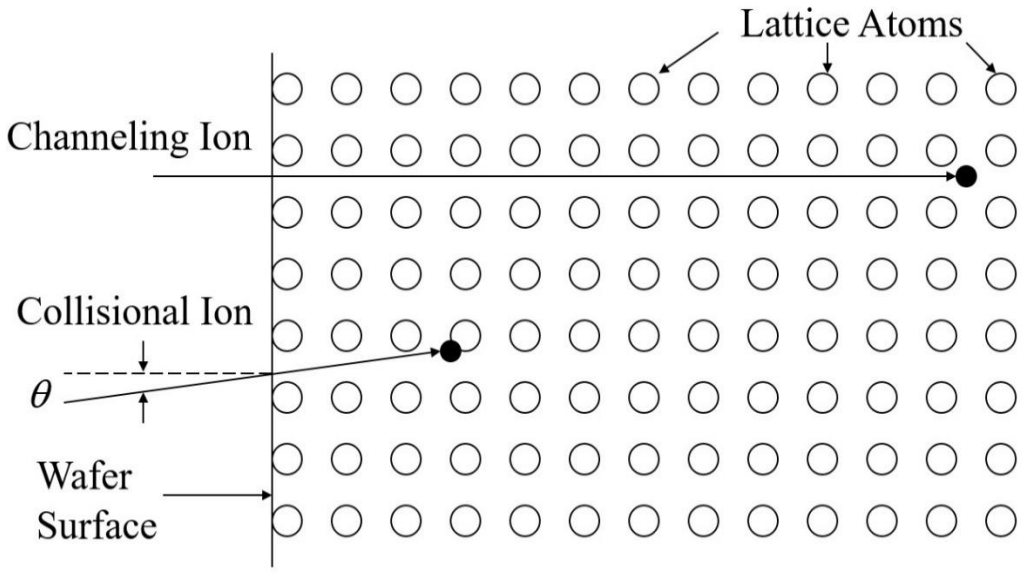

Figure 3.4: scheme of the channeling effect during ion implantation. Without a tilt angle between ion beam and the crystal lattice, ions can deeply penetrate inside the crystal.

- **Amorphous layer formation:** if the implanted dose is sufficiently high, also the damage due to the displacement of the atoms of the target is consequently very high (see for example ref. [8]). The displaced atoms can themselves displace other atoms, causing a collision cascade effect. This brings to an increasing of vacancies and atomic clustering effect, until a creation of an amorphous layer. As it was said before, this problem can be reduced by heating the target sample during implantation: in this way, the implanted surface partially self-anneals. However, in order to recreate the crystal lattice of the target, a post-implantation annealing treatment is required, and performed at even higher temperature. Details on the annealing treatments performed on the samples investigated in this work (up to 1950-2000°C) will be provided in the next pages.

Ion implantation performed with a single energy beam generates a Gaussian profile of the dopant concentration inside the target sample. To obtain the desired shapes of the dopant concentration, for example box-shaped profiles, multiple implantation are required. However, the correct doses and energies of the implanted ions must be known in advance. These informations can be obtained from simulation tools, which allow to determine the ion profile and concentration before the implantation itself. The most widely adopted software tool to predict the energy and the depth of the implant profiles is the Stopping and Range of Ions in Matter (SRIM). SRIM is a group of programs, which elaborate the stopping and the range of implanted ions into the target thanks to a full quantum mechanical treatment of ion atom collisions (see ref. [9]). SRIM was developed by J. P. Biersack and J. F. Ziegler in 1983 and it is distributed under a freeware license. This tool (in the version SRIM2008) was adopted to predict the doping profiles of the implanted samples of this work, and for almost

all samples the obtained implant profiles were verified by Secondary Ion Mass Spectroscopy (SIMS), generally before the thermal treatments. Except for very few samples, a good agreement between the predicted and the measured concentration profiles was observed in the investigated samples. Moreover, when compared with the SIMS profiles after the thermal treatments, equal implant tails were observed confirming a negligible diffusion of Al also after high temperature treatments. Thanks to SIMS measurements, furthermore, is possible to evaluate the thickness of the implanted layer.

The implantation of Al^+ ions on 4H-SiC samples investigated in this work, was performed at Consiglio Nazionale delle Ricerche, Istituto per la Microelettronica e Microsistemi (CNR-IMM Institute) located in Bologna (Italy) by the research group of Dr. Roberta Nipoti. The ion implanter is a Tandentron 1.7 MV accelerator (High Voltage Engineering Europa B.V.), a 3-inches hot holder for sample mounting and heating were used.

3.3 Annealing treatments

After ion implantation process, even if it is performed at high temperatures, a thermal annealing is usually performed on the 4H-SiC Al^+ implanted samples, with the purposes of both recover the damaged crystal lattice and to electrically activate the dopants. While the most part of the damage induced by implantation can be repaired

by annealing at temperatures of about 1200°C, to reach an acceptable electrical activation these temperatures, however, are not enough, and thermal treatments at temperatures higher than 1500°C are required, due to the high strength of the bonding of the silicon carbide lattice. In fact, after ion implantation, the atoms implanted in the target surface are mainly located in interstitial position (see ref. [10]): in this position, they do not behave as intentional dopants, but only as point defects, damaging the crystal lattice and the electrical properties. The incorporation of the impurities at the proper lattice sites, i.e. their placement in substitutional positions, resulting in their electrical activation, is provided by the thermal annealing of the wafer.

It has been observed that the SiC surface is subjected to degradation when high temperature (>1500°C) annealing treatments are performed, both if performed in vacuum or in an inert gas, like argon. Silicon tends to evaporate, leaving a carbon-rich layer on the surface (see ref. [11]). For this reason, the implanted sample surface of the 4H-SiC samples has been protected by a carbon film (C-cap, see ref. [12]). The root mean square roughness of the sample surfaces was verified after annealing treatments by atomic force microscopy (AFM), showing a low degree of roughness in almost all samples.

Over the years, different annealing techniques have been studied for silicon carbide processing. The main way to improve the electrical activation was the increase of the working temperature of thermal treatments. In this work the annealing temperatures of the investigated samples were raised up to 1950°C with a conventional annealing process (CA), and up to 2000°C by using a microwave heating (MWA). A comparison of the results obtained by applying these two methods will be presented in the next chapters.

The conventional annealing treatment on the samples investigated in this work was performed, like the ion implantation, at the CNR-IMM Institute located in Bologna (Italy), by Dr. Roberta Nipoti. A modified Jipelec SiC inductively heated furnace has been adopted to perform a rapid thermal annealing process of 4H-SiC samples up to 1950° with a ramp rate up to 40°C/s, inside a super-pure argon atmosphere. This furnace can operate in the temperature range 700-2000°C, and the temperature control is provided by a pyrometer. The SiC wafer is put inside a graphite susceptor and the annealing process is controlled by a proprietary software.

Figure 3.5: the Jipelec SiC Furnace of Bologna CNR-IMM

The microwave heating of an implanted specimen is obtained by putting this sample faced to an n-type 10^{18} cm^{-3} silicon carbide dummy sample of identical area inside a microwave field. The electrons of the dummy sample absorbs the microwaves and the temperature of the dummy sample increases till 2000°C at the rate of about 600°C/s. . This treatment is performed in forming gas (nitrogen and 10% hydrogen) at 5 atm (inert environment). The implanted sample is heated by conductive heat exchange through the contact of the sample surfaces and the gas atmosphere. The implanted sample follows the same thermal cycle of the dummy sample. To preserve SiC surface a carbon cap has been fabricated on the surfaces of both dummy and implanted specimens. The temperature is monitored by an optical pyrometer. This annealing system was developed by LT Technologies, further details can be found in ref. [11].

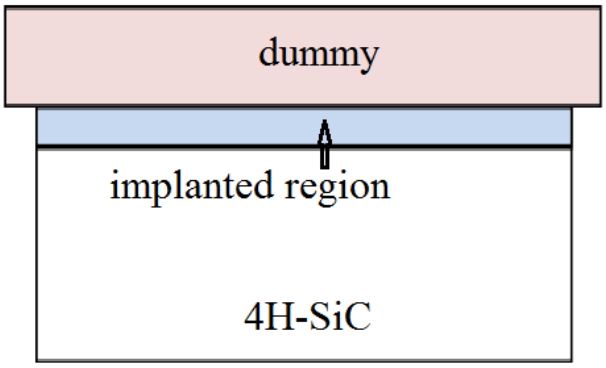

Figure 3.6: schematic representation of the microwave annealing process. The SiC dummy plays the role of heater for the implanted 4H-SiC.

The main difference between the two thermal treatments could be a possible interaction between the microwave field and the free carriers gradually increased in the implanted layer during the electrical activation process, which is expected to enhance the efficiency of electrical activation.

3.4 References of this chapter

[1] S. E. Saddow et al., “Advances in Silicon Carbide Processing and Applications, Semiconductor materials and devices series”, Artech house, inc. (2004)

[2] S. Soloviev et al., “Aluminum and Boron Diffusion into α-face SiC Substrates”, Material Science Forum, 389-393: 557-560 (2002)

[3] P. Achatz et al., “Doping-induced metal-insulator transition in aluminum-doped 4H silicon carbide”, Applied Physics Letters 92, 072103 (2008)

[4] J.M. Bluet et al., “Activation of aluminum implanted at high doses in 4H-SiC”, Journal of Applied Physics 88, issue 4 p. 1971-1977 (2000)

[5] Y. Negoro et al., “Electrical activation of high-concentration aluminum implanted in 4H-SiC”, Journal of Applied Physics 96, p. 4916-4922 (2004)

[6] S. A. Campbell, “The Science and Engineering of Microelectronic Fabrication Engineering”, Oxford University Press (1999)

[7] H. Ryssel et al., “Ion Implantation”, Wiley-Interscience publications (1986)

[8] J. K. Hirvonen, “Treatise on Materials Science and Technology – Ion Implantation”, vol. 18, Academic Press (1980)

[9] http://www.srim.org/

[10] M. V. Rao et al., "Al and B ion-implantations in 6H- and 3C-SiC", Journal of Applied Physics Vol 77, 2479 (1994)

[11] L. Muehlhoff et al., "Comparative electron spectroscopic studies of surface segregation on SiC(0001) and SiC(000-1)", Journal of Applied Physics, Vol. 60, 2842 (1986)

[12] R. Nipoti et al., "Carbon-cap for ohmic contacts on ion-implanted 4H-SiC", Electrochemical and Solid-State Letters **13** (12) (2010) H432-H435

[13] S. G. Sundaresan et al., "Ultrahigh-temperature microwave annealing of Al^+- and P^+-implanted 4H-SiC", Journal of Applied Physics 101, 073708 (2007)

More details on the aspects of this chapter can be found also in:

- J. W. Mayer et al., "Ion Implantation in Semiconductors", Academic Press (1970).
- T. Kimoto et al., "Fundamentals of Silicon Carbide Technology", Wiley (2014)
- J. F. Ziegler, "Ion Implantation: Science and Technology" Academic Press, 2nd Edition, 1988

4. Samples and investigation methods

4.1 van der Pauw devices

High purity semi-insulating 4H-SiC wafers have been implanted with Al^+ ions of multiple energies and doses to obtain box profiles at the wafer surface. Ion implantation was performed at a temperature in the range 300-400°C on Si-face 4H-SiC, after a deposition of a thick SiO_2 film. The role of this film is to slow down the ion energies so to obtain an almost flat implanted atom depth profile at the wafer surface. Implantation schedule and SiO_2 film thickness have been selected by the help of the SRIM2008 simulation tool. Two kinds of wafers were taken into account and compared: 8° miss-cut from the <0001> axis ones toward the axis of the (10-10) plane, and <0001> on-axis wafers. In both the cases, ion implantation was performed with tilt and twist angles such that ion beam enters the 4H-SiC crystal lattice along a direction at 8° from the <0001> 4H-SiC axis and within a plane that lays half a way between the (10-10) and (11-20) planes. Ion implantation provided a homogeneous Al concentration in the range 1×10^{19} - 5×10^{20} cm^{-3} across a thickness of about 400-600 nm.

The implanted wafers were diced into squares of 5 mm side adequate for a subsequent van der Pauw (vdP) device fabrication. These samples were then annealed either by

conventional method (CA) or through a microwave heating system (MWA) (see chapter 3.3): CA thermal treatment was performed at 1950°C for a time in the range 5-40 min, while MWA at a temperature of 2000°C for 30 s. Before the thermal treatments, the SiC native oxide was etched away in a hydrofluoric acid bath and samples were dried in nitrogen at 110°C for 30 min, and then the surface was protected by a carbon film (see previous chapter), obtained by a 900°C/2 min pyrolysis in forming gas of a 2-4 μm resist film (see ref. [1]). After CA or MWA, C-cap was removed by an 850°C/15 min dry oxidation. The root mean square surface roughness was measured on selected samples by Atomic Force Microscopy in the tapping mode and found to be in the range of about 0.5-5 nm. Figure 4.1 (see ref. [2]) shows typical SIMS profiles of the implanted samples: the thickness of the implanted layer was assumed equal to the length in depth that corresponds to half of the plateau height in the SIMS profile. Typical thickness values are of about 400 nm: this is an important

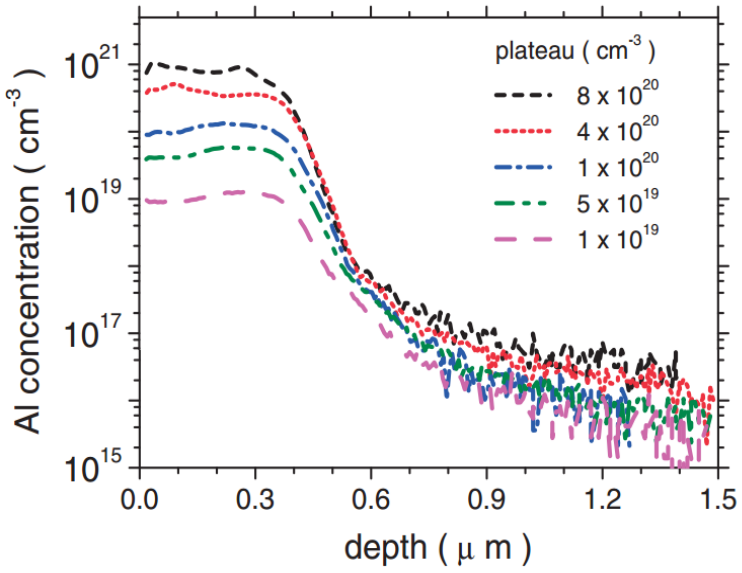

Figure 4.1: Secondary Ion Mass Spectroscopy (SIMS) Al depth profiles of the selected 4H-SiC specimens. Al plateau values are shown in the legend. See ref [2].

information for electrical investigation, because it allows to convert the Hall coefficient and sheet resistance measurements into carrier density and resistivity, respectively. In the investigated sample, the depletion layer at the surface is negligible due to the high doping level, whereas the uncertainty on the thickness value is related to the implant tail and the extended defects at the layer-substrate broad interface.

Square vdP devices were obtained by fabricating triangular ohmic contacts on the four corners of each 5 mm × 5 mm sample, after the annealing treatment and C-cap removal. For this purpose, sputtered Ti(80nm)/Al(2%Si, 350nm) films alloyed at 1000°C for 2 min in vacuum were used. The contact dimensions are not negligible if compared to the sample size, therefore a correction factor, dependent on the contact geometry, was applied to the results of the electrical measurements (see ref. [3]). In the samples of this study, such a correction resulted to an increase of the resistivity experimental data of a few percent (lower than 5%), while the correction to the Hall voltage was more significant, lowering the values of the Hall hole experimental data of about 10-30%

Four point vdP Hall and sheet resistance measurements were performed in the temperature range 30-680K, using different experimental apparatuses. These measurements were performed at CNR-IMM Institute of Bologna in the temperature range above RT, using a magnetic field of 1T. Measurements below RT were performed at the “Dipartimento di Fisica e Scienze della Terra” (DiFeST) of the “Università degli Studi di Parma": a 0.8 T magnetic field was applied in this temperature range. The Hall measurement apparatus consists in a scanner (Keithley®, model 705) a programmable current source (Keithley®, model 220) and a multimeter (Keithley®, model 196), with a maximum allowed voltage compliance of 8V. The temperature were stabilized by a LakeShore® 330 autotuning temperature controller.

The current range adopted for each measurement was chosen within the linear trait of the Current-Voltage characteristic of the contacts, checked before each measurement, in order to guarantee the ohmic behavior of the contacts, by excluding artefacts in the measured potentials due to space charge regions in proximity of them. Figure 4.2 shows the image of one of the investigated samples, visible inside the circle with the four triangular ohmic contacts at the corners.

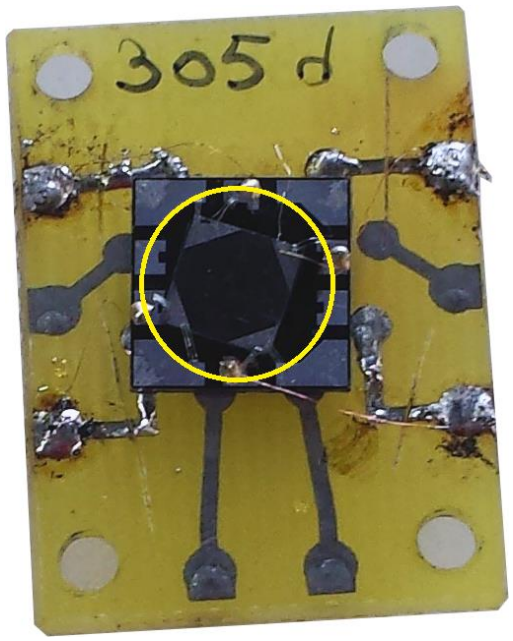

Figure 4.2: a picture of one of the investigated 4H-SiC vdP samples (inside the circle). Triangular Ti/Al ohmic contacts are visible at the four corners.

4.2 Al^+ implanted 4H-SiC p^+/n junction and Schottky barriers

Vertical p^+-i-n diodes were obtained by creating a p^+ layer by ion implantation of Al^+ on an epitaxial n-type layer of 4H-SiC. The epilayer, which showed a thickness of 8.48 μm and a doping level of 7×10^{15} cm^{-3}, was grown on a bulk n-type doped 4H-SiC substrate. Selective ion implantation at a temperature of 400°C was performed to obtain circular anodes with a diameter varying in the range 150-1000 μm: energies and doses of implantation were calculated to obtain an homogeneous doping profile in a layer of about 160 nm, with a plateau concentration of Al of 6×10^{19} cm^{-3}. In order to improve the reverse characteristic of the junction (increase of the BD voltage and reduction leakage current) an external ring implanted with Al in concentration of 6×10^{17} cm^{-3} was prepared around the anodes (see ref [4]). To electrically activate implanted ions, a CA treatment was performed, at a temperature of 1600°C for 30 minutes in an atmosphere of pure Ar, without protective C-cap. The final step was the realization of ohmic contacts in the anode and cathode region with the metallization of Ti/Al and Nickel, respectively. Nickel metallization was made on the backside of the structure, while Ti/Al contacts, concentric to the implanted circular regions but with diameters smaller of 40-50 μm, were evaporated on the p^+ layer. Ti/Al metallization was also carried out in non-implanted regions of the epilayer to realize Schottky barriers.

The p^+/n junctions and Schottky barriers were submitted to a preliminary electrical investigation by Current-Voltage (I-V) measurements to check their rectifying properties and C-V, AS and DLTS measurements to determine the doping profiles

and the physical parameters (mainly the activation energy) of the deep levels in the active region of the devices.

For the I-V characteristics, a Keithley 4912 electrometer was used, while C-V and AS measurements were performed using a HP 4192 LCR-meter. Admittance Spectroscopy measurements were carried out using two different experimental sets up to expand the temperature range explored: the first one was the same apparatus used the C-V measurements, working in the range 77-400K, the second one includes an HP 4284 LCR-meter fully interfaced and remotely controlled by a LabVIEW script and a cryostat working in the range 15-300K. DLTS measurements setup was an MDC Semitrap system based on a lock-in analysis of the transient capacitance. These studies have been performed in part at DiFeST, in part at the CNR-IMEM Institute (Istituto Materiali per Elettronica e Magnetismo), in collaboration with Dr. Enos Gombia.

4.3 Hall effect and resistivity measurements

The transport properties of a semiconductor, in presence of external fields and concentration gradients in the electron gas, can be studied in the semi-classic scheme of the Boltzmann equation, in the relaxation time approximation (RTA):

$$\frac{\partial f}{\partial t} + \frac{\partial f}{\partial \boldsymbol{r}} \cdot \boldsymbol{v} + \frac{\partial f}{\partial \boldsymbol{k}} \cdot \frac{\boldsymbol{F}}{\hbar} = -\frac{f - f_0}{\tau(\boldsymbol{k})} \tag{4.1}$$

where $\boldsymbol{k}$ is the electron wave vector, $\boldsymbol{v}$ is the group velocity, f_0 is the Fermi-Dirac function at thermal equilibrium, τ is the relaxation time, $\boldsymbol{r}$ is the position, t is the time and $\boldsymbol{F}$ is the resultant of the external forces. The function $f(\boldsymbol{r},\boldsymbol{k},t)$ is the statistical distribution function for the perturbed system: the quantity $f(\boldsymbol{r},\boldsymbol{k},t)\mathrm{d}\boldsymbol{r}\mathrm{d}\boldsymbol{k}/4\pi^3$ represent the number of occupied states at the time t in a volume $\mathrm{d}\boldsymbol{r}$ around $\boldsymbol{r}$ and $\mathrm{d}\boldsymbol{k}$ around $\boldsymbol{k}$ in the phase space. The Boltzmann equation describes the time-evolution of such a function in the phase space. In equation 4.1, the term to the right of the equality represents the collisional term, written in the RTA, which is valid for isotropic scattering mechanisms and for anisotropic but elastic ones. In presence of an external electric field $\boldsymbol{E}$ and a magnetic field $\boldsymbol{B}$ (both constant in time and spatially uniform), the macroscopic force is the Lorentz force, and $\boldsymbol{F} = -e(\boldsymbol{E} + \boldsymbol{v} \times \boldsymbol{B})$. In this case, for a spatially uniform electron gas, the Boltzmann equation 4.1 takes the form:

$$-\frac{e}{\hbar}\frac{\partial f}{\partial \boldsymbol{k}} \cdot (\boldsymbol{E} + \boldsymbol{v} \times \boldsymbol{B}) = -\frac{f - f_0}{\tau(\boldsymbol{k})} \tag{4.2}$$

In presence of weak electric fields (ohmic regime) this equation can be approximated to the form:

$$-e\frac{\partial f_0}{\partial \varepsilon}\boldsymbol{v} \cdot \boldsymbol{E} - \frac{e}{\hbar}\frac{\partial g}{\boldsymbol{k}} \cdot \boldsymbol{v} \times \boldsymbol{B} + \frac{g}{\tau(\boldsymbol{k})} = 0 \tag{4.3}$$

where $g=f-f_0$ represent the deviation from the equilibrium of the distribution function. In absence of magnetic field ($\boldsymbol{B}=0$) the solution is $g = e\tau(\boldsymbol{k})\frac{\partial f_0}{\partial \varepsilon}\ \boldsymbol{v} \cdot \boldsymbol{E}$ and it can be used to obtain the current density

$$\boldsymbol{J} = -\frac{e}{4\pi^3}\int_{BZ} g\ \boldsymbol{v}\ \boldsymbol{dk} = \sigma_0 \boldsymbol{E} \tag{4.4}$$

where σ_0 indicates the electrical conductivity in the absence of a magnetic field. The term $\tau(\boldsymbol{k})$ is called momentum relaxation time: in the RTA and for carriers in a single spherical valley, it results a function of the energy, $\tau(\varepsilon)$.

In presence of a magnetic field the solution can be found by writing the deviation from equilibrium of the distribution function as $g = e\tau(\varepsilon)\frac{\partial f_0}{\partial \varepsilon}\, \boldsymbol{v}\cdot\boldsymbol{A}$ (where **A** is a vector dependent both from **E** and **B,** (see ref [5]) and imposing that this form is the solution of equation 4.3. This imposition can lead to a simple solution when electrons occupy a single spherical valley, so that $m\boldsymbol{v} = \hbar\boldsymbol{k}$, where m is the scalar electron effective mass. Under the hypothesis of monokinetic carriers, so that the relaxation time results independent on the energy, it is possible to write:

$$\boldsymbol{E} = \frac{\boldsymbol{J}}{\sigma_0} - \frac{1}{en}\boldsymbol{B}\times\boldsymbol{J} \tag{4.5}$$

Equation 4.5 shows that, if the sample is crossed by a current density $\boldsymbol{J}$, the total electric field $\boldsymbol{E}$ appears as a sum of two components: the first one is the ohmic component (the only present in absence of magnetic field) $\boldsymbol{E}_\Omega = \boldsymbol{J}/\sigma_0$, with direction parallel to the current density vector, while the second one is the Hall component $\boldsymbol{E}_H = (-1/en)\boldsymbol{B}\times\boldsymbol{J}$, which has direction perpendicular to $\boldsymbol{J}$. The Hall effect consists in the appearance of this component in presence of a magnetic field. The experimental measurement of the Hall field allows the determination of the Hall coefficient

$$R_H = \frac{\boldsymbol{E}_H}{\boldsymbol{B}\times\boldsymbol{J}} \tag{4.6}$$

Analogous relations can be written for holes, so that, in the case of a monokinetic carrier gas

$$R_H = -\frac{1}{en} \quad \text{or} \quad R_H = \frac{1}{ep} \tag{4.7}$$

where n and p are the electron and hole density, respectively. The experimental determination of the Hall coefficient leads to the determination of both the sign and the density of carriers, and furthermore its combination with the electrical conductivity measurement allows the determination of the carrier mobility, $\sigma_0 = en\mu_e$ or $\sigma_0 = ep\mu_H$

Because such a simplified theory is valid for monokinetic carriers in a single spherical valley, in a real system, it can be applied only for metal or heavily doped semiconductors, with carrier density above the critical one for the insulator-to-metal transition (Mott transition). In fact, in this case, all the carriers involved in the transport process have energy approaching the Fermi energy, so that the relaxation time is equal to that correspondent to the Fermi energy. In the other cases, the relaxation time entering in the transport formulas has to be properly corrected to take into account the energy distribution of the carriers. A weighted average on the energy must be performed according to the following relation:

$$\langle \tau \rangle = \frac{2}{3} \frac{\int \tau(\varepsilon) \left(-\frac{\partial f_0}{\partial \varepsilon} \right) \varepsilon^{3/2} d\varepsilon}{\int f_0(\varepsilon) \varepsilon^{1/2} d\varepsilon} \tag{4.8}$$

It is possible to show that, in presence of a non-monokinetic electron gas the Hall coefficient can be rewritten as

$$R_H = -\frac{1}{en} \frac{\langle \tau^2 \rangle}{\langle \tau \rangle^2} = -\frac{1}{en} r_H \tag{4.9}$$

where $r_H = \langle\tau^2\rangle/\langle\tau\rangle^2$ is called Hall scattering factor. Its value is of the order of unity (usually its value is between 1 and 2) and depends on the temperature, owing to the variation with the temperature of the effectiveness of the different scattering mechanisms. The experimental value of the carrier density (and mobility) is usually affected by this indetermination, therefore the experimental data are called Hall carrier (mobility) density and symbolically identified by a pedex "H", to distinguish them from the *drift* (true) values:

$$n_H = \frac{1}{e|R_H|} = \frac{n}{r_H}$$

$$\mu_H = \sigma_0 R_H = \mu r_H \qquad (4.10)$$

Here n and μ are the true values.

From an experimental point of view, to perform Hall measurements are necessary two ohmic contacts for the injection of the current, two contacts to measure the Hall voltage perpendicularly to the current flux and a uniform magnetic field applied in the plane perpendicularly to both the Hall electric field and the current. In a bar shaped

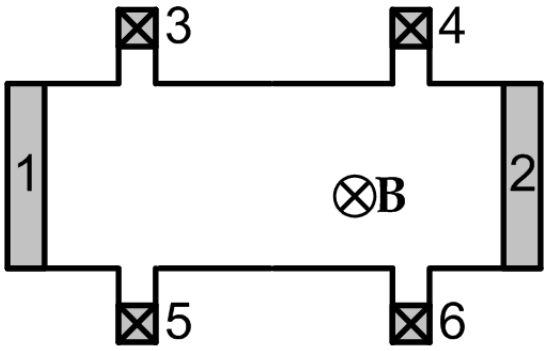

Figure 4.3: scheme of a Hall bar configuration. Current is injected between contacts 1 and 2 and the Hall field can be measured between contacts 3-5 or 4-6.

planar sample, this geometry can be realized by metallizing proper areas of the sample surface, as shown in figure 4.3. The magnetic field is applied perpendicularly the sample surface. This geometrical configuration is called "Hall bar method".

However, it is not always possible to obtain samples of this particular shape: in 1958, van der Pauw proposed an approach applicable to planar samples of arbitrary shape (see ref [6]). Over the years, this method became the most commonly used for electrical characterization, due its simplicity. Conditions required are i) uniform thickness, *d*, ii) homogeneity in the sample composition, iii) point-shape contacts on the sample edge and iv) a simply connected domain of the surface.

A sample in van der Pauw geometry is schematically reported in figure 4.4.

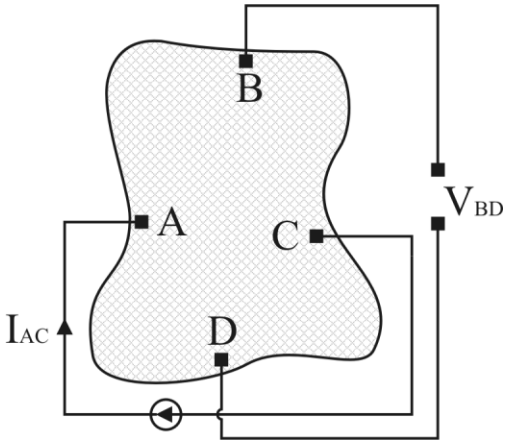

Figure 4.4: an arbitrary-shape sample according to van der Pauw method. A,B,C and D are the four ohmic contacts at the edge of the sample

Considering A, B, C, D the four contacts, denominated in consecutive order following the perimeter of the sample, as shown in the above figure, the resistivity ρ can be obtained from the measure of the resistance $R_{AB,CD}$ and $R_{BC,DA}$ defined as

$$R_{XY,WZ} = \frac{V_W - V_Z}{I_{XY}} \tag{4.11}$$

where (V_W-V_Z) is the potential difference between two contacts, W and Z, when the current I_{XY} is injected through the other two X and Y adjacent contacts. In the "resistivity configuration", the couple of current contacts XY, are adjacent and the same is true for the two voltage contacts (WZ). The arbitrariness of the geometry is taken into account by a correction factor $f(R_{AB,CD}/R_{BC,DA})$, known as "van der Pauw function":

$$\rho = \frac{\pi d}{\ln(2)} \frac{R_{AB,CD} + R_{BC,DA}}{2} f\left(\frac{R_{AB,CD}}{R_{BC,DA}}\right) \tag{4.12}$$

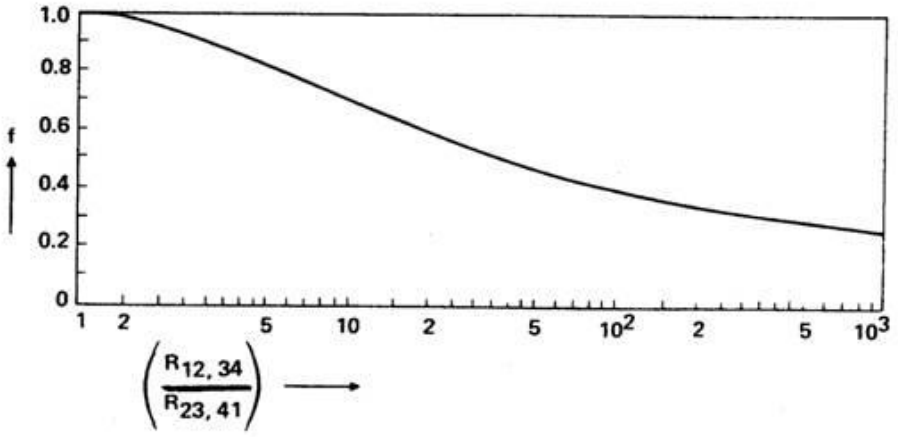

Figure 4.5: van der Pauw function values as a function of the ratio $R_{AB,CD}/R_{BC,DA}$.

Figure 4.5 shows the dependence of the van der Pauw function on the ratio $R_{AB,CD}/R_{BC,DA}$. Measurements in resistivity configuration can be performed both in absence and in presence of a magnetic field, giving the possibility to highlight magnetoresistance effects.

To prevent systematic errors, due, for example, to possible thermoelectric voltages, the measure is repeated by inverting the current sign, and by cycling over the four possible equivalent resistivity configurations (through a scanner). A mean of eight absolute values is calculated, to evaluate the experimental resistivity.

For the measure of the Hall mobility, instead, a different configuration must be used: the current is injected through a couple of opposite contacts and the Hall voltage measured at the other two opposite contacts: this is just the configuration illustrated by figure 4.4. In this case, the mobility can be obtained from the relation:

$$\mu_H = \frac{d}{B}\frac{\Delta R_{AC,BD}}{\rho} \tag{4.13}$$

where $\Delta R_{AC,BD} = R_{AC,DB}(B) - R_{AC,DB}(0)$ is the difference between the values of the resistance $R_{AC,DB}$ in presence and absence (B=0) of an external magnetic field. The resistance $R_{AC,DB}$ is defined with the same convention of equation 4.11. However, the final value of the mobility is obtained as a mean of the data given by equivalent configurations of measure, in which both $\Delta R_{AC,BD}$ and $\Delta R_{BD,AC}$ are derived.

It has been specified that the van der Pauw method requires ohmic contacts of negligible dimension with respect to the sample dimension. However, especially if the sample dimension is small, this condition can be not verified, introducing an error on both the experimental resistivity and Hall voltage data. Thanks to the work of Chwang et al. (see ref. [3]) these systematic error can be simply corrected in the case of triangular shaped contacts at the edges of square shape samples. Such correction factors are given as a function of the ratio between contact dimension and sample size (δ/l), as figure 4.6 shows. Note that the resistivity correction has been estimated also for square shaped ohmic contacts: triangular shaped contacts introduce lower error with respect the square shape ones.

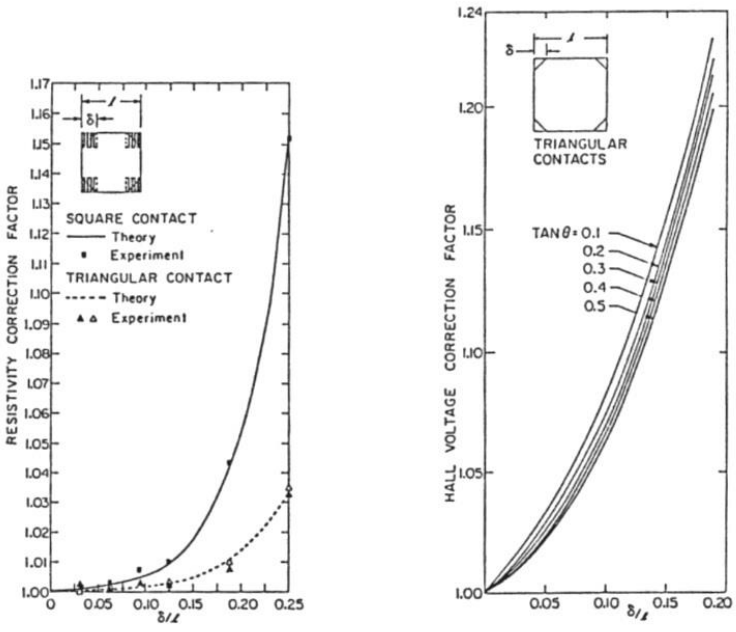

Figure 4.6: correction factors for resistivity (left) and Hall Voltage (right) for square or triangular ohmic contacts. See ref. [3].

An important information obtained by Hall measurements, which is one of the purposes of this work, is the estimation of the ratio between the acceptors and the implanted density of Al, giving the efficiency of the implanted-impurity electrical activation and the evaluation of the compensation ratio. This goal can be achieved by fitting the drift hole mobility and hole density data as a function of the temperature, after correction for the Hall factor. Taking into account the Boltzmann statistics and the neutrality equation (see ref. [7]), the total free hole density can be written as

$$p = \sum_i \frac{N_{Ai}}{1 + g_i exp[(E_{Ai} - E_F)/(K_B T)]} - N_D \qquad (4.14)$$

where N_{Ai} is the density of the ionized i-acceptor species, N_D is the density of compensating donors assumed fully ionized, g_i is the degeneracy factor and E_{Ai} is the ionization energy of the i-th acceptor impurity. Drift mobility can be calculated by

$$\mu = \frac{e\langle\tau(E)\rangle}{m_c} \qquad (4.15)$$

where m_c is the conductivity mass and $\tau(E)$ is the total momentum relaxation time, which can be obtained from the Mathiessen rule:

$$\frac{1}{\tau(E)} = \sum_n \frac{1}{\tau_n(E)} \qquad (4.16)$$

Here τ_n(E) indicates the momentum relaxation time of the n-th scattering mechanism taken into account in the calculation, like polar and non-polar optical phonon scattering, non-polar acoustic phonon scattering, and neutral and ionized impurity scattering. The analysis of the transport data of a p-type material is complicated by the parallel conduction of holes into the heavy and light-hole valence bands: this

phenomenon can be accounted for by coupling the two parallel conductions through the formula

$$\mu = \frac{p_1\mu_1 + \mu_2 p_2}{(p_1 + p_2)} \tag{4.17}$$

where p_i and μ_i, are, respectively, the true hole density and the drift mobility referred to each *i*-valley, with i = 1,2.

Another important point concerning the analysis of the transport data in p-type 4H-SiC, is related to their Hall to drift conversion, necessary before the fitting of the drift data, as mentioned above. Following the standard transport theory the calculation of the Hall factor in presence of mixed conduction effects is given by:

$$r_H = (p_1 + p_2)e\frac{\sigma_1\mu_1 r_1 + \sigma_2\mu_2 r_2}{(\sigma_1 + \sigma_2)^2} \tag{4.18}$$

where the meaning of the terms are the same defined above: σ_i, μ_i, p_i and r_i are, respectively, the conductivity, the drift mobility, the true hole density and the Hall scattering factor (intra-valley) referred to each *i*-valley, with i = 1, 2. However in p-type 4H-SiC, similarly to Silicon, such a formulas does not predict correctly the Hall factor, due to the warping of the VB. An experimental evaluation of the Hall factor, given by Schmid et al (see ref. [8]), is generally used for the Hall-to-drift correction for p-type 4H-SiC transport data, although such a temperature dependent curve resulted valid in a limited range of sample doping.

4.4 Space Charge Spectroscopy techniques

Space charge spectroscopy techniques are usually adopted for the characterization of deep levels in semiconductor materials. They are based on the analysis of the capacitance transient of a p/n junction or of a Schottky barrier, due to carrier emission or capture from deep levels inside the depletion layer. Amongst these techniques, in particular, Admittance Spectroscopy and Deep Level Transient Spectroscopy can be mentioned.

The admittance Y of a junction is defined as the ratio between the increment of current $\delta i(\omega)$ and the increment of the alternate bias signal $\delta v(\omega)$ of angular frequency $\omega=2\pi f$

$$Y(\omega) = \frac{\delta i(\omega)}{\delta v(\omega)} = G(\omega) + jS(\omega) \tag{4.19}$$

It could be expressed as the sum of a real part $G(\omega)$ (conductance) and an imaginary part $S(\omega) = \omega\, C(\omega)$ (S is the susceptance, C is the capacitance). It can be shown that the AS allows the determination of characteristic parameters of the deep levels (mainly the energy depth) by the analysis of the dependence of G and S on the frequency ω and the temperature. Taking into account figure 4.7, when a deep energy level E_t intercepts the Fermi level, the application of a sinusoidal signal modulates the depletion layer width and induces variations in the occupancy of the level, so that a variation of the space charge around $x = w$ and $x = \bar{x}$ occurs. If the amplitude of the signal is weak enough, only the occupancy of the traps next to $\bar{x}$ is modulated by the sinusoidal test signal, resulting in a contribution to the space charge variation. It is possible to demonstrate that in $\bar{x}$ the capture and emission time constants ($\tau_{c,e}$) are

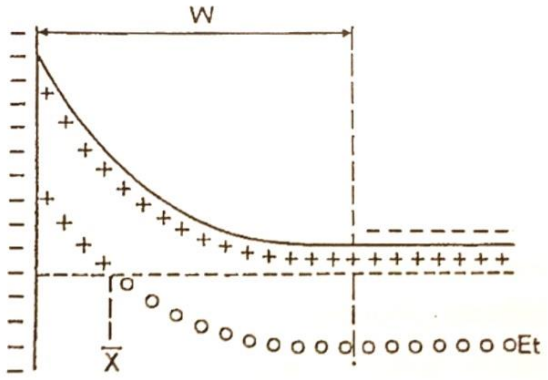

Figure 4.7: band diagram of a metal/n-semiconductor junction in presence of a deep level intercepting the Fermi Level in $\bar{x}$.

equal and $\tau_c = 1/2e_n$, where e_n is the thermic emission rate. If $\omega \leq e_n$, electrons are captured from traps during the positive semi-period and they are emitted during the negative one, while if $\omega \gg e_n$ the emission and capture processes can't follow the variation of the sinusoidal signal. It is possible to show that:

$$G(\omega) = \frac{(\omega/\bar{\omega})^2 (C_0 - C_\infty)\bar{\omega}}{1 + (\omega/\bar{\omega})^2}$$

$$C(\omega) = \frac{S(\omega)}{\omega} = C_\infty + \frac{(C_0 - C_\infty)}{1 + (\omega/\bar{\omega})^2} \qquad (4.20)$$

here C_0 is the low frequency capacitance that takes into account the charge and discharge contribution of the deep level, while C_∞ is the capacitance at high-frequency, when the deep level is not able to follow the variation of the sinusoidal signal. By referring the energy level E_t to the CB minimum, it results:

$$\bar{\omega} \approx 2e_n = 2N_C \langle v \rangle_n \sigma_n exp\left(-\frac{E_c - E_t}{K_B T}\right) \qquad (4.21)$$

Here N_c is the effective density of state of the CB, $<v>_n$ is the mean thermic velocity of electrons and (E_c-E_t) is the energy depth of the trap from the conduction band. It is possible to demonstrate that $G(\bar{\omega})$ shows a maximum when $\omega = \bar{\omega}$. Taking into account that $\bar{\omega}(T)$ has an exponential dependence on temperature, from an Arrhenius plot of $\bar{\omega}$ data obtained at different temperature it is possible to extrapolate the energy depth of the deep level.

AS, however, allow only the study of majority carrier traps with an energy depth usually lower than 0.5 eV. Deeper levels, or minority carrier traps can be investigated by DLTS. This technique consists on the study of the capacitance transient subsequent to a positive bias pulse applied to a p/n junction or a Schottky barrier. This transient varies exponentially with the inverse of emission rate e_n and

$$e_n = \langle v \rangle_n \sigma_n N_c exp\left(-\frac{\Delta E}{K_B T}\right) \tag{4.22}$$

The measurement of the emission rate of the transient of capacitance as a function of temperature allows the determination of the activation energy of the deep level. However, in this kind of measurement the capacitance signal is usually obscured by the noise of the diode. For this reason, the novelty introduced by DLTS is to make these transients periodic, and to process these signals with appropriate techniques (lock-in, double boxcar, etc…), by improving the signal to noise ratio.

4.5 Automation of measurements

The acquisition of the Admittance Spectroscopy data (but also Current-Voltage and others) was previously automated thanks to the development of specific software, mainly using LabVIEW® block diagrams, but also MATLAB® scripts.

LabVIEW (Laboratory Virtual Instrumentation Engineering Workbench) is a system-design platform and development environment provided by National Instruments®. It was first time released for Apple Macintosh in 1986, but now can be found also on different platforms including Microsoft Windows, Linux distributions and OS X. It is based on a visual programming language (or Graphical language, G), which is commonly used for data acquisition, instrument control and industrial automation. Its execution is determined by the structure of a graphical block diagram (a kind of source code of G language) on which different function-nodes are connected by wires. These virtual wires propagate the variables and any node can execute as soon as all its input data become available. This software includes the support for interfacing to a wide range of devices and instrument, mainly through USB, GPIB or Serial buses, interfaced to acquisition hardware (provided by National Instruments). A picture of one of the developed front panel and block diagram tools for Admittance Spectroscopy measurements is reported in figure 4.8. MATLAB (matrix laboratory), instead, is well known software inside the research community. It has a wide range of application including numerical computing, matrix manipulation, plotting of functions and data, and also data acquisition. Its first development was provided by Cleve Moler at the University of New Mexico in the late 1970s and then it was rewritten by MathWorks starting from 1984.

The main reason to use two different software is due to the fact that MATLAB allows an accurate analysis of acquired data inside the software itself, while LabVIEW is more user-friendly and, thanks to a proper user interface, allows the utilization of acquisition software also without any knowledge of this software.

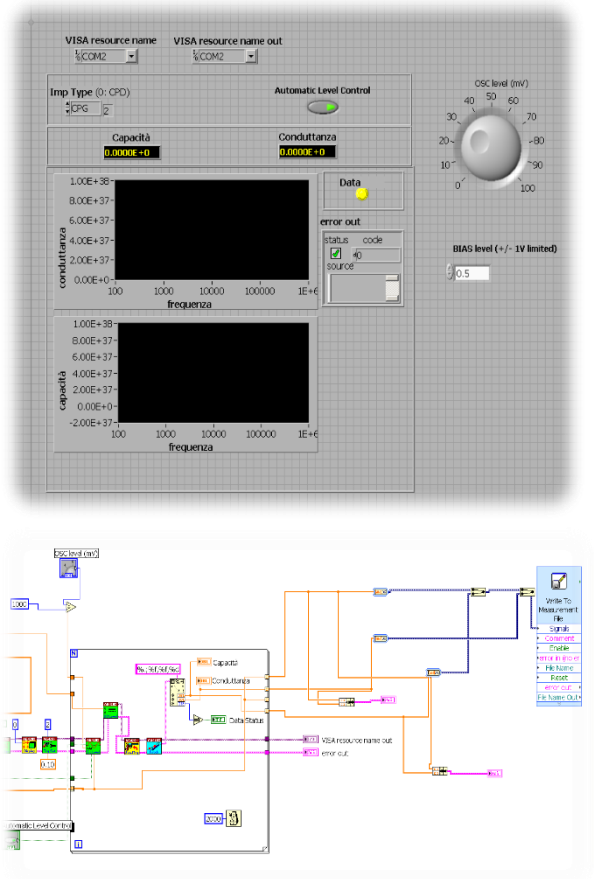

Figure 4.8: A picture of one of the developed front panel (up) and block diagram (down) tools for Admittance Spectroscopy measurements.

4.6 References of this chapter

[1] R. Nipoti et al., "Carbon-cap for ohmic contacts on ion-implanted 4H-SiC", Electrochemical and Solid-State Letters **13** (12) (2010) H432-H435

[2] R. Nipoti et al., "Microwave Annealing of Very High Dose Aluminum-Implanted 4H-SiC", Applied Physics Express 4, 111301 (2011)

[3] R. Chwang et al., "Contact size effects on the van der Pauw method for resistivity and Hall coefficient measurement", Solid State Electronics, vol. 17, issue 12, p. 1217-1227 (1974)

[4] B.J. Baliga, "Power Semiconductor Devices", PWS Publishing Company, 1996, ISBN 0-534-94098-6

[5] C. Ghezzi, "Fisica dei semiconduttori", Monte Università Parma Editore (2013)

[6] L. J. van der Pauw, "A method of measuring specific resistivity and Hall effect of discs of arbitrary form", Philips Research Reports 13, 1-9 (1958)

[7] A. Parisini et al., "Analysis of the hole transport through valence band states in heavy Al doped 4H-SiC", Journal of Applied Physics 114, 243703 (2013)

[8] F. Schmid et al., "Hall Scattering Factor for Electrons and Holes in SiC", Recent Major Advances, edited by W.J Choyke et al., Springer-Verlag, 2004) p. 517

More details on these aspects can be found in:

- C. Chien, “The Hall Effect and Its Applications”, Springer Science & Business Media (2013)
- S. M. Sze et al., “Physics of semiconductor devices” John Wiley & Sons (2006)
- E. Barsoukov et al., “Impedance Spectroscopy Theory, Experiment, and Applications”, John Wiley & Sons (2005)

5. Results

In this chapter, the results of the whole study performed in this work on the electrical properties of 4H-SiC ion implanted samples are described. It will be shown the comparison among transport data obtained in samples characterized by different concentrations of implanted Al ions, but also by different high temperature thermal treatments. The main goal of the research was the lowering of the resistivity of the material, with the aim to realize ohmic contacts of low specific resistivity. The approach that can be adopted to obtain lower and lower resistivity of the material can consist in the increase of either the ion implanted density and the temperature of the post implantation annealing treatment, or both. In this work, an effort has been made to enhance the electrical activation efficiency of the implanted impurities using very high annealing temperatures. For a given ion implanted density, in fact, the increase of the annealing temperature permits to activate a higher impurity density. In this way, a given free carrier density can be achieved in a sample by implanting a lower ion density with respect to the same material submitted to a low annealing temperature, with an expected improvement of the mobility values. Nevertheless, high annealing temperatures could favor the formation of traps centers, detrimental for the performances of devices. In this work, the experimental set up for the study of traps has been developed, with the aim to give a contribution, as more as possible, to the evaluation of both vantages and disadvantages of thermal treatments at very high temperatures in the realization of electronic devices.

Hall and resistivity characterization of heavily Al^+ implanted 4H-SiC vdP samples are discussed in next paragraphs. State of the art resistivity values are of the order of the

low 10^{-2} Ωcm decade (see for example ref. [1]). In the literature the implanted concentration and post implantation annealing temperature have reached the low 10^{21} cm^{-3} decade (see ref. [2]) and 1800°C (see ref. [3]), respectively. Resistivity values comparable with the state of the art have been reached in this work in samples with $3\text{-}5\times10^{20}$ cm^{-3} implant density, submitted to both microwave annealing at 2000°C and high temperature conventional annealing at 1950°C.

Another important parameter, other than the temperature, is the duration of the annealing treatments, and a specific study was conducted to find the optimal duration of the CA at such high temperatures. Furthermore, the effectiveness of ion implantation and high temperature conventional annealing, initially presented for off-axis samples, was checked subsequently also on on-axis samples, showing the results in paragraph 5.3. The Hall density and mobility trends, here reported, showed the typical characteristics of an impurity band conduction, giving the possibility of the study of such conduction mechanism and its presentation. These results are in paragraph 5.4.

In the last part of the chapter (paragraph 5.5) are finally reported the results of a preliminary investigation performed on p^+/n junctions, obtained by Al^+ implantation on an n-type epilayer, and Schottky barriers. The investigation was made by Space Charge Spectroscopy techniques, like Admittance Spectroscopy and Deep Level Transient Spectroscopy with the aim of checking the presence of electrically active defects, other than the dopants, induced by ion implantation.

5.1 Heavy Al^+ implantation on off-axis 4H-SiC: Annealing treatments comparison

5.1.1 – Introduction

Thermal treatments are a fundamental step for ion implantation doping of semiconductors, both to activate implanted ions and to recover the damaged crystal lattice. In this first part of the work, the effectiveness of the conventional annealing process (CA) performed at a temperature as high as 1950°C/5min on Al^+ implanted 4H-SiC is compared with a microwave annealing method (MWA) at 2000°C/30s, on the same samples. The details of both the methods are explained in chapter 3, while the preparation of the samples is described in chapter 4. Here, the results of the transport investigation on these samples are discussed.

5.1.2 Discussion of results

The vdP devices were characterized by resistivity and Hall effect measurements in the temperature range 30-680K. I recall that the transport measurements were performed

in two different experimental sets up. This approach is made necessary by the different methods that are used to heating and cooling the samples; however, it also permits to test the reproducibility of the electrical data around RT in different experimental systems, by permitting to sense/exclude possible systematic errors in the measurements. In the figures the "Hall hole density" is plotted, instead of the "drift hole density"; I recall the difficulty for obtaining the Hall factor for these samples mentioned in the paragraph 4.3, and again discussed below. In table 5.1 are resumed the characteristics of the samples discussed in this part of the work.

Sample name	Nominal Al density (cm^{-3})	Measured implanted density (cm^{-3})	Annealing treatment	RT hole density (cm^{-3})	RT resistivity (Ωcm)
SiC305g	1.5×10^{20}	$1.1\times10^{20**}$	MWA (2000°C/30s)	2×10^{19}	0.067
SiC305b	1.5×10^{20}	$1.1\times10^{20**}$	CA (1950°C/5min)	7×10^{18}	0.097
SiC293a	3×10^{20}	2.94×10^{20}	MWA (2000°C/30s)	5×10^{19}	0.059
SiC293e	3×10^{20}	2.94×10^{20}	CA (1950°C/5min)	3×10^{19}	0.052
SiC296c	5×10^{20}	5.34×10^{20}	MWA (2000°C/30s)	3.5×10^{20}	0.023
SiC296e	5×10^{20}	5.34×10^{20}	CA (1950°C/5min)	1.4×10^{20}	0.032

*Table 5.1: characteristics of the selected samples taken into account. The nominal Al density varies in the range 1.5-5×10^20 cm^-3; RT Hall hole density and resistivity of each sample are also resumed. ** For these samples the measured implanted density is slightly lower than expected, more details in the text.*

In figures 5.1(a) and 5.1(b) the Hall hole concentration and mobility are respectively shown for samples with the three different concentration of implanted Al impurities,

each one submitted either to thermal treatment using a conventional method (CA, closed symbols) at 1950°C for 5 min or by microwave annealing (MWA, open symbols) at 2000°C for 30s. The first observation, in the aim of this study, is the effect of different thermal treatments on couples of samples with same implantation density: in all the cases, MWA induces an higher Hall hole density and a lower Hall mobility with respect to CA treatment, but the trends have similar shape. The small differences observed in the three sets of data indicates that the coupling of the microwave field with the free carriers in the implanted layer, if it occurs, is weak, and suggests to ascribe these differences simply to the 50°C higher annealing temperature of MWA.

Focusing on the Hall carrier density Arrhenius plots relative to the two lowest doped samples, it is possible to see a linear trend starting from high temperature (lower values in the 1000/T scale) and going to RT and below, which agrees with an exponential decay of the carrier concentration in this temperature range. In the same temperature range the mobility increases. This behavior is typical of a hole freezing regime and a carrier transport trough the extended states of the valence band (see ref [4]). In particular, the slope of the hole density Arrhenius plots is compatible with a thermal activation energy of about 100 meV, a value lower than the activation energy of Al acceptors in low doped 4H-SiC (about 200 meV, see ref [5]), in agreement with the conclusion of ref. [6] and with the comments given at the end of paragraph 2.5.

The temperature dependence of the correspondent mobility curves of figure 5.1(b) shows a trend attributable to lattice scattering (dashed line shows a trend proportional

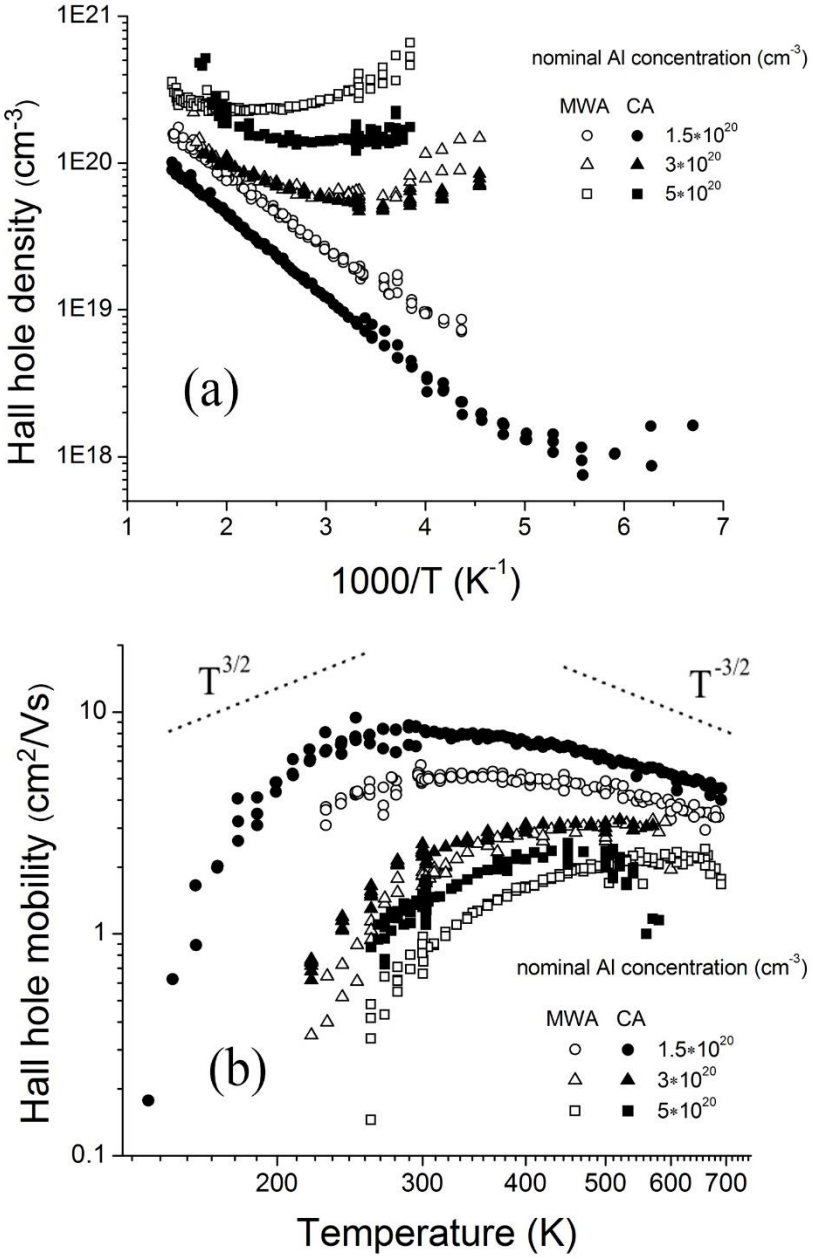

Figure 5.1: Hall hole density (a) and mobility (b) trends (see ref [4]) as a function of temperature of investigated 8° off-axis <0001> Al implanted samples. For each implanted density, the CA 1950°C/5min (full symbols) and MWA 2000°C/30s (open symbols) trends are showed. The experimental data were corrected for contact size systematic error.

to $T^{-3/2}$, typical of the interaction with acoustic phonons, for a comparison). These results confirm that the crystalline quality of these 4H-SiC implanted sample is preserved, despite the high Al concentration near the solubility limit.

By decreasing further the temperature, the Hall density Arrhenius plot presents a minimum (clearly visible especially in CA sample), while the correspondent mobility curve shows a decrease with decreasing T, steeper than the trend expected for the mobility limited by ionized impurity scattering, which, in presence of a classical gas of carriers, follows a power law of $T^{3/2}$ or weaker. This behavior is detectable also in samples implanted at 3×10^{20} and 5×10^{20} cm^{-3}, but with respective minima and maxima of Hall hole density and mobility shifted at higher temperatures: the more is the implanted dose, the more these features are shifted toward high temperature. Taking a closer look to the Hall carrier concentration of these highest implanted doses, it's possible to see how the density measured at the lower temperatures is similar with respect to the value measured at the higher temperatures, and the corresponding mobilities are quite low. However, by decreasing the temperature, for each sample, Hall density and mobility curves become progressively scattered and unreliable: this is due to the elevated carrier density, which correspond a low Hall voltage. As appears in the figures 5.1(a) and (b), the measured temperature range for the Hall data becomes narrower with increasing Al implantation doses. This effect is particularly evident in the heaviest doped samples. Differently, the electrical signals measured to evaluate the resistivity are not affected by this limitation, and the resistivity can be reliably measured up to very low temperatures, even if the current injected in the samples is progressively reduced, in order to guarantee ohmic behavior of the electrical contacts.

These aspects allow to hypothesize the low temperature onset of a carrier transport through an impurity band (IB) in all the investigated samples (see ref. [4]). Such a

mechanism appears to be relevant only at low temperatures in samples whose implantation density is lower than the solubility limit and seems to dominate the transport properties until RT and above in samples doped over such a limit. The onset of the IB conduction occurs below the temperature of the minima of the Hall hole density; however, in higher doped samples, where such minimum is less evident and broad, the IB conduction is expected to coexist with the transport through extended states at any temperature of Hall data measure, in a regime of parallel conduction (see ref. [4]).

From a technological point of view, the appearance of an IB conduction around RT in samples with implantation doses of 3×10^{20} and 5×10^{20} cm^{-3} represents a relevant feature: it opens the possibility to obtain Al implanted p-type 4H-SiC of almost constant hole concentration in a significantly wide range of working temperature for a device (see ref. [4]). IB conduction around RT has been already reported in literature (see ref. [7]) for implanted p-type 4H-SiC of Al implant density as high as 1.5×10^{21} cm^{-3} but submitted to the significantly lower post implantation annealing temperature of 1600°C. However, samples of this study show higher hole density and mobility, and then lower resistivity; these differences can be attributable to a more efficient electrical activation of the implanted dopants, due to the higher annealing temperatures. The importance of such a result is due to the achievement of an acceptor density high enough to induce an IB conduction persisting until RT, obtained through the implantation of a lower Al density with respect to ref. [7], which results in a higher mobility, probably thanks to a lower amount of lattice disorder.

The Al doping increasing of 4H-SiC samples, however, leads to lower carrier mobility with respect to analogous epitaxial materials reported by the literature [8]: a comparison is given in figure 5.2, where the RT Hall hole mobility is plotted as a

function of the RT Hall hole density for all samples in this work and for Al doped epitaxial 4H-SiC samples of ref. [8].

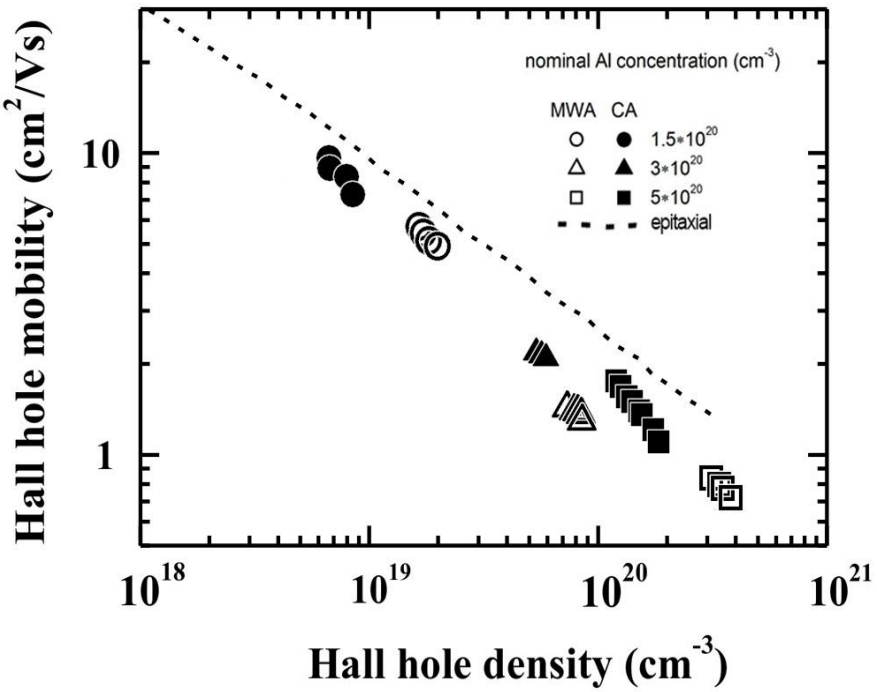

Figure 5.2: Hall hole mobility vs. Hall hole density at RT of samples of this work CA 1950°C/5min (full symbols) and MWA 2000°C/30s (open symbols), in comparison with Al doped epitaxial 4H-SiC of ref [8] (dashed line).

At comparable carrier densities, the mobility of implanted samples is systematically lower than epitaxial ones. This can be attributed to the presence of higher structural disorder caused by implantation technique. A relevant aspect of this comparison, in the light of the purposes of this work, is that the different post implantation annealing treatments give rise to p-type materials with almost the same dependence of the RT Hall mobility on the RT Hall density.

As mentioned in the paragraph 4.3, to estimate the efficiency of the impurity electrical activation reached thanks to the post-implantation annealing, the Hall carrier density and Hall mobility data must be converted into drift data to permit the fitting of the data through the transport theory. This could be done by introducing the Hall factor correction, r_H. As already explained, the usual Hall factor correction is performed by using an experimental curve, proposed by Schmid et al. (see ref. [9]), and assessed for an Al acceptor density in the range of 1.8×10^{15} cm^{-3} - 2×10^{18} cm^{-3}. In ref. [6], reasons have been given to justify the use of such an experimental Hall factor curve up to a concentration of about 1×10^{20} cm^{-3}. Moreover, ref. [6] clarifies that the usual formulas, which gives the expression for r_H in presence of two parallel conduction channels, i.e.:

$$r_H = (p_1 + p_2)e\frac{\sigma_1\mu_{1H} + \sigma_2\mu_{2H}}{(\sigma_1 + \sigma_2)^2} \tag{5.1}$$

can be reconciled with the experimental Hall factor of ref. [9] only by accounting for the anisotropy of the VB. As explained in paragraph 4.3, in equation 5.1, p_i, σ_i and μ_i are the Hall hole density, the conductivity and the Hall mobility of the i-th conduction channel (i=1 or 2, for heavy and light holes band) e is the electron charge. However, in each transport channel, Hall (μ_{iH}) and drift (μ_i) mobility are generally different, and their ratio is the *intra-valley* Hall factor (r_{Hi}). In ref [6], r_{Hi} is defined as the product of the Hall scattering factor $r_{Si} = \langle\tau_i^2\rangle/\langle\tau_i\rangle^2$, that takes into account the energy distribution of free non-monokinetic carriers, and a mass anisotropy factor r_{Ai}, that takes into account a possible anisotropy of the band and is, generally, dependent on temperature. Tn this way $r_{Hi} = r_{Si}r_{Ai}$ (see ref. [10]).

A similar approach, using the experimental Hall factor to correct the Hall data, has been adopted by other authors in the literature (see refs. [11], [12]) to describe the hole transport in 4H-SiC through the two parallel channels of the heavy and light hole

valence bands, although for relatively low doped samples. In ref. [6] it has been applied for samples having a concentration of acceptors in the range 2×10^{15} - 1×10^{20} cm^{-3}. However, for 3×10^{20} cm^{-3} and 5×10^{20} cm^{-3} implanted samples such an analysis cannot be performed, not only due to a doping level that overcomes the above given limit, but also because a transport through an impurity band is added in parallel in the whole temperature range. In this case, the application of equation 5.1 becomes difficult, in particular because the interpretation of the Hall coefficient as related to the inverse of the hole density becomes uncertain. In IB conduction regime, in fact, the Hall voltage can also change in the sign, with respect to that one consistent with the conductivity type of the sample (see, for example, ref. [13]). In this conduction regime, in fact, the hopping transport can be calculated in terms of a thermally activated hopping probability, and not in terms of an energy dependent relaxation time, in this way the Hall factor r_H may lose its usual meaning. Around the metal-insulator transition, however, the Hall coefficient does not have an abnormal sign, as suggested from Mott (see ref. [14]). Although a conversion of the Hall values into drift ones for the heaviest doped samples is not possible, some qualitative considerations can be performed.

To roughly evaluate the efficiency of the impurity electrical activation in the heaviest doped samples the following considerations can be proposed. The Hall hole density data of samples with Al concentration of 5×10^{20} cm^{-3} show a maximum Hall density value, at the highest temperatures, of about 3.5×10^{20} cm^{-3}, and the net acceptor density can be considered at least equal to this value. At these high temperatures, the conduction through extended states should prevail on the IB transport, so that the intra-valley factor of ref. [9] could be tentatively used to correct the Hall data. Taking into account a value of 0.6 for the high-temperature Hall factor r_H, a net acceptor density of about 2.2×10^{20} cm^{-3} is estimated for these samples. This density could indicate a 100% electrical activation with a compensation of about 50%, or an

electrical activation of more than 50% for a 15% compensation. The second hypothesis seems more reliable, if compared with the results of the analysis performed on 4H-SiC samples implanted with Al density in the range $5\times10^{19} - 1.5\times10^{20}$ cm^{-3} (see ref. [6]). In the latter case, in fact, an electrical activation of about 70% and a compensation of 10-13% has been obtained. This qualitative analysis indicates a comparable effectiveness of the two different thermal treatments, with a good activation ratio of at least 50% in the heaviest doped samples, and up to 70% for the lowest doped ones, with a similar compensation of 10-15%.

The Hall factor correction, however, doesn't affect sheet resistance measurements, and, in addition, this kind of measurements can be performed with good accuracy also at temperatures lower than those where Hall measurements are reliable. As observed above, in fact, the contacts preserve their ohmic behavior up to 10 K and, thanks to IB conduction, current can flow at any temperature. Figure 5.3 shows the Arrhenius plot of resistivity data for all the samples analyzed, in a restricted temperature range near RT, in absence of magnetic field (but no magneto-resistance was observed for these samples). All these samples show a thermally activated resistivity, with a minimum value at RT (dotted line) of 0.023 Ωcm, measured in the 5×10^{20} cm^{-3} Al implanted MWA sample. The resistivity versus temperature behavior show that, with sample cooling, the resistivity continuously increases for all these samples: also with the highest concentration of implanted Al, a semiconductor behavior persists. This behavior is not surprising in the light of other works reported by the literature, where a metal-insulator transition (MIT) has been observed in p-type vapor-liquid-solid epitaxial 4H-SiC with an Al concentration in the range $6.4\times10^{20} - 8.7\times10^{20}$ cm^{-3} [15]. However, because implanted materials have a higher crystal disorder with respect to epitaxial ones with identical dopant concentration, hopping conduction could persist in spite of high doping level and the MIT could be inhibited.

The comparison of each couple of samples with identical implantation conditions shows that the higher post implantation annealing temperature, provided by MWA at 2000°C with respect to CA at 1950°C, leads to a lower resistivity, attributed to a more efficient electrical activation, in agreement with literature reports (see ref. [16]). The

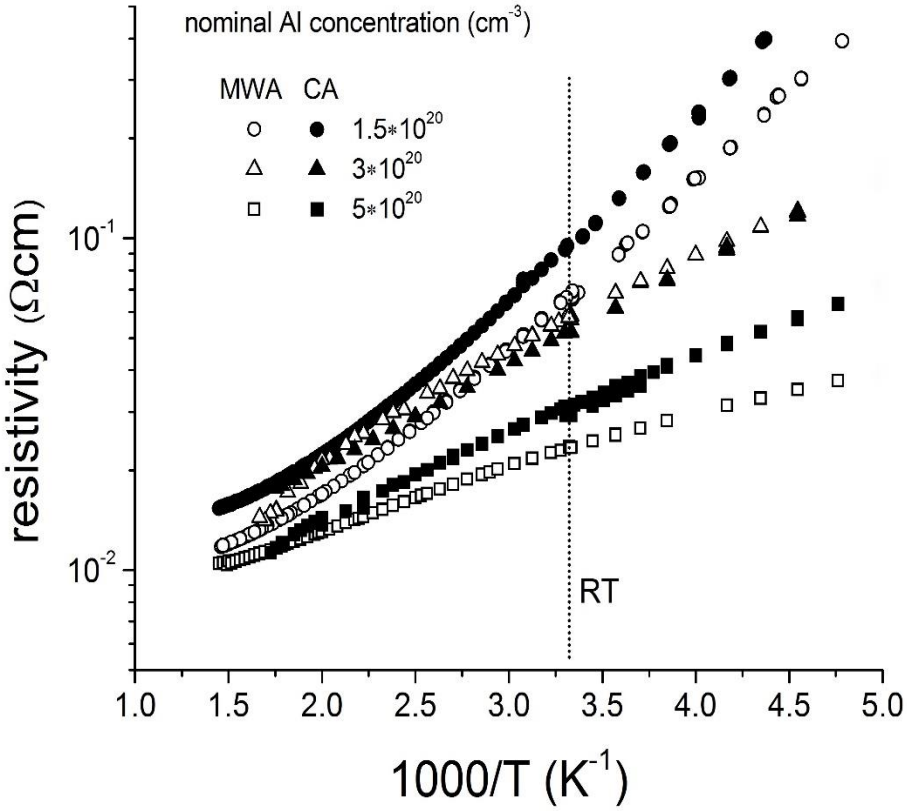

Figure 5.3: Arrhenius plot of the resistivity data for all the samples investigated, focusing around RT. Open and full symbols indicate samples annealed MWA and CA, respectively.

minimum RT resistivity value of 0.023 Ωcm and the trends here reported are in agreement with the conclusions of ref. [17], where a minimum resistivity value of 0.07

Ωcm with Al concentration of 5×10^{20} cm^{-3} has been computed for a hole transport through the extended states, in absence of compensation, and lower resistivity values only thanks to a transport through impurity band has been predicted.

The transition from a transport through extended states to an IB conduction is evident in figure 5.4, where the Arrhenius plot of the resistivity data of all samples is shown in the whole temperature range. The trends of samples with the lower Al implanted concentration of 1.5×10^{20} cm^{-3} (upper curves) show a bending towards a lower slope with the ample cooling, and this slope is kept until low temperatures.

The pioneering model in the literature on this topic has been proposed by Miller and Abrahams (see ref. [18]). In this model, the conductivity is taken as the sum of three thermally activated contributions:

$$\sigma(T) = \sigma_1 + \sigma_2 + \sigma_3 = \sigma_{01} e^{-\varepsilon_1/K_B T} + \sigma_{02} e^{-\varepsilon_2/K_B T} + \sigma_{03} e^{-\varepsilon_3/K_B T} \qquad (5.2)$$

with three terms corresponding, respectively, to the thermal activation of the carriers from impurity states to the extended states band (ε_1), to the higher Hubbard band (ε_2), and the thermal activation of hopping from an occupied impurity state to a nearest-neighbor empty one (ε_3). K_B is the Boltzmann constant. Consistently with such a model, an almost linear trend in the Arrhenius plot of the low temperature resistivity, then, is usually attributed to nearest neighbor hopping conduction; ε_3 is then the activation energy for the hops between nearest impurities, which varies with compensation and doping level (see ref. [19]). The activation energy estimated from the low temperature slope of the Arrhenius plot for the data of figure 5.4 is of about 20 meV. Considering again both the lowest doped samples here discussed, the slope around RT corresponds, instead, to an activation energy of about 100 meV. Such an energy can be attributed, in agreement with the Miller and Abrahams model, to the

transport through the valence band extended states. Effectively its value is comparable to the slope of the Hall density Arrhenius plot (see previous discussion on figure 5.1(a)), and then resulted to be related to the thermal ionization energy of the majority dopants.

A departure from the expectation of the Miller and Abrahms model, however, is observed in the heaviest doped samples: these aspects will be discussed in chapter 5.4.

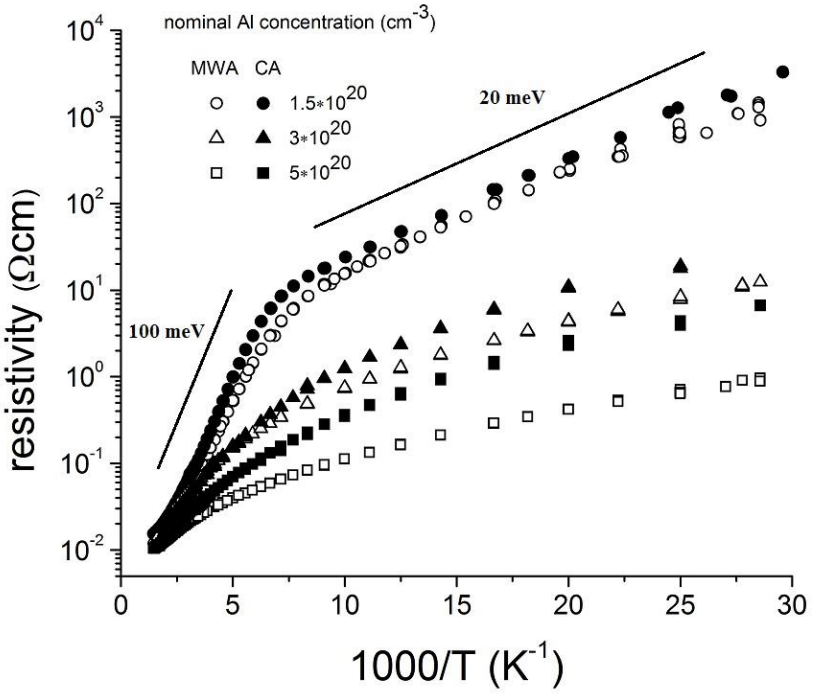

Figure 5.4: Arrhenius plot of the resistivity data for all samples presented in the whole temperature range. Open and full symbols indicate samples annealed MWA and CA, respectively.

5.2 Heavy Al^+ implantation on off-axis 4H-SiC: estimation of the optimal duration of the conventional annealing

5.2.1 Introduction

In the previous part of the work, the effectiveness of two different annealing techniques was discussed: a conventional, radiofrequency heating furnace up to 1950°C and a microwave technique up to 2000°C. In particular, it was shown that with CA at 1950°C/5min it is possible to obtain results similar to those induced by MWA, and the little differences reported are mostly attributable to the 50°C higher temperature of the latter. However, there is another parameter that needs to be optimized, other than the temperature: the duration of thermal treatment. Studies on the effect of the annealing time are reported in literature, but referred to samples submitted to thermal treatments at lower temperature of 1800°C [3,20] and having Al concentration not always declared. In particular, in ref. [3], with an implanted Al concentration of 3×10^{21} cm^{-3} and annealing time in the range 1-200 min, it was shown an increasing sheet resistance and a decreasing free hole density with the increasing duration of annealing.

In this work, the study is focused on the influence of the annealing time on 1.1×10^{20} cm^{-3} Al^{+} implanted 4H-SiC samples, subjected to conventional thermal treatments with a constant temperature of 1950°C. Like in previous part, semi-insulating 8° off-axis <0001> 4H-SiC wafer has been implanted at 400°C with Al^{+} ions. Before the annealing, the implanted wafer was submitted to SIMS investigation. Wafer has been subsequently cut into 5×5 mm^2 samples, each of which was submitted to an identical thermal treatment, except for the duration. As usual (see chapter 4.1), before the annealing, a surface-protecting carbon film were deposited on the samples to prevent surface decomposition and to limit the surface roughness. For all the pieces, the thermal treatment was performed at 1950°C, in a high purity Ar atmosphere of a inductively heated crucible, with annealing times varying in the range 5-40 min, and by keeping a constant heating rate of 40°C/s and an exponential cooling cycle with 30s characteristic time. Then the samples were prepared for electrical investigation (see chapter 4.1).

5.2.2 Discussion of results

SIMS analysis reported on figure 5.5 is relative to the 1950°C/5min annealed sample (profile before annealing results identical). An Al plateau of about 1.1×10^{20} cm^{-3} next to the sample surface is clearly visible, extended up to 1300 nm in depth, a height lower and a width larger than the expected ones of about 1.5×10^{20} cm^{-3} and 500 nm, respectively. Moreover, there is an unexpected weak dip in the Al profile, at about

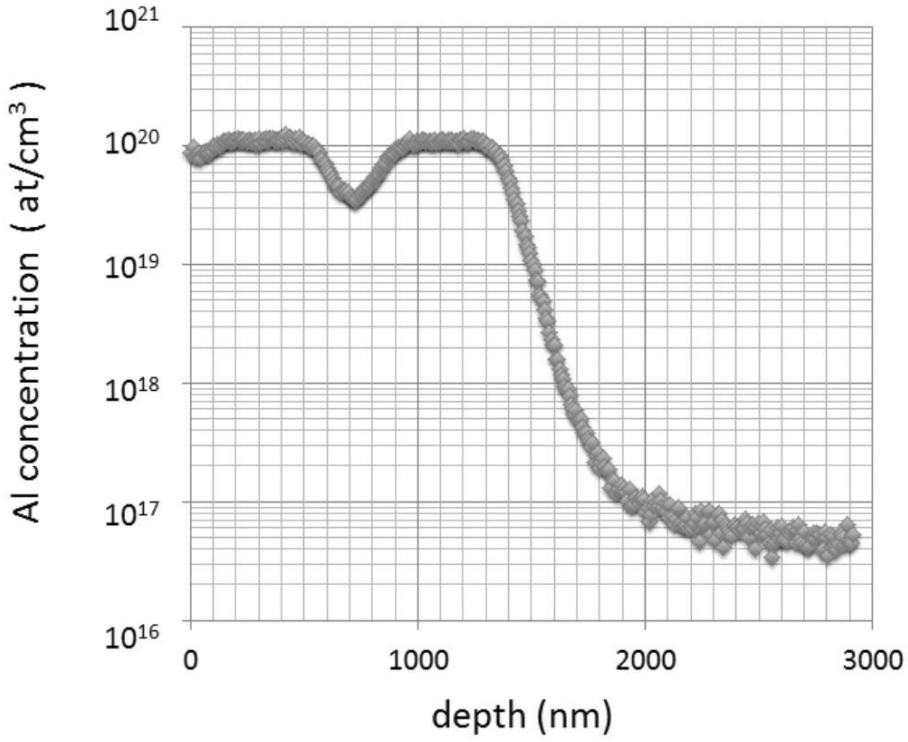

Figure 5.5: SIMS Al depth profile of the 1950°C/5min annealed sample.

700 nm depth. This anomalous profile, significantly different from those reported in chapter 5.3, is due to a wrong step in the sample processing before the ion implantation. Its presence complicates a quantitative analysis of the electrical data, but, considering that the implantation conditions are identical for all samples, a comparison among their sheet resistance and Hall coefficient are expected to be still reliable in establishing the duration of the more efficient thermal treatment (see ref. [21]).

Sheet resistance Arrhenius plots of all the samples of this series are reported in figure 5.6: in figure 5.6(a) they are shown in the whole temperature range investigated, while

in figure 5.6(b) their high temperature data are expanded, to appreciate differences around RT. Trends correspond to four different annealing times of 5, 10, 25, 40 minutes. The shape of these curves are very similar, with two distinct linear regions of different slope at high and low temperatures respectively, separated by a transition region, around 125K (8 in 1000/T K^{-1} scale). At high temperatures, the curve shape is consistent with a thermally activated exponential dependence on temperature of the sheet resistance, and with an activation energy varying from about 114 meV for the 5min annealed curve (dotted line on figure 5.6(b)) to about 104 meV (dashed line) for the 40min one. At low temperatures, instead, the linear trends of the Arrhenius plots again suggest an exponential trend of the sheet resistance with temperature, compatible with an activation energy of about 20 meV for all curves. Similarly to previous data, these two distinct regimes can be attributed to the presence of two different channels of carrier transport: one through the extended states, dominant at higher temperatures, and the other one, through the impurity sites, clearly visible at lower temperatures. Again, the activation energy for the conduction through extended states, here reported, is of the same order of magnitude, but of lower absolute value, than the thermal ionization energy of diluted Al in 4H-SiC [5]. The reason of this behavior has been clarified in chapter 2.5.

Taking into account that in a compensated semiconductor:

- the effective dopant ionization energy decreases with increasing of both doping and compensation level
- the absolute value of the resistivity decreases with increasing doping level and/or with decreasing of the compensation ratio
- in figure 5.6(b) is clearly visible a decrease of both resistivity and activation energy with increasing annealing time

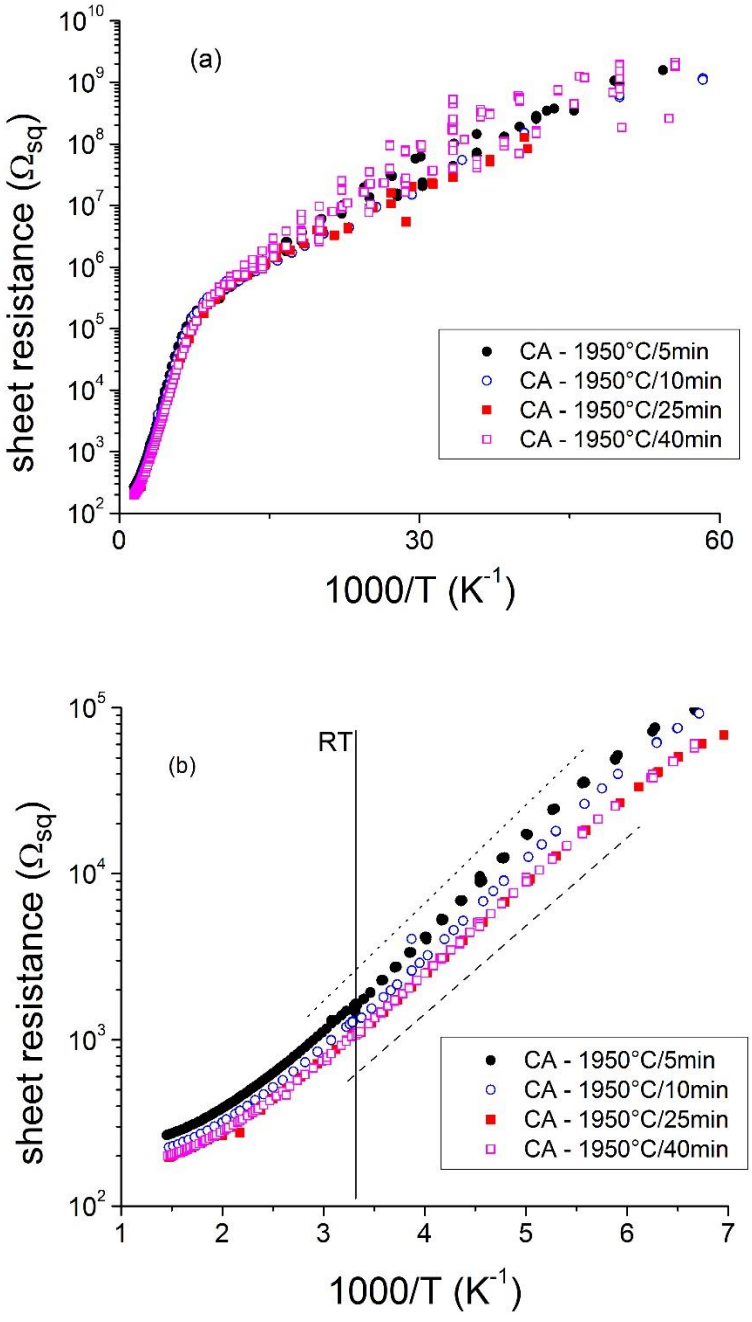

Figure 5.6: Sheet resistance as a function of temperature of the 1.1×10^{20} cm^{-3} *Al implanted samples of the study, annealed at fixed temperature of 1950°C for a time varying between 5 and 40 minutes. Reported in the whole temperature range of measurement (a) and focusing on high temperatures (b). Dotted and dashed lines show the exponential trends of the 5 min (about 114 meV activation energy) and 40 min curves (about 104 meV) respectively.*

it is possible to hypothesize that the increasing of the annealing time leads to a better electrical activation on Al^+ implanted 4H-SiC at such doping level. In addition, the Arrhenius plots reported in figure 5.6(b) clearly show that longer thermal treatment duration in the range 5 to 25 min leads to a sheet resistance reduction in all temperature range; trends corresponding to 25 and 40 min long annealing treatments, instead, are almost overlapped, indicating a saturation of the annealing effectiveness for a time exceeding 25 min (see ref. [21]).

In figure 5.7, the RT values of the sheet resistance are plotted as a function of the 1950°C/CA duration. Starting from a value of about $1650\Omega_{sq}$ for a 5min thermal treatment, sheet resistance decrease to about $1270\Omega_{sq}$ for 10min annealing process and then saturate to a value close to $1100\Omega_{sq}$ at 25 and 40 min. The two dashed lines are representative of the decreasing sheet resistance region and the saturation one. The

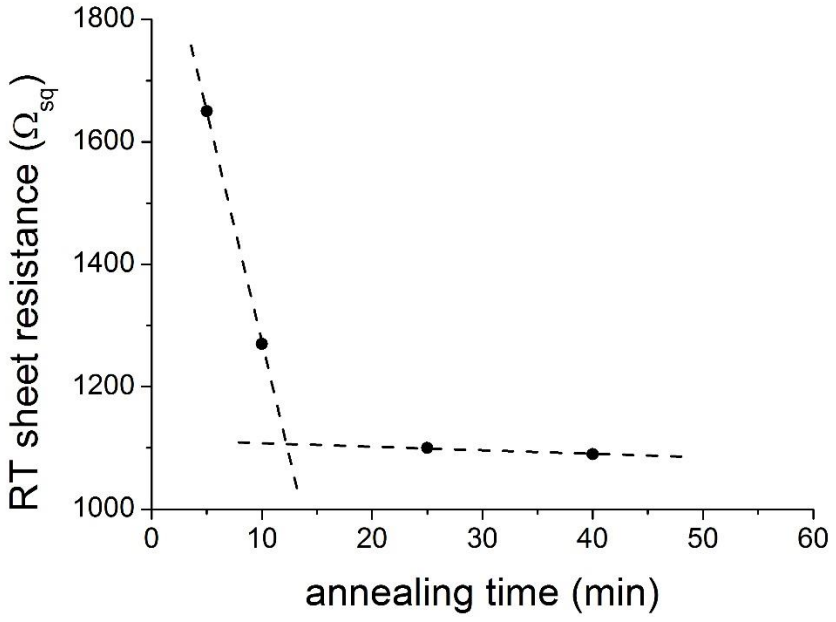

Figure 5.7: RT sheet resistance of samples investigated for the different duration of 1950°C conventional annealing.

intersection should qualitatively indicate the minimum annealing time required to obtain the lowest sheet resistance value in the case of a 1.1×10^{20} cm^{-3} Al^{+} implanted 4H-SiC samples, annealed by conventional method at a temperature as high as 1950°C: this time should be about 12-13min.

These trends are completely different from those reported in ref. [3], probably due to a different implanted density (1.1×10^{20} cm^{-3} in this work against 3×10^{21} cm^{-3} in the other one) and/or the different annealing temperature (1950°C in this case, against 1800°C in the other one). Further investigation is necessary to clarify the differences.

5.3 Heavy Al^+ implantation on on-axis 4H-SiC

5.3.1 Introduction

The importance of on-axis 4H-SiC substrates investigation is mainly related to the fact that in on-axis 4H-SiC devices the formation of stacking faults (SF) in the basal plane is expected to be reduced in respect to off-axis samples. Such extended defects are retained responsible of the "forward voltage drift" effect in the high power bipolar electronic devices: due to an expansion of SFs during forward-bias operation, the voltage required to turn the device in the on-state increases continuously. Therefore, the turn-on voltage is a not stable parameter of the device and make the latter useless. Mesa p-i-n diodes fabricated on epitaxial p^+-p-n-n^+ on-axis 4H-SiC wafers (see ref. [22]) have not shown appreciable evidence of this effect, as like as the formation of stacking faults (from optical characterization). Works reported in the literature (see ref. [23], [24]) highlighted the realization of 10 KV p-i-n diodes on epitaxial on-axis 4H-SiC layers of good performances.

5.3.2 Discussion of results

A commercial semi-insulating, <10 cm^{-2} micro-pipe density, on-axis <0001> 4H-SiC wafer have been submitted to Al^{+} implantation at 400°C (see chapter 4). The absence of channelling (see chapter 3) and the flatness of profiles was confirmed by SIMS spectra (see fig. 5.8), which show the Al depth profiles of the three samples selected for this discussion, with an almost flat plateau of 4.8×10^{18} cm^{-3}, 9.2×10^{18} cm^{-3} and 4.7×10^{19} cm^{-3} density, respectively, and a thickness of about 630 nm. van der Pauw devices were prepared to obtain sheet resistance and Hall measurements in the temperature range 100-580 K, again with two different experimental sets up for investigation above RT and below RT as in the case of the off-axis samples. The electrical data resulted reproducible within an error of about 10-20%, and will be discussed in the following. The conversion of the Hall data into drift ones has been performed using the hole Hall factor for Al doped 4H-SiC of ref. [9], as discussed in ref. [6]. In table 5.2 are resumed the main aspects of the on-axis samples here investigated.

AFM measurements in the tapping mode were adopted for the characterization of the surface morphology and its root mean square (rms) roughness resulted in the range 0.5-0.7 nm, comparable for all the samples despite the different Al implanted density. Such a roughness value is even lower than the virgin SiC wafer and lower than that one reported for off-axis 4H-SiC samples (see ref. [24]).

The results of the electrical investigation on these samples is reported in figures 5.9 and 5.10: these figures show the temperature dependence of the drift hole density, the

drift hole mobility and the resistivity of three on-axis samples (see ref. [26]). For comparison, the same figures also show the data of two off-axis samples, whose Al implant concentration is comparable to the two higher doped on-axis samples here discussed. In particular, the data of the off-axis samples with 1×10^{19} and 5×10^{19} cm^{-3} Al implant concentration (empty symbols) are compared to those of the on-axis samples with 9.2×10^{18} and 4.7×10^{19} cm^{-3} Al implant concentration (full symbols), respectively.

This comparison highlights a higher hole density and a lower resistivity of the on-axis samples with Al concentration of 9.2×10^{18} and 4.7×10^{19} cm^{-3}, with respect of their corresponding off-axis counterparts with similar Al concentration. Looking at their mobility trends, instead, the on-/off-axis couple of samples of lowest Al implanted concentration exhibits a higher mobility for on-axis sample, while the couple of samples of higher Al implanted density shows an almost equal / slightly lower mobility for the on-axis sample in respect to the other one. I will come back to this comparison below. Before to comment the mentioned differences between on/off-axis samples and to suggest a qualitative explanation for them, it is worth to briefly comment the shape of the curves of figures 5.9 and 5.10. These trends are qualitatively similar to those reported in the previous part of the thesis (chapter 5.1) for off-axis 4H-SiC samples with an Al implanted concentration of about 1×10^{20} cm^{-3}. In particular, also these samples show a thermally activated transport through the extended states of the valence band at higher temperatures, while the trends at lower temperature suggest a thermally activated hopping conduction into an impurity band; the transport can be described by the Miller and Abrahams model (see ref. [18]) through the equation (5.2). These two transport regimes are evident in both carrier density and mobility trends: in the first case, a minimum in the Arrhenius plot of the hole concentration is visible, in particular in the two highest density samples.

Sample name	On/off axis	Measured implanted density (cm^{-3})	Annealing treatment	RT hole density (cm^{-3})	rms roughness (nm)
SiC314a1	On-axis	4.79×10^{18}	CA (1950°C/5min)	2.5×10^{17}	0.55±0.09
SiC314b1	On-axis	9.24×10^{18}	CA (1950°C/5min)	4.4×10^{17}	0.55±0.17
SiC314c1	On-axis	4.66×10^{19}	CA (1950°C/5min)	2.6×10^{18}	0.68±0.13
SiC284e	Off-axis	1.07×10^{19}	CA (1950°C/5min)	3.5×10^{17}	-

Table 5.2: characteristics of the selected samples taken into account for the study of on-axis Al^+ implanted 4H-SiC. The implanted density varies in the range of about 5×10^{18} to 5×10^{19} cm^{-3}, and also off-axis samples of similar density are taken into account for comparison. The CA treatment is the same for all samples

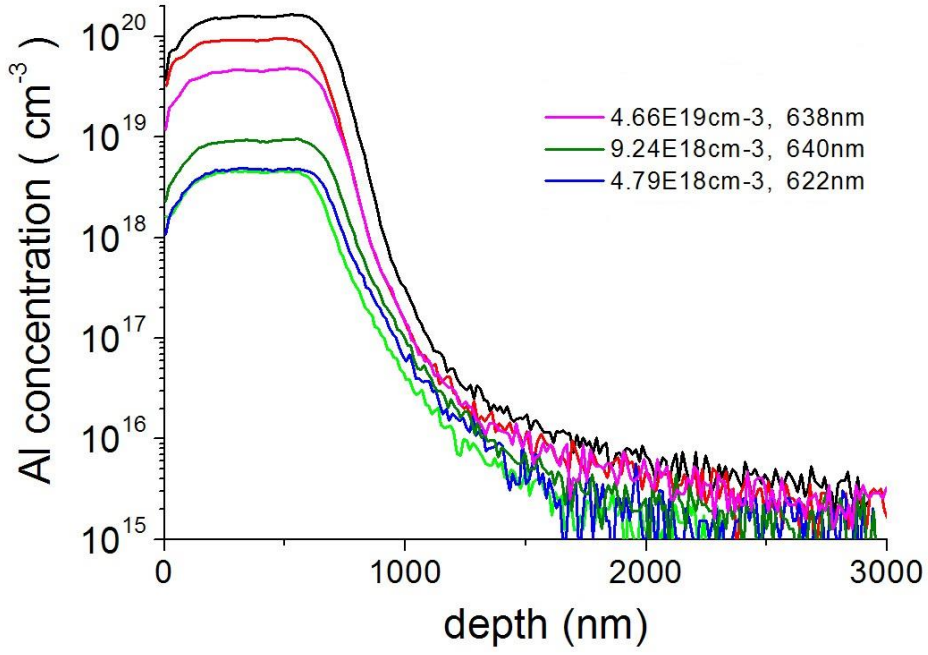

Figure 5.8: Secondary Ion Mass Spectroscopy (SIMS) measurements of the samples investigated (plus other samples, here not discussed, for comparison). The Al depth profiles show a similar plateau thickness of about 630 nm.

Concerning the mobility data, at high temperatures the trends of both the curves are qualitatively compatible with that expected for a mobility limited by the scattering with phonons, under the hypothesis of a classical free hole transport into VB (as for example: a $T^{-3/2}$ like temperature dependence). At lower temperatures the drop of mobility trends, significantly steeper than expected one for a mobility limited by ionized impurity scattering mechanism ($T^{3/2}$ like temperature dependence in the case of acoustic phonon scattering via deformation potential), suggests the onset of a transport through localized states. The minimum on the hole density Arrhenius plots of figure 5.9(a), as seen in previous part of the chapter, is typical of the transition between the two conduction regimes and appears more or less at the same temperature of the drop of the mobility curve. Moreover, it shifts toward higher temperatures with the increasing of acceptor concentration (then, of the electrically activated Al impurities), indicating a shift at higher temperature also of the onset of the IB conduction with increasing doping level. The hints of a conduction through impurity band can be found also in resistivity trends, that show a reduction of the slope with sample cooling, according to the Miller and Abrahams model. Comparing the on-axis and off-axis trends of the couples of samples with similar Al density, instead, it seems that the minimum of the hole density appears at slightly higher temperatures in the on-axis samples with respect to the off-axis ones (see ref [26]). This fact, and the lower resistivity of on-axis samples with respect their off-axis counterparts, are consistent with the supposition of a little higher acceptor density and/or little lower compensation in the on-axis 4H-SiC with respect to the 8° off-axis ones. The reason of these differences could be due to a different typology of defects induced during the implantation process. These on-axis and off-axis 4H-SiC semi-insulating wafers come from different suppliers and so they might have a different defect content for obtaining the semi-insulating property, and such differences could influence the electrical

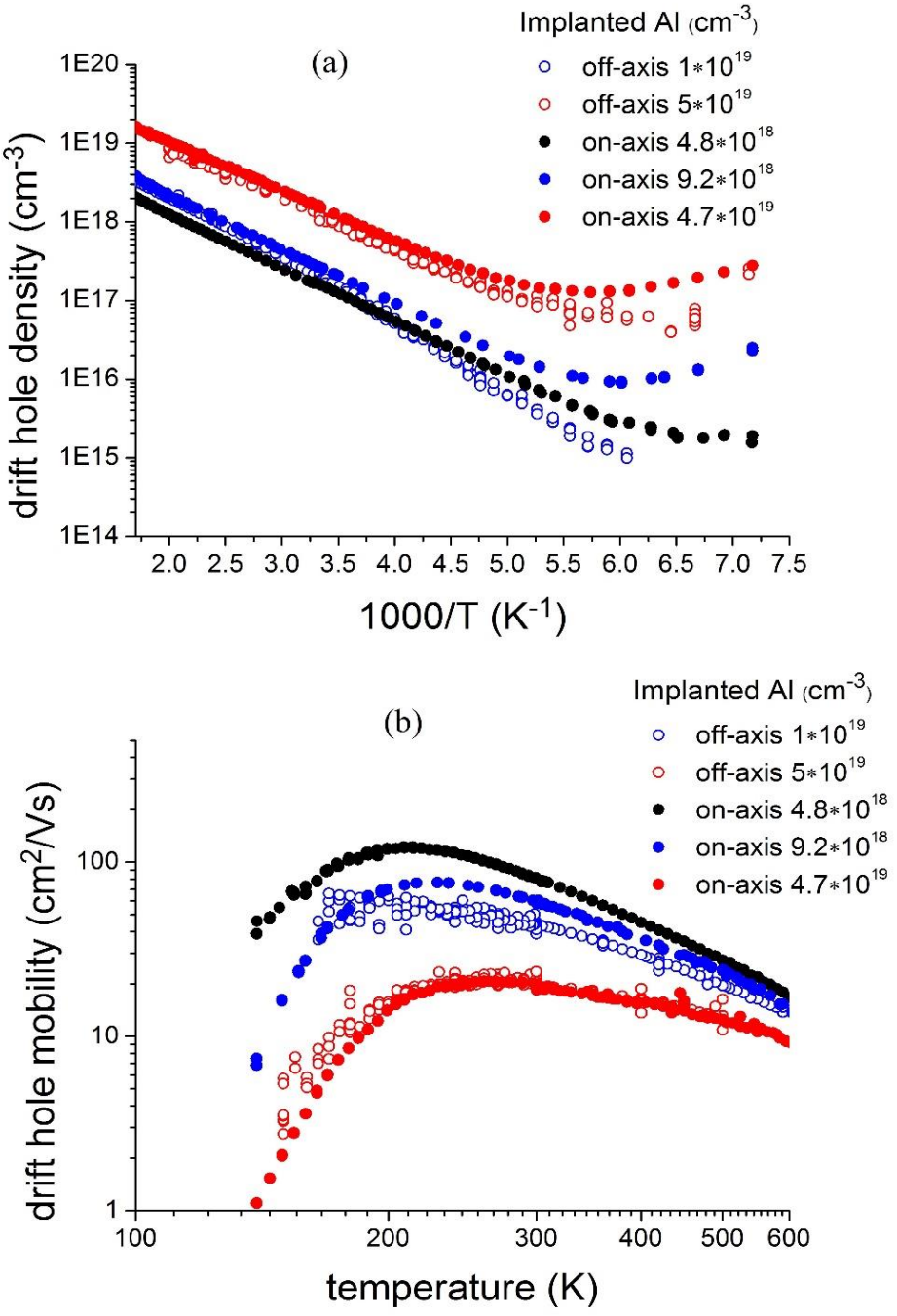

Figure 5.9: Drift hole density (a) and mobility (b) as a function of temperature of Al^+ implanted on-axis and off-axis semi-insulating 4H-SiC, 1950°C/5min conventional annealed.

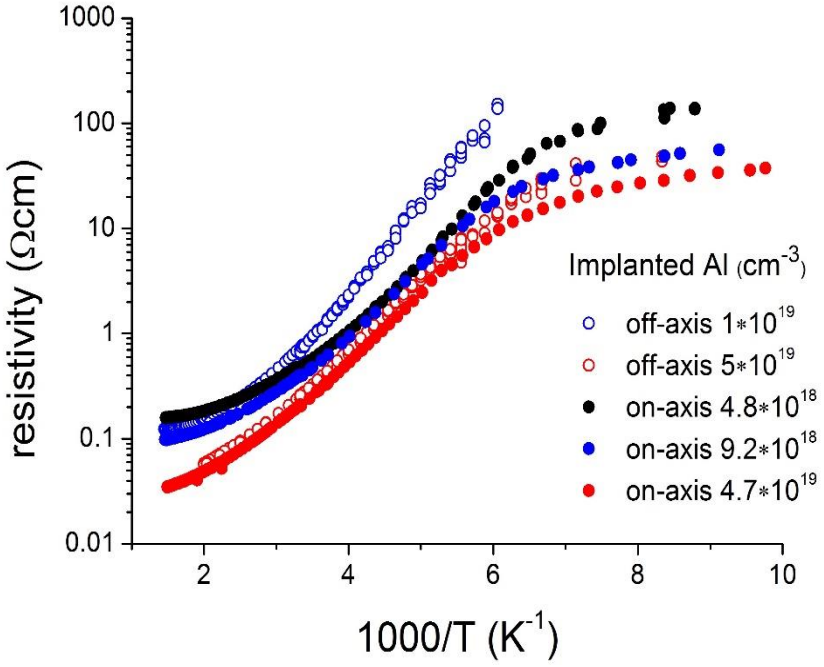

Figure 5.10: Resistivity as a function of temperature of Al^+ implanted on-axis and off-axis semi-insulating 4H-SiC, 1950°C/5min conventional annealed.

activation and compensation of implanted Al. Notwithstanding this, the similarity of these data with those of ref. [6] suggests the hypothesis of an electrical activation of implanted Al of about the 70%, with a compensation ratio of about 10-12% or even lower.

5.4 High temperature variable range hopping in heavy Al implanted 4H-SiC

5.4.1 Introduction and theory

In the previous part of this chapter, both in the investigation of on-axis and off-axis samples, the heavy Al implantation density (up to 5×10^{20} cm^{-3} in off-axis samples) and the high temperature of thermal treatments (up to 1950°C for conventional annealing and 2000°C for MWA) have induced the presence of mixed conduction effects in almost all 4H-SiC samples investigated. In fact, a transport through extend states was generally highlighted at higher temperatures, while the onset of an impurity band conduction was pointed out at lower temperatures. In the Arrhenius plot of resistivity data, the transition between the two regimes of transport is usually evidenced by a different slope of the two corresponding linear regions (see ref. [27]), as it's possible to see for the lower doped samples of figure 5.4. With the increasing of the doping level, the transition between the two different slopes appears at higher temperatures and, at the same time, the temperature range where the hole freeze out regime is recognizable becomes narrower. For the heaviest doped samples (5×10^{20} cm^{-3}), none freeze out regime is distinguishable in the Arrhenius plots reported in figure 5.1(a) and the carrier density shows a very weak temperature dependence, suggesting that the IB conduction is relevant up to RT and above. The correspondent resistivity trends of these samples (see fig. 5.4), but also that one of the 3×10^{20} cm^{-3}

Al implanted ones, deviate from the "Miller and Abrahams like" behavior, showing a sublinear trend instead of two distinct linear ones. Trying to justify this behavior, a closer look at the hopping conduction theory is necessary.

In a simplified Mott theory (see ref. [27]), the hopping conductivity and probability are proportional. Taking into account two possible hopping sites i and j, separated in energy of a quantity w_{ij}, there is an optimal minimum distance R_{ij} between these sites that maximizes the hopping probability P:

$$P \sim \exp\left(-2\alpha R_{ij} - \frac{w_{ij}}{K_B T}\right) \tag{5.3}$$

where α is the inverse of the localization length ξ. The quantity ξ is the characteristic dimension of the localized wave function: it is assumed independent of energy. In equation (5.3) the first term $exp(-2\alpha R_{ij})$ is related to the square of the overlap integral of the electronic wave functions at the i and j sites, while the second term, $exp(-w_{ij}/K_B T)$, expresses the ratio between the Boltzmann factors of the final to initial states involved in the hop. In the high temperature limit, i.e. when $w_{ij}/K_B T << 2\alpha R_{ij}$, the maximum hopping probability occurs with a minimum value of the distance R_{ij}: this is the case of the nearest neighbours hopping transport. When, instead, this high temperature limit is not verified, and then $w_{ij}/K_B T \approx 2\alpha R_{ij}$, the probability P is maximized when the hopping sites are located in energy within a band width w_{opt} (optimal energy) around the Fermi level μ, and they are spatially separated by an average optimal length R_{opt}: this is the case of the variable range hopping (VRH). The number of states with energy inside this optimal band is given by $g(\mu) \times w_{opt}$, where $g(\mu)$ represents the density of states at Fermi level, and must be equal to the number of corresponding hop sites per unit volume, N. $g(\mu)$ can be taken energy independent in a simplified approach, and $\mathbf{1/N = 4\pi R_{opt}^3/3}$ in a 3D space, while

$\mathbf{1/N = \pi R_{opt}^2}$ in a 2D space. Thanks to these considerations, the maximization of the hopping probability leads the conductivity law to the following universal form:

$$\boldsymbol{\sigma(T) = \sigma_0 exp\left[-(T_0/T)^{1/n}\right]} \qquad (\mathbf{5.4})$$

The value of *n* in the equation (5.4) is *n=4* in the case of a 3D system of non-interacting carriers, while *n=3* in a 2D system. The pre-exponential term σ_0 can be a weak function of the temperature, depending on the assumption of the model of ref. [27], but it's often assumed constant, like in this investigation. T_0 is a reference temperature, and its relation with the density of states at Fermi level and the localization length depend on the space dimensionality *d*. In the light of these considerations, in the temperature range dominated by a VRH transport the conductivity should exhibit a linear trend on a semi-logarithmic plot when reported as a function of $T^{-1/n}$, with n = 3 or 4 depending on the dimensionality (2D and 3D case, respectively)

5.4.2 Discussion

The simplified theory presented above was used to justify the conductivity trends of the four heaviest doped samples of figure 5.4, whose resistivity trends shown a sublinear behaviour. They are 8° off-axis 4H-SiC samples, heavy Al^+ implanted with densities between 3 and 5×10^{20} cm^{-3} and subject either to CA or MWA thermal treatment. The dependence of the conductivity on temperature was measured in the range 10-680 K. Main parameters of these samples are resumed in table 5.3, as like

as the main results obtained from the analysis of the conductivity data, explained below.

The temperature dependence of the conductivity for the samples investigated is shown in figure 5.11. Consistently with equation 5.4, the conductivity data of the heaviest doped samples, plotted as a function of $T^{-1/3}$ (figure. 5.11(a)), suggest the occurring of a 2D variable range hopping transport, whereas the data of lower doped samples, plotted as a function of $T^{-1/4}$, are in agreement with a 3D VRH one. In fact, a linear behaviour of the respective plots is clearly visible in the reported data. The transition between the two different dimensionalities of hopping seems to be related to the increasing of doping level: samples with a concentration of Al in the implanted layer of 3×10^{20} cm^{-3} exhibit 3D VRH transport features ($n=4$), while samples with higher concentration of 5×10^{20} cm^{-3} exhibit 2D ones ($n=3$). Conductivity trends consistent with the equation 5.4, compatible with a variable range hopping transport, are a novelty in 4H-SiC materials, as like as the variation of the value of n from 4 to 3 with increasing doping level (see ref. [28]). Note that, in figure 5.11(b) the linear trends are observed only below a temperature of about 170K, while for the heaviest doped samples of figure 5.11(a) the VRH transport is observed from low temperatures up to T≈350K. This indicates that the 2D transport is a "robust" phenomenon, resistant to higher temperatures than the 3D one. The intercepts with the vertical axis and the slope of the fitting lines permit to extrapolate the parameters σ_0 and T_0. From these parameters the optimum length can be obtained as $R_{opt} = (3/8)\xi(T_0/T)^{1/4}$ or $R_{opt} = (1/3)\xi(T_0/T)^{1/3}$, for the 3D and 2D case, respectively (see ref. [26]). In table 5.3, the obtained numerical values are reported.

The reduction of the dimensionality of VRH transport suggests the possibility of a structural modification that occurs in the implanted and annealed layer of 4H-SiC. A

2D VRH transport could be related to a strong path-anisotropy in the hopping mechanism that appears when the optimum length R_{opt} becomes comparable to a structural length characteristic of the transport channel. This can bring to the so called size-effect (see ref. [29]): the carrier hop between the electrically active Al impurities may be constrained into a flat and thin region. Such a structural length should be searched along the <0001> axis of 4H-SiC, orthogonal to the current flux applied for the resistivity measurements, and its value should be comparable with the values of R_{opt}, estimated in a few tens of nanometers, a value comparable to the average separation of electrically activated Al impurities.

Sample name	Nominal Al density (cm^{-3})	Annealing treatment	RT Hall hole density (cm^{-3})	RT resistivity (Ωcm)	n	σ_0 ($\Omega^{-1}cm^{-1}$)	Ropt/ξ at 10K
SiC296c	5×10^{20}	MWA (2000°C/30s)	3.5×10^{20}	0.023	3	1.3×10^{3}	3.5
SiC296e	5×10^{20}	CA (1950°C/5min)	1.4×10^{20}	0.03	3	5.1×10^{3}	5.3
SiC293a	3×10^{20}	MWA (2000°C/30s)	6×10^{19}	0.059	3	1.3×10^{3}	4.9
SiC293e	3×10^{20}	CA (1950°C/5min)	5.1×10^{19}	0.052	4	5.9×10^{4}	7.4
SiC293g	3×10^{20}	CA (1950°C/10min)	4.9×10^{19}	0.049	4	3.5×10^{3}	5.3

Table 5.3: main characteristics of the selected of samples taken into account.. For each sample, they are reported from left to right: the nominal Al implanted concentration, the post-implantation annealing treatment, the RT hole density and resistivity, the dimensionality of VRH, the conductivity at infinite temperature and the optimal length at 10K normalized to the localization radius.

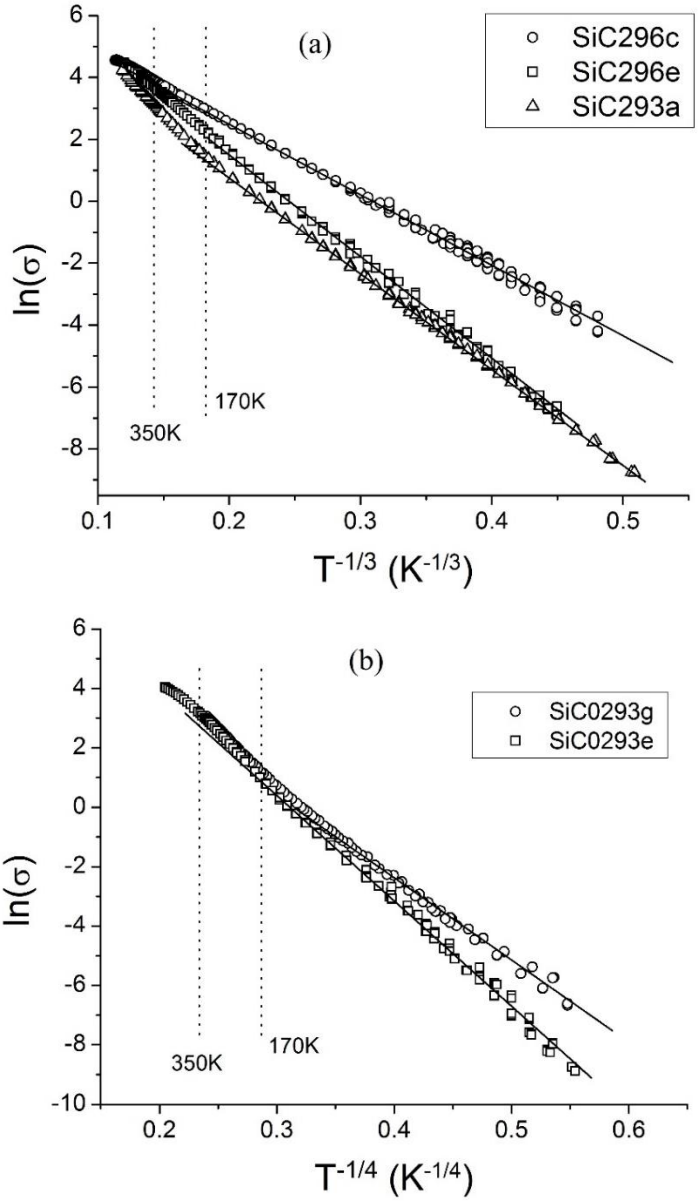

Figure 5.11: logarithm of measured conductivity as a function of $T^{-1/3}$ (a) and $T^{-1/4}$ (b) for the Al implanted 4H-SiC samples taken into account, compatible with a 2D VRH (n=3 in eq. 5.4) and a 3D one (n=4), respectively. Continuous straight lines are guides for eyes, vertical dotted lines show reference temperatures.

Figure 5.12 show a cross-sectional transmission electron microscopy (TEM) micrograph of the sample SiC296e of table 5.3 (see ref. [28]), performed at IMM institute of Bologna. The white contrasted straight segments at a small angle with respect to the sample surface, close to the 4H-SiC miss-cut angle, represent stacking faults (SFs) in the basal plane observed edge-on in this (10-10) projection. Near the surface, where the Al density is maximum and homogeneous, the defect density is lower and this should be the region of the effective conducting channel; the structural properties of this region control the layer conductivity. The average separation between adjacent SFs along the *c*-axis direction results to be of some tens of nanometers, the same order of magnitude of R_{opt}, suggesting a correlation between this

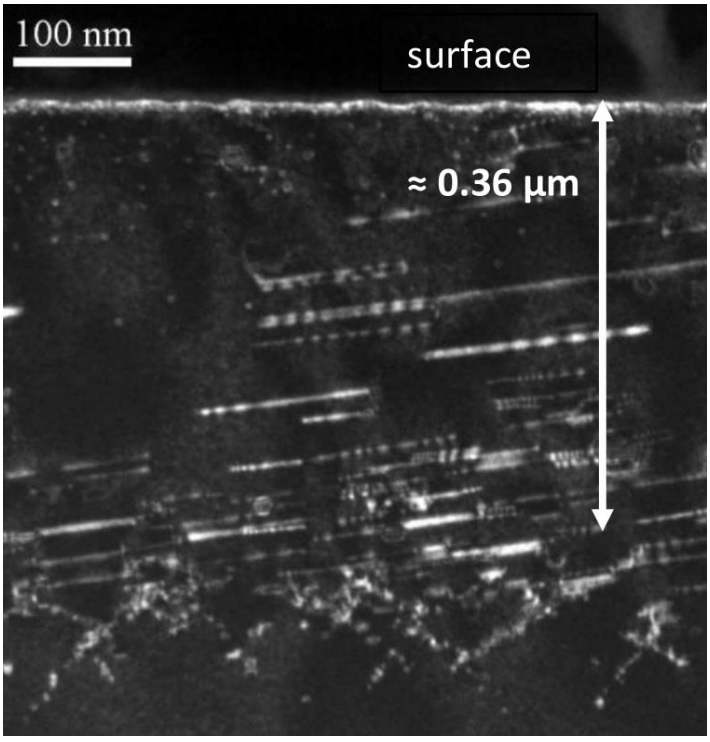

Figure 5.12: (10-10) cross-sectional WB (-g,4g) g=[0004] micrograph of sample SiC296e. Among other defects SFs are here observed edge-on as white contrasted straight segments at a small angle with the sample surface.

SF distribution and the strong anisotropy of VRH transport of the SiC296e sample. Thanks to this hypothesis is possible to give an interpretation of the values of σ_0 and R_{opt}/ξ reported in table 5.3: R_{opt} seems to be related to the doping level through the density of the impurity states near the Fermi level $g(\mu)$, while σ_0 can approximately quantify the amount of structural order in the conducting layer. The increasing concentration of implanted Al tends to decrease the values of σ_0 and R_{opt}, however their absolute values are not indicative of the dimensionality of VRH, which it's rather due to the proper spatial distribution and density of SFs. In fact, considering for example the SiC293g sample, subjected to a longer annealing time (10 minutes) with respect to SiC293e (5 minutes), shows lower values of σ_0 and R_{opt}. This suggests that the amount of disorder can evolve during the thermal treatments without consequences on d, and $g(\mu)$ may increase with time, as a consequence of the more efficient activation of Al showed before.

5.5 Preliminary electrical investigation of 4H-SiC p^+/n junctions and Schottky barriers realized by Al^+ implantation

5.5.1 Introduction

As explained in chapter 3, high implantation doses and annealing temperatures could create traps of non-negligible density inside the material. The traps can be investigated thanks to Space Charge Spectroscopy techniques (see chapter 4), which can highlight the presence of electrically active defects, other than the dopants. For this reason, in the last part of the work, it was developed an automated acquisition system for Admittance Spectroscopy and Current-Voltage measurements (see chapter 4) and an electrical investigation on p^+/n junctions and Schottky barriers 4H-SiC test devices was carried out. The automation of acquisition was provided by the development of proper acquisition programs with LabVIEW and MatLab software. Because this last part of the work was achieved mainly with the purpose of testing the automated

acquisition system, the electrical investigation showed here has to be considered as preliminary; further studies are required to fully understand the presented results.

5.5.2 Discussion of results

The p-n junctions and Schottky barriers were submitted to a preliminary electrical investigation by Current-Voltage (I-V) measurements to check their rectifying properties and Capacitance-Voltage (C-V), Admittance Spectroscopy (AS) and Deep Level Transient Spectroscopy (DLTS) measurements to determine the shallow doping profiles and the physical parameters (mainly the activation energy) of the deep levels in the active region of simple devices. Once completed, this investigation will be useful to clarify the effects of the sample processing on the formation of traps close to the implant region, even as a consequence of high temperature thermal treatments. The identification of traps in the active region of the devices and the control of their density is important to assess the optimal minority carrier lifetime, which is a key parameter for the device performances.

Current-Voltage characteristic

Figure 5.13 reports the I-V characteristics of a p^+-i-n junction (1 mm in diameter) and a Schottky barrier (400 μm in diameter) at room temperature. The Schottky barrier shows good rectification properties, with a rectification ratio of four order of magnitude at 1 V. For the p-i-n diode, only the forward current is reported since the reverse current resulted to be lower than the sensitivity limit of the used experimental

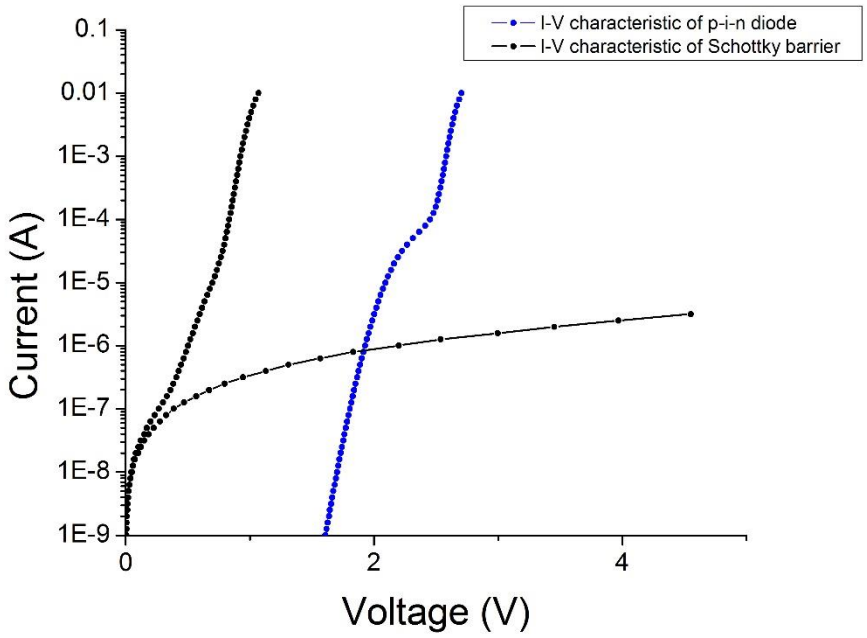

Figure 5.13: Current-Voltage characteristics of a p-i-n 4H-SiC junction and an Ti/Al /n-4H-SiC Schottky barrier.

apparatus: the rectification ratio is more than six orders of magnitude at 2.5V. The significant differences between the two characteristics (large voltage shift in the forward branch and strong variations in the amplitude of the revers current) are attributable to the different built-in voltage of the two junctions (comparable to energy gap in the p-n junction and about 1 eV in the Schottky barrier as reported in ref. [30]). The above I-V tests show that the diodes characteristics are good enough to allow reliable Capacitance and Space Charge Spectroscopy measurements.

Capacitance-Voltage profile

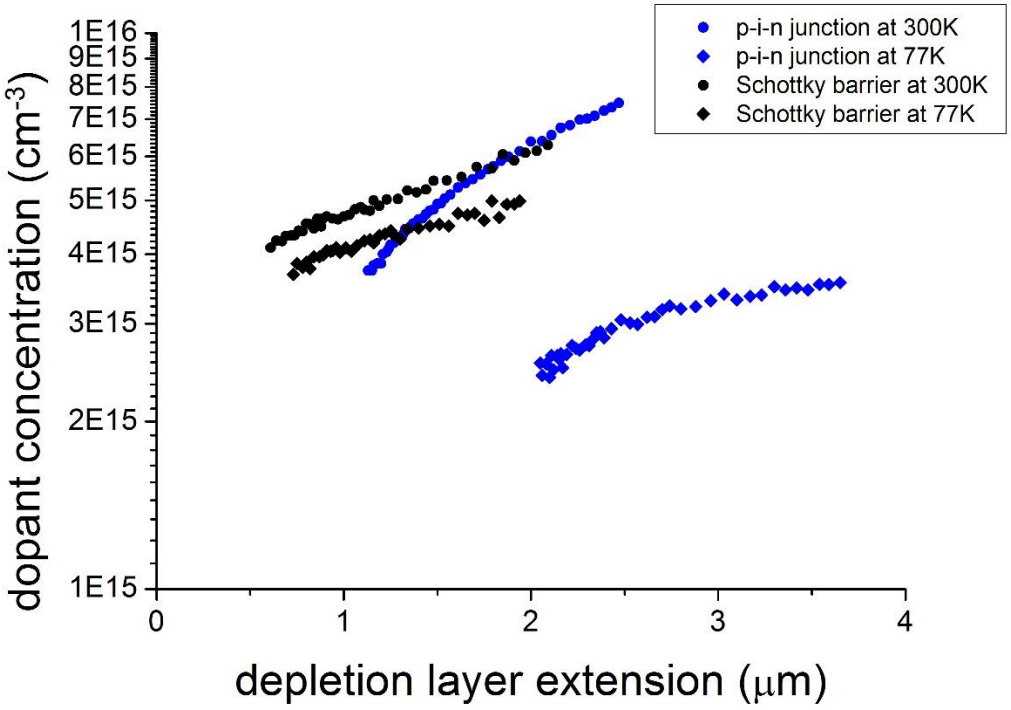

Figure 5.14: Capacitance-Voltage profiles obtained at 300 and 77K on typical p+/n 4H-SiC junctions and Al/n- 4H-SiC Schottky barriers, respectively. Test signal frequency is 1MHz.

Figure 5.14 shows the C-V profiles of the p^+/n junction and the Schottky barrier obtained at 77 and 300 K. As can be seen, the profile of the ionized-donor net concentration at 300 K slowly increases with the distance from the metal-semiconductor interface, probably due to a weak increase of free carrier concentration with depth. A possible cause of this could be a surface degradation due to the lack of carbon cap protection during the annealing. The small reduction of the profile density from RT to 77 K could be attributed to variation with the temperature of the dielectric constant and of the built-in potential. As concerns the comparison of these profiles with those obtained for the p^+/n junction, three main features need to be commented. Firstly, figure 5.14 shows that the p^+/n junction profile at 300 K starts at a larger depth

with respect to that of the Schottky barrier at the same temperature. This result could be attributed to a larger space charge region of the p/n junction at V=0 V with respect to the Schottky barrier, owing to the presence of a wide implant tail, which causes: (i) compensation effects in a wide thickness, (ii) a graded junction and even (iii) a junction interface placed more deeply from the surface with respect to the Schottky barrier. Secondly, a large difference is observable between the C-V profiles of the p/n junction at RT and 77K. Such a difference could be attributable to implantation-induced deep levels in concentration comparable to the shallow donors. Indeed, at 300K these traps can be able to change their occupancy during the voltage variations, resulting in an apparent free carrier density profile, which increases with depth, and which gives only at very large reverse bias gives (in the case of a single trap) the correct sum of trap and net donor concentrations. Differently, at 77K most of the deep levels are expected to exhibit a very low emission rate and, consequently, the obtained profile should simply give the uncompensated donor concentration. Third, the profile of the p/n junction obtained at 77K is lower than that one of the Schottky barrier probably due to the presence of implanted acceptors within the depletion region of the junction, in concentration (N_A) not negligible with respect to the donor density N_D. Moreover, the increasing of the profile density with depth is probably due to the presence of a graded junction (see ref. [31], pp. 574-575).

Admittance Spectroscopy investigation

Diodes were then investigated by Admittance Spectroscopy: AS exploits the influence of majority-carrier electronic levels, present in a depletion region on capacitance (C) and conductance (G) of a junction. By analyzing the variation of C and G as a function of both frequency of the test signal and sample temperature it is possible to determine the features of these levels (activation energy and concentration). The first step was

the characterization of a p-i-n diode (1 mm in diameter) with Admittance Spectroscopy measurements, carried out at a fixed test frequency in the 20-300 K temperature range: this measurement approach gives a full view of the deep levels present in the depletion region up to a maximum activation energy of 0.3-0.4 eV. The contribution of a deep level is evidenced by i) a step in the capacitance, overlapped to a smooth increase of C due to the variation of the dielectric constant and built-in potential with temperature, and ii) a peak of the G/ω vs. temperature (ω=2πf where f is the test signal frequency) at a temperature corresponding to the inflection point of the capacitance step. In figure 5.15 the trends of measured capacitance and G/ω as a function of temperature for three different test frequencies (2, 20 and 200 KHz) are reported. Two contributions are clearly visible both in capacitance and conductance curves (fig. 5.15). The first one appears at low temperatures (around 30 K), where the capacitance increases from 21 pF (at 20K) to 55 pF (at 40K) and G/ω shows a peak of about 10 pF.

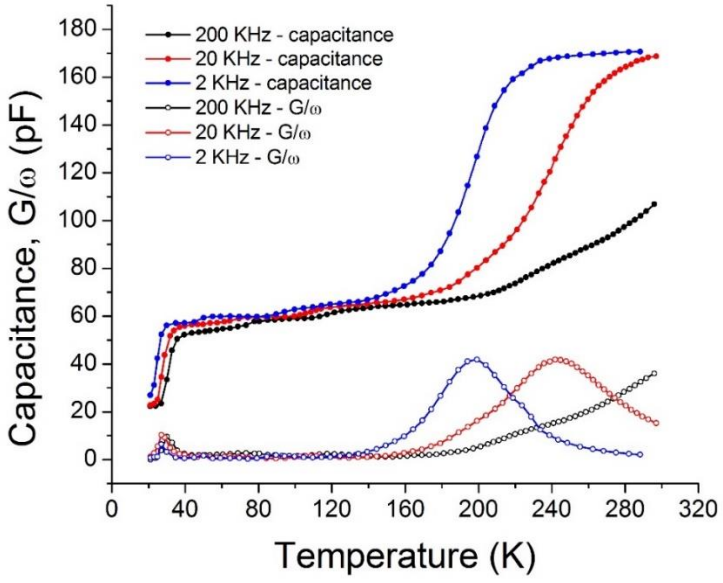

Figure 5.15: Capacitance and Conductance/ω of the p-i-n junction as a function of the temperature for three different test signal frequencies (2, 20 and 200 KHz).

The second one is clearly visible at higher temperatures where the capacitance increasing from 65 pF (at 140K) to 170 pF (at 250 K) is likewise associated to a G/ω peak. These results indicate the presence of at least two electronic levels inside the depletion layer of the structure; moreover, by taking into account that the capacitance steps and the G/ω peak amplitude are comparable to the junction capacitance absolute values, the detected levels are expected to be present in concentration of the order of the dopant density. In the 40-150 K temperature range, two other minor capacitance steps of a few pF are visible, but their characterization is difficult due to the low concentration of the associated levels. To determine the activation energy of the two main levels, AS measurements were performed as a function of the test signal frequency at different fixed temperatures.

In figure 5.16(a), the capacitance C and G/ω corresponding to the main trap appearing at high temperature in figure 5.15 are shown as a function of the frequency, at different fixed temperatures in the 170-295 K range. It's possible to see how the capacitance changes from a low frequency value (C_0) of about 170 pF, where the dominant deep level has time enough to modify its occupancy during the period of the sinusoidal signal, to an high frequency value (C_∞) of about 65 pF, where the emission and capture time of the level (near the crossing point with the Fermi level) is much lower than the period of the test signal. As expected, the G/ω vs frequency curves show peaks, with their maxima located at the same frequency of the inflection point of the capacitance steps. Their amplitudes are about 40 pF, more or less half of the corresponding capacitance step, as expected from the theory of AS. Since at the frequency corresponding to the G/ω peak (f_{max}), the emission rate of the trap is given by $e_n=6.28f_{max}/2$, it is possible to evaluate the position in energy of the level with respect to the correspondent band edge, through the analysis of the variation of the emission rate with temperature.

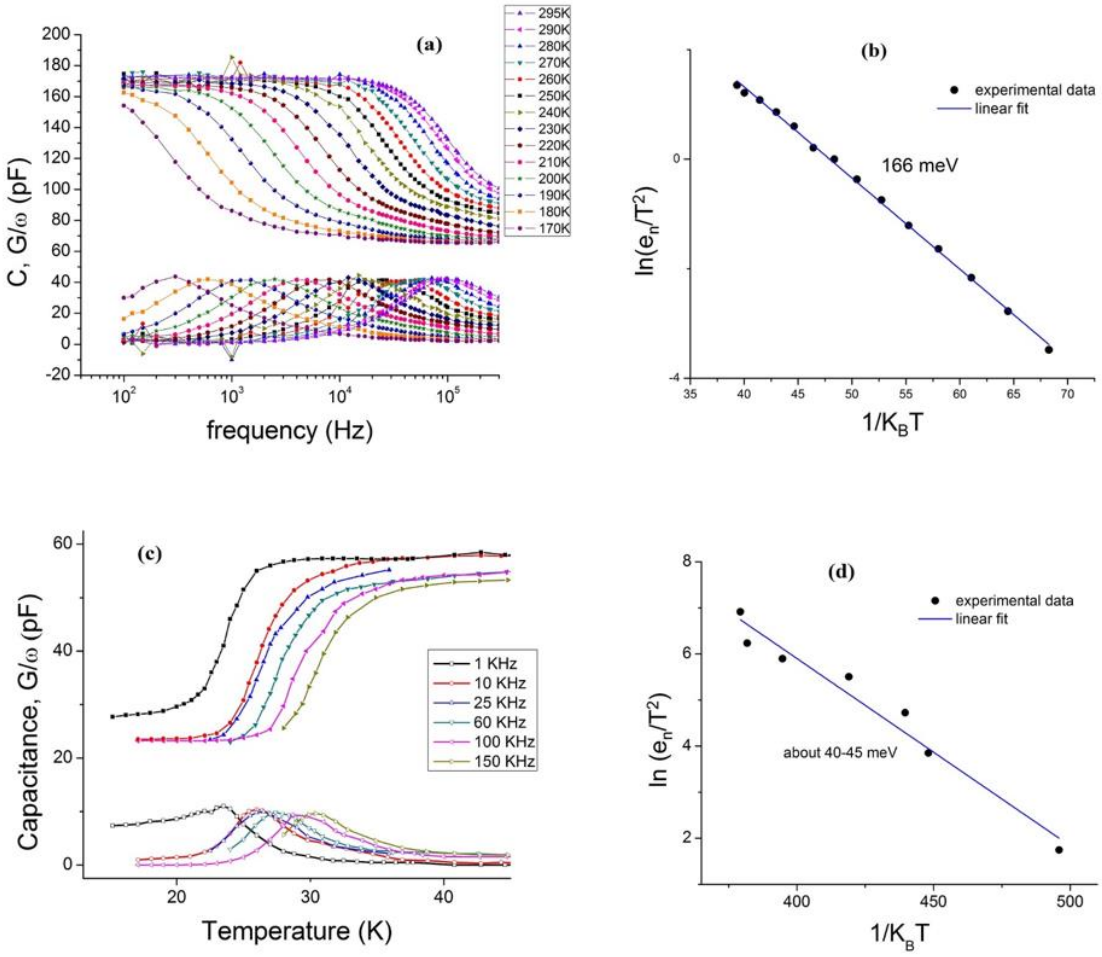

Figure 5.16: Admittance Spectroscopy measurements, performed on the p-i-n junction as a function of frequency at different fixed temperatures (a) and as a function of temperature at different fixed frequencies (c), to investigate the electronic levels reported in the high and low temperature range of fig. 5.15, respectively. On the right side, the related Arrhenius plots of the two detected traps with their estimated activation energy are reported.

In fact, considering that $e_n=AT^2\exp(-\Delta E/KT)$ (where A is a constant if the capture cross section is independent on temperature and ΔE is the activation energy of the trap), ΔE can be determined from the slope of the Arrhenius plot of e_n/T^2 as reported in figure 5.16(b).

A similar investigation was performed for the other step in capacitance at lower temperature (figure 5.16(c)). However, in this case the measurements were carried out as a function of the temperature at different fixed frequencies, owing to the difficulty to obtain a good stabilization of the sample temperature for T<40 K. The corresponding Arrhenius plot of e_n/T^2 is reported in figure 5.16(d). The activation energies obtained from the Arrhenius plots of figure 5.16(b and d), are of about ΔE_1=160-170 meV and ΔE_2=40-45 meV for the peaks revealed at high and low temperature, respectively. Taking into account the fact that AS technique is able to reveal only majority carrier traps, the detected levels could be either donors located in the low doped n-type side of the junction, or acceptors in the p-side one. Since the p-n junction is graded (and therefore not strongly asymmetric), both the impurity levels are in principle detectable. For this reason, ΔE_1 could be attributed to the energy level of the aluminum dopant: this values is lower than the fundamental state energy of the isolated Al impurity; however, this is not surprising, owing to the significant p-type doping level, which induces a reduction of the thermal activation energy of the acceptor, as mentioned in chapter 2.5. This interpretation is reinforced by the fact that in the Schottky barrier no deep level has been observed by AS in at T=146K and T=300K, as evidenced by the figure 5.17. In fact, no capacitance step nor G/ω peak have been observed in this case at the two investigated temperature. Note that the different absolute value of the capacitance in figure 5.16 and figure 5.17, which in part is due to the different areas of the devices. ΔE_2 is related, instead, to the n-type dopant of the epilayer (N).

Admittance measurements were repeated also on another p-i-n junction with identical characteristics but different diameter (0.4 mm), using a different cryostat and LCR-meter, to check the reproducibility of the above data: the obtained results were very close to those above reported.

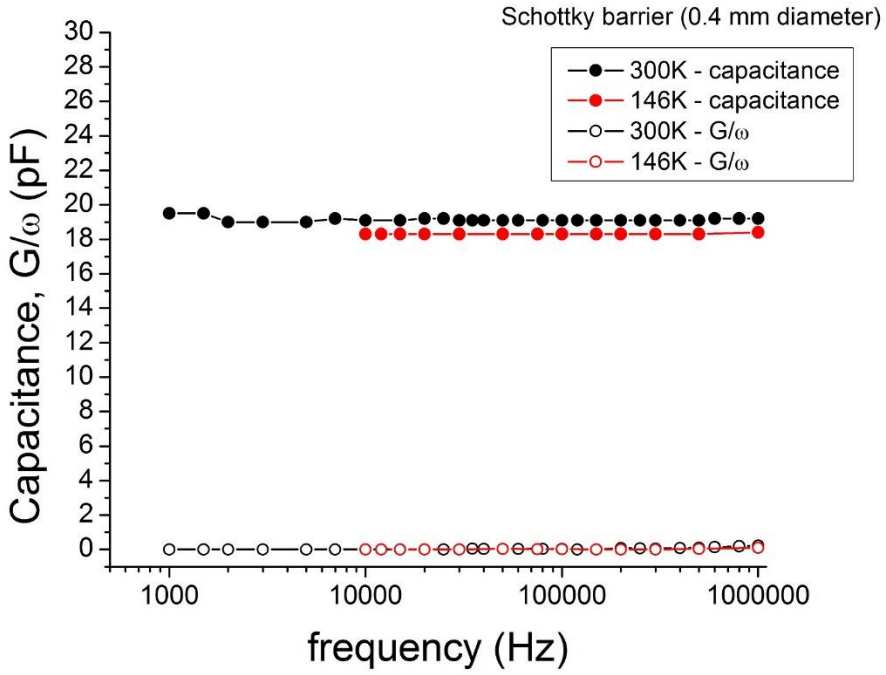

Figure 5.17: Admittance Spectroscopy measurements, performed on the 0.4 mm 4H-SiC Schottky barrier as a function of frequency, at two different fixed temperatures of 146 and 300K.

DLTS investigation

To have additional information about the deep levels located in the space charge regions, the diodes were submitted to DLTS analysis; indeed this technique allows: i) to detect trap levels located in a deeper energy range with respect to AS and ii) to distinguish and study, unlike AS, both minority and majority carrier traps, which are conventionally associated to positive and negative DLTS peaks, respectively.

In figure 5.18 the DLTS spectra of a diode, 0.4 mm in diameter, are reported. All these spectra were obtained with the same pulse duration (50 μs), frequency (1 KHz) and

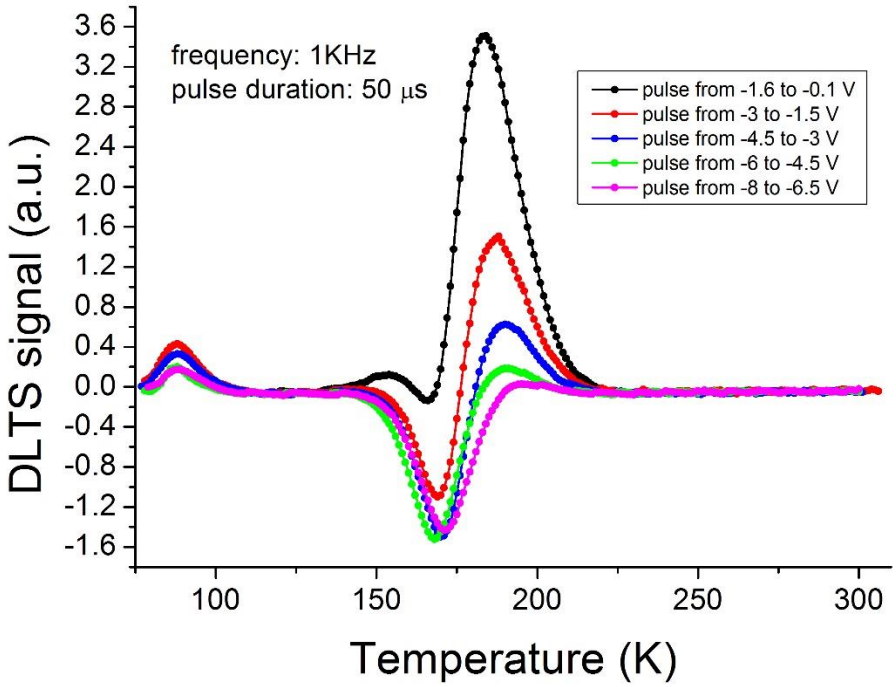

Figure 5.18: DLTS spectra as a function of temperature obtained on the p^+/n junction using different reverse bias from -1.6 V to -8 V and pulse amplitude of 1.5 V.

pulse amplitude (1.5V); the applied reverse bias, instead, increases from -1.6 to -8.0 V. Positive polarization pulses were never used, however, it's possible to see in this figure at least two positive peaks, attributable to minority carrier traps, one in the range between 80 and 100 K and the other in the range 170-220K. The presence of positive DLTS peaks without using minority carrier injection by positive voltage pulses is anomalous and is probably due to the graded p-i-n junction, as suggested by ref. [31] (see p. 580 and following). However, by applying high reverse voltage and maintaining the same pulse amplitude, in order to explore intervals of the depletion region further and further away from the junction interface, a negative peak in the 150-190 K temperature range, corresponding to a majority carrier trap, is detected.

Finally, in the temperature range from 220K to RT, no DLTS signal was observed.

In order to determine the activation energy of the level associated to the positive peak, DLTS spectra have been obtained for different pulse frequencies, as reported in figure 5.19(a). The measurement parameters (pulse amplitude = 1.5V, reverse bias = -1.6V) were chosen in such a way to minimize the negative peak contribution. Known the pulse frequency used in the measurements, the emission rates (e_n) of the trap at the temperatures corresponding to the peak maxima were determined. From the Arrhenius plot (figure 5.19(b)) of e_n/T^2, the activation energy of the trap is then extracted. From the inspection of figure 5.19(a), however, the large width of the peak and the appearing of a shoulder for pulse frequency of 404 Hz clearly indicate that the positive signal is due to the superposition of two contributions of levels with very near activation energies. The simultaneous presence of two positive peaks and a negative peak in a narrow interval of temperature certainly makes difficult the separation of the different contributions and the correct determination of the corresponding activation energies.

A similar analysis was carried out for the low-temperature peak, whose DLTS spectra, obtained at different frequencies from 64 to 1907 Hz, are reported on figure 5.19(c). The pulse height was kept to 1.5V, with a quiescent bias at 0V (pulse: from 0 to +1.5V), to enhance the amplitude of the DLTS signal. The wide variation of the peak amplitude with frequency is probably due to a non-exponential transient or to a large variation of the capture cross section with the temperature. At 64 Hz (black curve in figure 5.19(c)), DLTS signal shows a very small amplitude so that a rough peak is visible only using frequency at 190 Hz. However, a reliable evaluation of the peak temperature was possible only from 501 Hz.

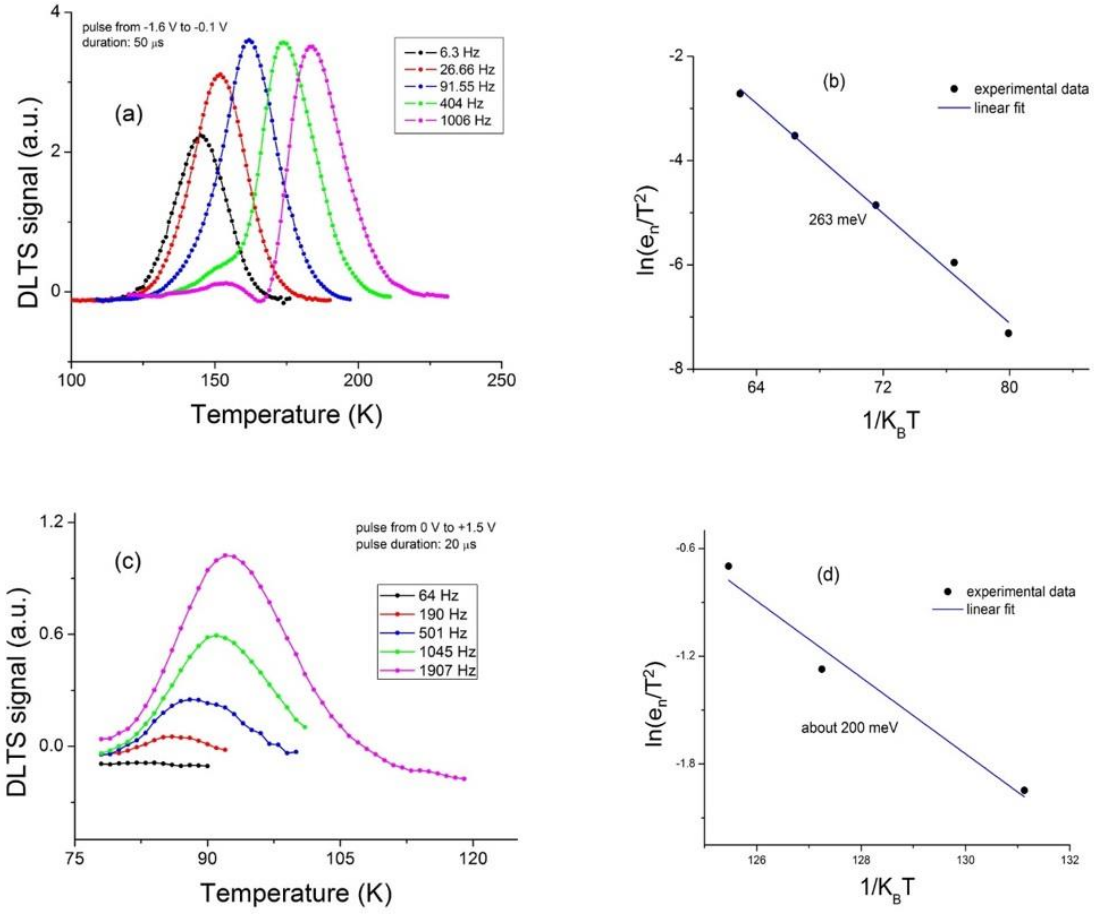

Figure 5.19: DLTS spectra as a function of temperature at different pulse frequencies relative to the high (a) and low (c) temperature positive peaks. On the right side are reported the related Arrhenius plots.

Moreover, owing to the low DLTS signal amplitude at low frequency and to the poor reproducibility of the spectra, the activation energy of this related trap, extracted from the Arrhenius plot (figure 5.19(d)), was affected by a not negligible error.

The activation energy associated to these minority carriers traps resulted respectively ΔE_3=260-270 meV and $\Delta E_4 \approx$200 meV for the two main positive DLTS peaks at high

and low temperature, respectively. These results can be critically compared with those reported in ref. [32], where similar samples have been investigated. In particular, the activation energy of the E_3 level, or alternatively that one corresponding to the very near shoulder (appearing in figure 5.19(a), at frequency 404 Hz), is very similar to the one of the $HS1^*$ (= 0.25 eV) of ref. [32], that in such a paper has been suggested to be associated to the Al acceptor. The difference between this energy and the value ΔE_1=160-170 meV, obtained before by AS and tentatively assigned again to the Al acceptor, could be attributed to the fact that in the DLTS measure the Al acceptors are detected in a region where they are present in low density (that is in the final trait of the implant tail, in the n-type side of the junction, where they behave as a minority carrier trap), therefore their thermal activation energy should approach the value expected for the isolated Al impurity (about E_{Al} = 240 meV, see ref. [9]). Differently, AS measurements probably detect the Al level in the highly doped p-type layer, where the high doping reduces the thermal activation energy of the impurity (see ref [32]).

Figure 5.20 reports the DLTS spectra, taken at different pulse frequencies, of the majority carrier trap that corresponds to the negative peak observed in figure 5.18. To characterize this trap it is necessary to minimize the contribution of the positive peak at ΔE_3=260-270 meV (see fig. 5.18), so that to avoid a distortion of the negative signal, whose peak appears approximately at the same temperature of that related to E_3. For this reason, the analysis of the negative peak was carried out by applying a high reverse bias of -8 V, keeping the pulse height to 1.5V. These DLTS spectra (see figure 5.20(a)) are reported for frequencies in the range 70-1031 Hz. Also in this case there is a large variation of the peak amplitude with frequency, again probably due to a non-exponential transient or to a large variation of the capture cross section with the temperature.

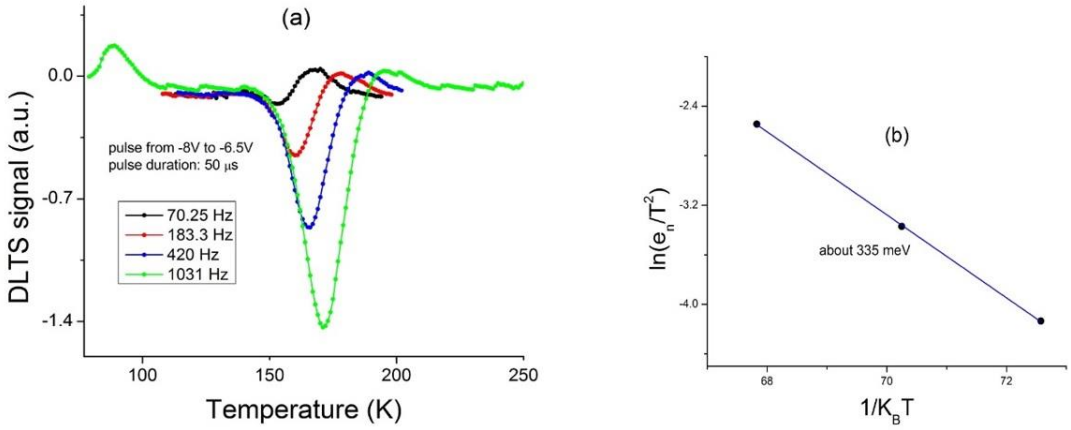

Figure 5.20: DLTS spectra (a) as a function of temperature at different pulse frequencies of the negative peak. On the right side (b) the related Arrhenius plot is reported.

The negative peak is now clearly distinguishable, especially in spectra obtained using the highest frequencies. The activation energy associated to this majority carriers trap (E_5) has been found to be ΔE_5=330-340 meV. Only incidentally, the energy of such a peak is comparable to the peak at ΔE=350 meV in ref. [32], therein labelled HS1 and associated to an intrinsic defect D_1, known as a hole trap (see ref. [34]). However, whereas in ref. [32] HS1 level appears as a positive peak, here, the E_5 behaves as a majority carrier trap, because of the negative peak polarity. In any case, since it is not known the side (p or n) of the depletion region from which mainly the DLTS signal derives, actually it is not possible a clear identification of such a trap in the contest of the present work. Further investigations are required to analyze in more detail the characteristics of this level.

Finally, in ref. [32] another very weak peak has been detected at ΔE=500 meV, labelled HS2 and attributed to a complex involving a second contaminant acceptor: B. This trap was not observed in the spectra discussed in the present work, probably

because of (i) the low HS2 density; (ii) a higher apparent C-V carrier density with respect to ref. [31], which makes the detectability of such a trap more difficult; (iii) different DLTS parameters used in the experiment (different reverse biases and voltage pulses).

To compare the deep levels present in the space charge region of the diodes before and after implantation, a preliminary DLTS investigation was carried out also on a Schottky barrier (here not showed). However, no detectable DLTS signal in the 77-300K temperature range was observed. This result suggests that the detected traps on the p-i-n junction are related to ion implantation.

A preliminary comparison with literature relative to traps in 4H-SiC (see ref. [35] and [36]) put in evidence in the reported DLTS spectra (see figure 5.18) the absence of DLTS signal in the 270-300K temperature range, where usually is detected the contribution of the $Z_{1/2}$ deep level. This trap, placed 0.56-0.71 eV below the conduction band minimum, should be related to the carbon vacancies, V_C, (see ref [35]), which is a major point defect in high-purity 4H-SiC epitaxial layers limiting the minority carrier lifetime. However, the absence of DLTS signal in the 270-300K temperature range could also be due to different experimental conditions of the investigation performed in the present work with respect to the literature works, and different characteristics of the samples investigated. In this respect, it is worth noting that the sensitivity of the DLTS technique is limited by the majority impurity density: because, in the samples here studied, the N doping level is of the order of 10^{15} cm^{-3}, the minimum detectable trap density is of the order of 10^{11}-10^{12} cm^{-3}. This limit is just comparable with the V_C concentration expected in epitaxial layers annealed at 1600°C (about 10^{12} cm^{-3}, see ref. [35]). In conclusion, the presence of the carbon vacancy cannot be excluded in these samples. Moreover before to draw a conclusion on the

presence of the V_C defect, even the possibility to detect the EH_7 (see ref. [36]) level should be explored, which is another deep level associated to the carbon vacancy and placed 1.55–1.65 eV below the conduction band minimum. A complete characterization of the deep traps in the wide band gap 4H-SiC should require the study of deeper levels than in the present investigation, which was limited to traps of relatively low activation energies (up to 335 meV). Such an improvement could be obtained by DLTS measurements carried out at higher temperature than in the present case, from 300 to 600 K. The investigation of this temperature range needs special cryostats and contacts able to support high temperatures without altering the electrical characteristics of the junction. This type of DLTS characterization has been planned for the next future.

In the light of the purpose of this preliminary investigation, the experimental data obtained with the developed acquisition system are almost equal to the ones obtained with a different experimental setup (an HP 4192 LCR-meter) at IMEM-CNR Institute of Parma (Italy). This may indicate that the automated acquisition system, tested for the first time, is reliable.

5.6 References of this chapter

[1] R. Nipoti et al., "Microwave annealing of very high dose Aluminum-implanted 4H-SiC", Applied Physics Express 4, 111301 (2011)

[2] J. M. Bluet et al., "Activation of aluminum implanted at high doses in 4H–SiC", Journal of Applied Physics 88 No. 4 (2000)

[3] Y. Negoro et al., "Electrical activation of high-concentration aluminum implanted in 4H-SiC", Journal of Applied Physics (2004), 96(9): 4916-4922

[4] A. Parisini et al., "Remarks on the room temperature impurity band conduction in heavily Al^+ implanted 4H-SiC", Journal of Applied Physics 118, 035101 (2015)

[5] I.G. Ivanov et al., "Ionization energies of phosphorus and nitrogen donors and aluminum acceptors in 4H silicon carbide from the donor-acceptor pair emission", Phys. Rev. B 71, 241201 (2005)

[6] A. Parisini et al., "Analysis of the hole transport through valence band states in heavy Al doped 4H-SiC by ion implantation", Journal of Applied Physics 114, 243703 (2013)

[7] V. Heera et al., "A comparative study of the electrical properties of heavily Al implanted, single crystalline and nanocrystalline SiC", Journal of Applied Physics 99, 123716 (2006)

[8] H. Matsunami et al., “Step-controlled epitaxial growth of SiC: High quality homoepitaxy”, Mater. Sci. Eng. R20, 125 (1997)

[9] F. Schmid et al., “Hall Scattering Factor for Electron and Holes in SiC”, Silicon Carbide: Recent Major Advances, (Springer, 2004) p. 517

[10] J. D. Wiley, “Mobility of Holes in III-V compounds” inside “Semiconductors and semimetals”, edited by R. K. Willardsonand A. C. Beer, Academic, New York (1975), Vol. 10, pag.91

[11] A. Koizumi et al., “Temperature and doping dependencies of electrical properties an Al-doped 4H-SiC epitaxial layers”, Journal of Applied Physics 106, 013716 (2009)

[12] J. Pernot et al., “Electrical transport properties af aluminum-implanted 4H-SiC”, Journal of Applied Physics 98, 023706 (2005)

[13] D. Ermin, “The Sign of the Hall Effect in Hopping Conduction”, Phil. Mag. 35, 1189-1198 (1977)

[14] N. F. Mott et al., “Electronic processes in Non-Crystalline Materials”, Clarendon Press, Oxford 1971 (chap. 2 pag. 53 and chap. 6 pag. 152)

[15] P. Achatz et al., “Doping-induced metal-insulator transition in aluminum-doped 4H silicon carbide”, Applied Physics Letters 92, 072103 (2008)

[16] A. Nath et al., “Microwave Annealing of High Dose Al^{+}-implanted 4H-SiC: Towards Device Fabrication”, Journal of Electronic Materials 43, pp 843-849 (2014)

[17] V. Heera et al., "p-Type doping of SiC by high dose Al implantation – problems and progress", Applied Surface Science 184 (2001) 307-316

[18] A. Miller et al., "Impurity Conduction at Low Concentrations", Physical Review 120, 745 (1960)

[19] E. A. Davis et al., "Compensation Dependence of Impurity Conduction in Antimony-Doped Germanium", Phys. Rev. 140, A2183 (1965)

[20] H. Nakamura et al., "Microstructural and electrical properties of Al-implanted and lamp-annealed 4H-SiC", Material Science Forum 389-393 (2002) pp 807-810

[21] R. Nipoti et al., "1950°C annealing of Al^+ implanted 4H-SiC: sheet resistance dependence on the annealing time" accepted on Materials Science Forum (2016); ICSCRM2015 4-9 October 2015; Giardini Naxos (Sicily), Italy

[22] N. Thierry-Jebali et al., "Observation of the generation of stacking faults and active degradation measurements on off-axis and on-axis 4H-SiC PiN diodes", Applied Physics Letters 101 (2012) 222111

[23] J. U. Hassan et al., "On-Axis Homoepitaxial Growth of 4H-SiC PiN Structure for High Power Applications", Materials Science Forum, vol 740-742, pp.173-176 (2013)

[24] A. Salemi et al., "Fabrication and Design of 10 kV PiN Diodes Using On-axis 4H-SiC", Materials Science Forum, vol 778-780, pp.836-840 (2014)

[25] R. Nipoti et al., "Conventional thermal annealing for a more efficient p-type doping 4H-SiC", Journal of Materials Research, vol. 28(1) (2013) 17-22

[26] R. Nipoti et al., "Al^+ Ion Implanted On-Axis <0001> Semi-Insulating 4H-SiC", Materials Science Forum vols. 821-823, p. 399-402 (2015) ECSCRM2014; 21-25 September 2014; Grenoble (France)

[27] B. I. Shklovskii et al., "Electronic properties of doped semiconductors", Springer Verlag (1984)

[28] A. Parisini et al., "High temperature Variable Range Hopping in Al implanted 4H-SiC", accepted on Materials Science Forum (2016)

[29] M. E. Raikh et al., "Size effect in the longitudinal hopping conduction of a narrow two-dimensional channel", Phys. Rev. B 42, 11203 (1990)

[30] J. Kohlscheen et al., "Band line-up determination at p- and n-type 4H-SiC Schottky interfaces using photoemission spectroscopy", Journal of Applied Physics 94, n. 6 (2003)

[31] P. Blood and J. W. Orton, "The electrical characterization of semiconductors: majority carriers and electron states", Academic Press (1992), ISBN: 0-12-528627-9

[32] F. Fabbri et al., "C-V and DLTS Analyses of Trap-induced Graded Junctions: the Case of Al^+ Implanted JTE p^+n 4H-SiC Diodes", Material Science Forum vols. 615-617, p. 469-472 (2009)

[33] A. Schoner et al, “Dependence of the aluminum ionization energy on doping concentration and compensation in 6H-SiC”, Institute of Physics Conferences Series n° 142, p. 493-496 (1996)

[34] L. Storasta et al., “Pseudodonor nature of the D_I defect in 4H-SiC”, Applied Physics Letters 78, p. 46 (2001)

[35] H. M. Ayedh et al., “Elimination of carbon vacancies in 4H-SiC employing thermodynamic equilibrium conditions at moderate temperatures”, Applied Physics Letters 107, 252102 (2015)

[36] N. T. Son et al., “Negative-U System of Carbon Vacancy in 4H-SiC”, Physical Review Letters 109, 187603 (2012)

6. Conclusions

In this work has been presented the electrical investigation on 4H-SiC samples, heavily p-type doped by implantation of Al ions. Ion-implanted layers on either 4H-SiC high purity substrates or on epitaxial n-type layers to obtain a p-n junction were investigated. The single layer samples were submitted to very high temperature (1950-2000°C) post-implant thermal treatments, as an original approach explored to improve the activation efficiency of the implanted element and the electrical conductivity of the material. Several Al^+-implanted 4H-SiC samples, resulting of p-type conductivity, were investigated, up to nominal densities in the 10^{20} cm^{-3} decade and subjected to two different high temperature thermal treatments. One annealing method provided by a radiofrequency heated furnace till to 1950°C (Conventional Annealing, CA) for duration in the range 5-40 min, while the other exploited a microwave field, providing a fast heating rate up to 2000°C/30s (Micro-Wave Annealing, MWA). In this contest, both off-axis and on-axis <0001> 4H-SiC wafers were investigated.

Concerning p-type off-axis samples, a high electrical activation of implanted Al, in the range of 50-70%, and a compensation ratio around 10% were estimated. In this work, the main sample processing parameters have been varied, as the implant density and temperature, the CA annealing duration, and the heating/cooling rates. MWA method showed higher hole density and lower mobility than CA in equivalent ion implanted layers, resulting in a lower resistivity, probably related to the 50°C higher annealing temperature. An electrical resistivity at room temperature in the low 10^{-2} Ωcm decade was experimentally observed, a value on the lowest reported in literature

for this kind of samples, and an optimal duration of the CA treatment was estimated in about 12-13 minutes.

Notwithstanding the heavy p-type doping levels, the carrier density remained less than the critical one required for a semiconductor to metal transition in all samples. However, the high carrier densities obtained was high enough to trigger an impurity band (IB) conduction. In the heaviest doped samples, such a conduction mechanism persists up to RT, without significantly prejudice the mobility values. This could be an interesting feature from a technological point of view, because it guarantees a nearly temperature-independent carrier density, the latter being not affected by freeze-out effects. The usual transport mechanism occurring in the IB conduction is the nearest neighbor hopping: such a regime is effectively consistent with the resistivity temperature behavior of the lowest doped samples. In the heavier doped samples, however, a trend of the resistivity data compatible with a variable range hopping (VRH) conduction has been pointed out, here highlighted for the first time in p-type 4H-SiC.

Even more: in the heaviest doped samples, and in particular, in those annealed by MWA, the temperature dependence of the resistivity data is consistent with a reduced dimensionality (2D) of the VRH conduction. In these samples, TEM investigation pointed out faulted dislocation loops in the basal plane, whose average spacing along the c-axis is comparable with the optimal length of the hops in the VRH transport. This result suggested the assignment of such a peculiar electrical behavior to a kind of spatial confinement into a plane of the carrier hops, equivalent in practice to a strong anisotropy of the layer conductivity.

In the last part of the work, a preliminary investigation of the electrical properties of 4H-SiC p-n diodes was finally performed thanks to Space Charge Spectroscopy

techniques. In this case, a heavy Al^{+} doping was obtained by ion implantation on n-type (N) epilayers and annealing thermal treatment at 1600°C, processes following the technological steps planed for final devices. For this kind of study, it was developed an automated acquisition system, mainly for Admittance Spectroscopy and Current-Voltage measurements, by the utilization of LabVIEW and MatLab software. The preliminary electrical investigation shown the presence of electrically active defects other than the dopants ones, induced in the depletion region of the diodes by ion implantation.

7. Acknowledgements

At the end of this Ph. D. I want to say thank you to all the people who have made this work possible.

A big thank you first of all to my research group: in particular, to my supervisor Dr. Antonella Parisini, which allowed me to perform this Ph. D. and supported me in the learning of the arguments discussed in this thesis. Thank you also to mr. Salvatore Vantaggio for the contribution in the laboratory activity.

Thank you also to the research group of Dr. Roberta Nipoti of CNR-IMM Institute of Bologna (Italy), responsible of the processing of the samples and transport data above room temperature. Amongst her coworkers, in particular, I would like to thank Dr. Andrea Parisini, for the TEM investigation and Dr. Maurizio Puzzanghera for his useful discussions. I would even thanks Dr. Enos Gombia of CNR-IMM Institute of Parma (Italy) for his valuable advice on the space charge spectroscopy investigation.

E adesso scrivo in italiano perché, per quanto si possa conoscere bene una lingua straniera, non ci si riesce mai ad esprimere bene come nella propria madrelingua. Grazie di cuore Antonella per tutto quello che hai fatto per me in tutti questi anni, ben al di là di quello che era il tuo compito, e non solo riguardo all'attività di ricerca scientifica. Grazie Salvat… ops… Rino per tutti i trucchetti che mi hai svelato per svolgere al meglio l'attività di laboratorio, ma soprattutto per la compagnia e per la preziosissima macchinetta del caffè che hai messo a disposizione. Grazie ovviamente anche a Roberta e ad Enos per l'importante contributo che avete dato a questo lavoro.

Ringrazio poi tutti i miei colleghi e compagni di dottorato, diventati nel corso del tempo anche ottimi amici: le pause pranzo sarebbero state molto più grigie senza la loro compagnia. Un ringraziamento a tutti i miei amici, senza la cui compagnia non so dove sarei adesso. Un grande grazie anche a tutta la mia famiglia, per tutto quello che ha fatto e fa per me.

In ultimo, non certo per importanza, un enorme grazie a tre persone speciali: Federica, Selena e Vincenzo. Non ho certo bisogno di specificare per quale motivo li devo ringraziare, loro lo sanno benissimo.